Reduced-Order Dynamic Modeling, Fouling Detection, and Optimal Control of Solar-Powered Direct Contact Membrane Distillation

Dissertation by

Ayman Mustafa Karam

In Partial Fulfillment of the Requirements

For the Degree of

Doctor of Philosophy

King Abdullah University of Science and Technology, Thuwal,

Kingdom of Saudi Arabia

December, 2016

EXAMINATION COMMITTEE PAGE

The dissertation of Ayman Mustafa Karam is approved by the examination committee.

Committee Chairperson: Taous Meriem Laleg-Kirati - Assistant Professor
Committee Members: Denis Dochain - Professor, Jeff Shamma - Professor, Noreddine
Ghaffour - Research Professor, Slim Alouini - Professor

3

ABSTRACT

Reduced-Order Dynamic Modeling, Optimal Control, and Fouling Detection of Solar-Powered Direct Contact Membrane Distillation

Ayman Mustafa Karam

Membrane Distillation (MD) is an emerging sustainable desalination technique. While MD has many advantages and can be powered by solar thermal energy, its main drawback is the low water production rate. However, the MD process has not been fully optimized in terms of its manipulated and controlled variables. This is largely due to the lack of adequate dynamic models to study and simulate the process. In addition, MD is prone to membrane fouling, which is a fault that degrades the performance of the MD process.

This work has three contributions to address these challenges. First, we derive a mathematical model of Direct Contact Membrane Distillation (DCMD), which is the building block for the next parts. Then, the proposed model is extended to account for membrane fouling and an observer-based fouling detection method is developed. Finally, various control strategies are implemented to optimize the performance of the DCMD solar-powered process.

In part one, a reduced-order dynamic model of DCMD is developed based on lumped capacitance method and electrical analogy to thermal systems. The result is an electrical equivalent thermal network to the DCMD process, which is modeled by a system of nonlinear differential algebraic equations (DAEs). This model predicts the water-vapor flux and the temperature distribution along the module length. Experimental data is collected to validate the steady-state and dynamic responses of the proposed model, with great agreement demonstrated in both.

The second part proposes an extension of the model to account for membrane fouling. An adaptive observer for DAE systems is developed and convergence proof is presented. A method for membrane fouling detection is then proposed based on adaptive observers. Simulation results demonstrate the performance of the membrane fouling detection method.

Finally, an optimization problem is formulated to maximize the process efficiency of a solar-powered DCMD. The adapted method is known as Extremum Seeking (ES). A Newton-based ES is designed and the proposed model is used to accurately forecast the distilled water flux. Although good results are obtained with this method, a practical modification to the ES scheme is proposed to enhance the practical stability.

ACKNOWLEDGEMENTS

First and above all, I praise Allah, the almighty for providing me this opportunity and granting me the capability to proceed successfully.

I would like to thank my supervisor, Prof. Meriem Laleg, for her continued support throughout my Ph.D. study and research, for her thoughtful guidance and feedback in writing this thesis, and for her warm encouragement, even during tough times in my Ph.D. pursuit. I am thankful to Prof. Noreddine Ghaffour for his support and the many discussions we had on membrane distillation. My gratitude extends to the rest of my committee members, Prof. Jeff Shamma and Prof. Slim Alouini. I am grateful for the helpful discussions and inspiring teaching. My gratitude to Prof. Denis Dochain.

The members of EMAN group have contributed to my personal and professional time at KAUST. I have had the pleasure to work alongside Abderrazak Chahid, Shahrazed Elmetennani, Zehor Belkhatir, Sharefa Asiri, and postdocs Ibrahima Ndoye, Chadia Zayane. Thank you all for the stimulating discussions, good advice and collaboration. Special thanks to my colleagues Usman Majeed and Fadi Eleiwi for the endless discussions and motivational cheerful words during the hard times.

My appreciation also goes to my friends and peers Hassan Trigui, Wail Ba-Alawi, and Zaid Sawlan for making my time at KAUST a wonderful and memorable experience. Special thanks to Amer Almadani and Saeed Atif Saeed for their contributions in my life and encouragements to pursue my studies.

My heartfelt sincere gratitude to my parents and family for their continuous support and encouragement. I am deeply grateful to my wife Maryam, for the joy and happiness she brought into my life and her patience and support through this journey. This work is detected to my Son Eyad, who has been my blessing and companion throughout this endeavor.

TABLE OF CONTENTS

LIST OF ABBREVIATIONS

AGMD   Air Gap Membrane Distillation

DAE   Differential Algebraic Equation

DCMD   Direct Contact Membrane Distillation

ES   Extremum Seeking

KAUST   King Abdullah University of Science and Technology

MD   Membrane Distillation

MF   Microfiltration

MPC   Model Predictive Control

ODE   Ordinary Differential Equation

PDE   Partial Differential Equation

RO   Revers Osmosis

TPC   Temperature Polarization Coefficient

UF   Ultrafiltration

VMD   Vacuum Membrane Distillation

WDRC   Water Desalination and Reuse Center

LIST OF SYMBOLS

A_m Differential cell membrane area (m^2)

A_{cs} Cross sectional area (m^2)

B_m Membrane mass transfer coefficient (kg/m^2sPa)

B_D Molecular diffusion coefficient (kg/m^2sPa)

B_{Kn} The Knudsen coefficient (kg/m^2sPa)

C Thermal capacitance (J/°C)

C_{elc} Electrical capacitance per unit length Farad/m (F/m)

D Diffusivity of water vapor and air mixture (m^2/s)

D_h Hydraulic diameter

$H_v[T]$ Latent heat of vaporization at temperature T (J/kg)

I Electrical current Ampere (A)

J Mass flux of distilled water (kg/m^2s)

L Thermal inductor

L^2 The set of square integrable functions.

L^∞ The set of essentially bounded measurable functions.

M Mass flow rate (MFR) (kg/s)

P Vapor pressure (Pa)

$P_w^{sat}[T]$ Saturation vapor pressure of pure water at temperature T (Pa)

P_a The air pressure (Pa)

Pr Prandtl number

Q Heat transfer rate Watt (W)

R_{elc} Electrical resistance per unit length (Ω/m)

Re Reynolds number

T Temperature (°C or K)

V Voltage Volt (V)

Z Impedance (Ω)

$\bar{R}$ Gas constant (J/mol K)

δ Membrane thickness (m)

δx Differential length (m)

η Dynamic viscosity

R	Thermal resistance (°C/W)
R_{eq}	Equivalent thermal resistance (°C/W)
l	Liter
ρ	Density (kg/m^3)
ε	Membrane porosity
ξ	Membrane tortuosity
c_p	Specific heat of water (J/kg°C)
dz	Differential length along flow direction (m)
h	Heat transfer coefficient (W/m^2.°C)
k	Thermal conductivity (W/m°C)
m_w	Molecular mass of water (kg/mol)
v	Differential cell volume (m^3)
x_{NaCl}	Molar fraction of NaCl salt

14

LIST OF FIGURES

LIST OF TABLES

Chapter 1

Introduction

...Water, water, everywhere,

Nor any drop to drink ...

(—Samuel Taylor Coleridge, *The Rime of the Ancient Mariner*)

1.1 Motivation and Background

Water is essential for the well-being, development, and life of mankind. It is estimated that an average person requires a minimum of 50 liters of fresh water per day for his basic needs. Fresh water is also needed for livestock, agriculture, and industry. However, fresh water only accounts for 2.5% of Earth's water body, with most of it inaccessible in the form of glaciers, snow, and ice [3]. The rapid population growth around the world has increased the demand for fresh water, putting the already limited natural freshwater resources under great pressure. Many water-stressed countries heavily rely on desalination plants to meet the ever increasing fresh water demand. In 2010, it was estimated that about 55% of the total desalinated seawater in the world was produced in Gulf Cooperation Council (GCC) countries [4].

Desalination is the process of removing salts and minerals from saline water to produce water suitable for human consumption, irrigation, or industrial purposes. The objective is always to produce clean water in a cost-effective manner. It is worthwhile to briefly present water classification based on salinity levels, as these levels generally

Table 1.1: Water classification based on salinity levels.

Type	Total Dissolved Solids (ppm)
freshwater	up to 1,500
brackish water	1,500-10,000
Salt water	>10,000
seawater	10,000-45,000
standard sea water	35,000

affect the choice of desalination method and the specific energy requirements. Table 1.1 shows the basic classification.

Desalination techniques can be classified into two categories, depending on whether the feed water goes through a phase change or not. Electro Dialyses process, Microfiltration (MF), Revers Osmosis (RO), and Ultrafiltration (UF), are "membrane-based" pressure-driven desalination methods. On the other hand, Multiple Effect Distillation (MED), Multi-Stage Flash (MSF) desalination, Thermal Vapour Compression (TVC), and Mechanical Vapour Compression (MVC) are examples of "thermal-based" techniques [3].

Membrane Distillation (MD) is an emerging sustainable water desalination method, which combines thermal and membrane-based techniques. In this process, thermal energy is used for phase change of salty feed water while a hydrophobic membrane is used to separate the water vapor from the hot feed solution. The vapor passes through the membrane and to the other side where it condenses and is collected. The mass transfer driving force is the partial vapor pressure difference across the membrane, which is induced by the transmembrane temperature gradient.

MD technology has seen significant advances in the last 50 years, largely due to the development of new and more effective membranes and efficient configurations. In the last decade, attention to the mathematical modeling and sustainable integration of MD with renewable and waste heat sources, and overall system optimization has considerably increased. All of these efforts are capitalizing on the advantages of MD over other desalination methods.

Unlike the well-known RO process, MD operates at a lower hydrostatic pressure and the water temperature is usually between (40-80°C). Therefore, MD requires less energy and can operate on waste heat, solar or another form of renewable energy. As a result, MD is a promising stand alone solution that requires minimal infrastructure for water desalination [5]. There are still several limiting drawbacks to MD however, notably the low production rates when compared to conventional desalination techniques. In addition, like many other membrane-based processes, MD is prone to membrane fouling, which is the result of gradual accumulation of deposited particles onto the membrane surface. Membrane fouling greatly reduces the mass transfer driving force and degrades the MD performance and, if left undetected, can cause system shutdown for cleaning. However, if detected in its early stages, membrane fouling can be dealt with by preventive actions, which saves on operation and maintenance costs. To overcome these limitations, it is important to understand and model the dynamic relations governing the process variables and use the established knowledge in control theory to enhance and optimize the MD process.

This work has three objectives. First, we need to develop a mathematical model of the Direct Contact Membrane Distillation (DCMD) that can be adapted for the process optimization and fouling detection. Then, we extend the proposed model and develop a fouling detection method based on a new adaptive observer design technique. Finally, we propose and implement optimal control techniques to the solar-powered DCMD process.

1.2   Proposed Approach

The main limitation of the current MD water desalination processes is a low freshwater flux compared to conventional thermal and pressure-driven techniques. The thermal efficiency of MD processes is another obstacle. The starting point to deal with these challenges is to develop a deep understanding of the MD process and its intrinsic

variables. Despite that MD has been around for more than half a century [1], accurate and dynamical mathematical models are still lacking in the literature.

Most of the reported models describe the steady-state dimensionless heat and mass transfer phenomena. It is only recently that some studies suggested dynamical models for MD processes. While black-box input-output models of the process are good for simple prediction and analysis, a more useful insight into the process can be obtained from physical modeling. Since MD relies on temperature-driven pressure gradient to produce flux, the temperature through the module varies spatially and over time. This suggests that a Partial Differential Equation (PDE) model would be a suitable mathematical model. However, several limitations of PDE-based models exist. For instance, complex boundary conditions and geometrical domains make it difficult to get a closed-form analytic solution. While, numerical discretization methods may be used to obtain a solution, the resultant system introduces many states that are not observable in practice. This could lead to issues with model controllability and/or observability.

Other alternatives to PDE-based models are lumped capacitance models, which represent a reduced order version of somewhat the equivalent PDE model. These models offer simplicity and practicality while providing the much needed physical insight. In this work, we derive a reduced-order nonlinear differential algebraic equation (DAE) model, based on electrical analogy to thermal systems of one configuration of MD, namely DCMD. This configuration is chosen because of its simplicity and the availability of a DCMD experimental setup in our laboratory at the Water Desalination and Reuse Center (WDRC) at King Abdullah University of Science and Technology (KAUST). In addition, DCMD has the largest number of papers published in refereed journals, according to [1]. Moreover, the proposed model can easily be adapted for other MD configurations. More details and background on the MD process will be presented in the next chapter 2.

To address the challenging problem of membrane fouling, which affects many membrane-based desalination processes including MD, the proposed model is extended to account for this effect. To detect membrane fouling, an adaptive singular observer is designed for this purpose. First, the convergence results and design technique is presented for a general class of nonlinear DAE systems. Then, the proposed design is extended for the specific application of fouling detection in DCMD.

The proposed model accurately predicts the distilled water flux, therefore enabling the design and testing of different control algorithms. This becomes more vital when powering the DCMD process with solar energy and trying to optimize the overall system. We demonstrate, with simulation results, an optimization method which minimizes the energy consumption of a DCMD module while maximizing the output flux. Inspired by the same optimization method, we propose a practical modification to it.

1.3   Contributions

The contributions of this work folds in the following stream:

- Derived a novel methodology for reduced-order dynamic modeling of heat transfer in fluid flow systems based on electrical equivalent thermal networks.

- Developed a reduced-order dynamic model of the DCMD process, which solves directly for the variable of interest and provides a physical insight into the process.

- Implemented a software platform on MATLAB to simulate various setups and operating conditions of DCMD.

- Validated the proposed model against experimentally collected data for various steady-state and dynamic conditions.

- Extended the proposed model of DCMD to account for membrane fouling.

- Developed a new design method for nonlinear adaptive descriptor observers, convergence results are proven by sufficient condition.

- Implemented a method for membrane fouling detection based on adaptive observers, results are presented and discussed.

- Formulated and illustrated an optimal control problem for solar-powered DCMD setup.

- Presented a practical modification of a real-time optimization algorithm called Extremum Seeking (ES), where an ES algorithm with adaptive dither signal amplitude proposed.

In chapter 2, a brief background about several water desalination techniques along with the basic concepts and configurations of the MD process are presented. The proposed model is developed based on mass and energy balance equations in chapter 3. Simulation results for two case studies are considered and discussed in chapter 4. The general design method for nonlinear adaptive descriptor observers is developed in chapter 5. The proposed model of DCMD is extended to account for membrane fouling, and the performance of a specific implementation of the proposed adaptive observer design for fouling detection is demonstrated in chapter 6. A review of two Extremum Seeking (ES) schemes is provided in chapter 7. In addition, the proposed modification to the ES is presented with simulation results compared to the original design. An optimal control problem is formulated for the solar-powered DCMD in chapter 8. Finally, conclusions are drawn and future directions are proposed in chapter 9.

Chapter 2

Membrane Distillation

2.1 Introduction

Membrane Distillation (MD) is a hybrid process where both thermal and membrane separation techniques are combined. In this process, a hot salty stream passes along one side (the feed side) of a microporous hydrophobic membrane, while the other side (the permeate side) of the membrane is kept at a lower temperature. Due to this temperature difference, water evaporates at the feed-membrane interface, and only water vapor passes through the hydrophobic membrane, driven by a differential saturation vapor pressure across the feed and the permeate sides of the membrane. The water vapor then condenses on the permeate side of the membrane [1].

This chapter gives an overview of several desalination techniques and focuses more on MD and its configurations. The mechanism of mass and heat transfer in DCMD is then presented.

2.2 Water Desalination Techniques

Before looking to MD and its configurations, this is a brief background about other desalination techniques based on the adopted separation process.

- Techniques without phase change: These methods usually employ some sort of pressure difference to drive water through a membrane. Reverse Osmosis is the most widely used method among other techniques, like Electro Dialyses, MF,

and UF. MF and UF are best suited for removal of suspended solids or as a pretreatment step for other desalination technologies.

- Revers Osmosis (RO)

  Osmotic pressure naturally drives solvent substance through a selective semi-permeable membrane, i.e. a membrane which retains solutes, from the low concentration side of the membrane (the feed side) into a "draw" solution of high concentration. On the other hand, the RO process applies high pressure at the high concentration side of the membrane to overcome the osmotic pressure, hence the name reverse osmosis.

- <u>Techniques with phase change:</u> These processes typically vaporize the salty feed water to produce freshwater. As a result, a substantial amount of thermal energy is required in these "thermal-based" processes. The two most widely used thermal desalination processes are Multiple Effect Distillation (MED) and Multi-Stage Flash (MSF) desalination, among other techniques like Thermal Vapour Compression (TVC), and Mechanical Vapour Compression (MVC).

  - Multiple Effect Distillation (MED): As the name suggests, this process includes multiple stages, or "effects", where the salty feed water is heated up via steam tubes in each stage. Some of the water evaporates and this vapor is used to heat the next stage feed water and so on. The steam from all the stages is then collected as a freshwater.

  - Multi-Stage Flash (MSF) desalination: In this process, a portion of feed water is flashed into steam by reducing the pressure in the respective stage chamber. Heat is supplied to the feed across multiple stages by counter-current heat exchangers. This process accounts for about 66% of the total desalinated water in the world.

2.3   MD Configurations

Several configurations have been proposed for MD, each with its pros and cons. The four main configurations are:

- Direct Contact Membrane Distillation (DCMD)

- Air Gap Membrane Distillation (AGMD)

- Sweeping Gas Membrane Distillation (SGMD)

- Vacuum Membrane Distillation (VMD)

In all of these configurations, the hot feed solution is always kept in direct contact with one side of the membrane, where vapor forms and passes through to the permeate side. However, the configurations differ according to the mechanism used to condense the water vapor.

2.3.1   Direct Contact Membrane Distillation

DCMD is the simplest MD configuration. Both the feed and permeate solutions are kept in direct contact with the membrane, hence the name direct contact (Fig. 2.1a). Since evaporation and condensation take place at the respective membrane surface, the temperatures at the membrane interfaces are very close to that of the respective bulk steam. This allows for a large temperature drop across the membrane, leading to a higher mass transfer driving force, hence, a greater water flux than other MD configurations. This makes DCMD setup suitable for seawater and brackish water desalination. However, heat losses in DCMD are high since the only barrier between the hot feed and the cooled permeate is the thin membrane [6].
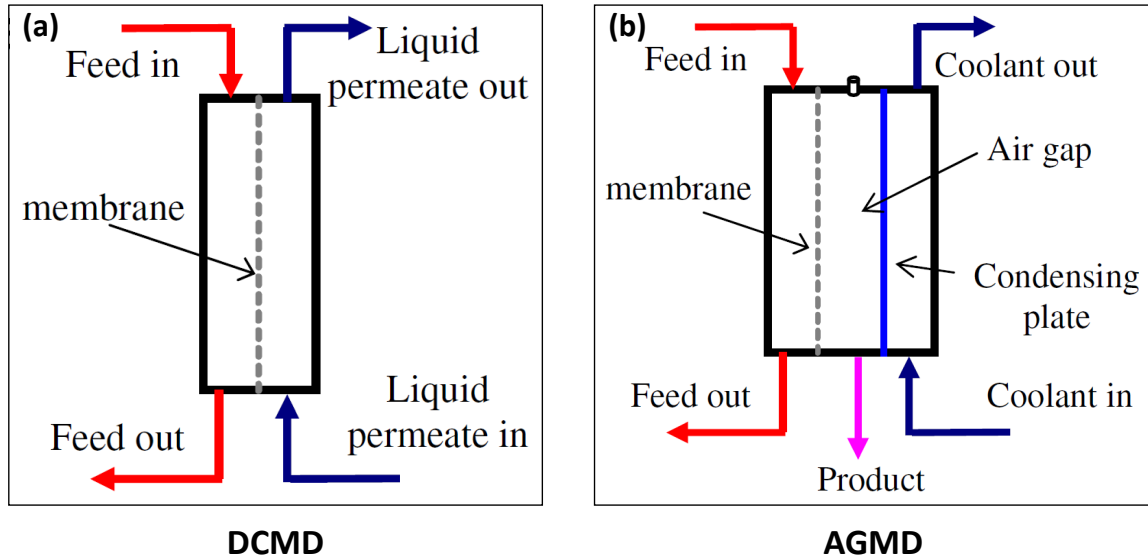
Figure 2.1: Schematic diagram of DCMD and AGMD modules.[1]

2.3.2 Air Gap Membrane Distillation

There are three separate channels in this configuration: the hot feed side, a stagnant air gap channel (permeate side of the membrane), and a coolant circulation stream (Fig.2.1 b). Vapor forms at the feed-membrane interface and passes through the membrane where it condenses on the condensing plate and the flux is collected out from the air gap. This setup reduces the heat losses by introducing the air gap between the membrane and the coolant fluid. The air gap thickness is of great importance, as a larger gap thickness decreases the effective temperature difference across the membrane, thus reducing the distilled water flux. Since the permeate flux is separated from the coolant fluid, the Air Gap Membrane Distillation (AGMD) setup is more convenient for applications such as removal of volatile organic compounds (VOCs) from aqueous solutions. This is an important advantage AGMD has over DCMD [7].

2.3.3 Sweeping Gas Membrane Distillation

This configuration sweeps gas along the membrane-permeate interface, which carries the vapor flux out of the MD module. Therefore, an external condenser has to be
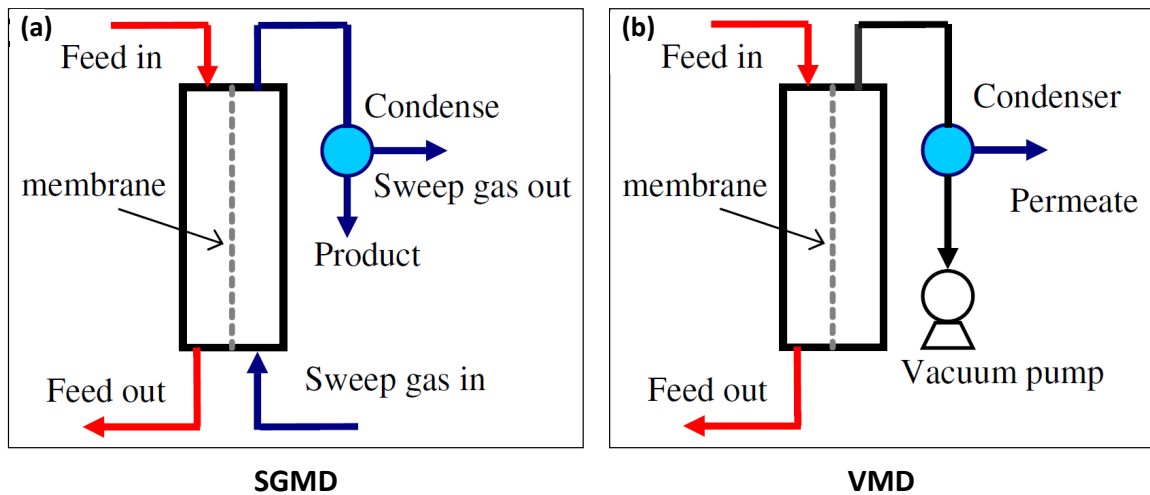
Figure 2.2: Schematic diagram of SGMD and VMD modules.[1]

installed to collect the produced water (Fig. 2.2 a). This setup raises the capital cost of the MD setup by adding the external condenser. However, SGMD reduces the additional mass transfer resistance found in AGMD by continuously circulating dry air along the membrane [8].

2.3.4 Vacuum Membrane Distillation

In this MD configuration, a vacuum is applied on the membrane-permeate interface by a vacuum pump (Fig. 2.2 b). The resultant pressure in the permeate side on the membrane has to be lower than the saturation vapor pressure at the membrane-feed surface to drive the mass transfer through the membrane. Like in SGMD, VMD requires an external condenser to collect the permeate flux. This setup has two advantages: The heat losses by conduction through the membrane are reduced and the effect of the thermal boundary layer at the membrane-permeate interface is negligible because of the low pressure applied at the permeate side of the membrane. In addition, there is a reduced resistant to mass transfer through the membrane, due to the induced vacuum. However, this configuration has a higher risk of pore wetting. This is when the applied vacuum overcomes the liquid entry pressure of the hydrophobic membrane

[9].

2.4   Theoretical Background

Since only water vapor is allowed through the hydrophobic membrane, MD has a 100% theoretical reject rate of ions, making it more appealing than other separation methods for water treatment containing non-volatile solutes [10]. There are several other applications of MD such as seawater desalination [11], and heavy metal removal [12].

Unlike conventional thermal-based desalination methods, MD does not require intensive heat, which means it can be integrated with solar thermal energy and waste heat sources [13, 14]. In addition, since MD operates at a lower hydraulic pressure, it is less susceptible to scaling and fouling; a general drawback of pressure-driven membrane-based desalination techniques, like RO. Moreover, the general operational concept of MD requires demanding membrane characteristics and properties [5]. All these features make MD ideal for sustainable water desalination in remote areas [15].

In the next subsections, the principles of mass and heat transfer in DCMD are presented. The proposed mathematical model is then developed based on lumped capacitance method in the next chapter.

2.4.1   Mass and Heat Transfer in DCMD

A schematic diagram of flat-sheet DCMD module is shown in Fig. 2.3. In this configuration, hot water is passed along one side of a hydrophobic membrane, called the feed, and cold fresh water flows in the counter direction along the other side, which is called the permeate. Both heat and mass transfer processes occur simultaneously as water evaporates at the feed-membrane interface and condenses at the permeate-membrane interface. The transport phenomena are described by the classic gas permeation and heat transfer theories.
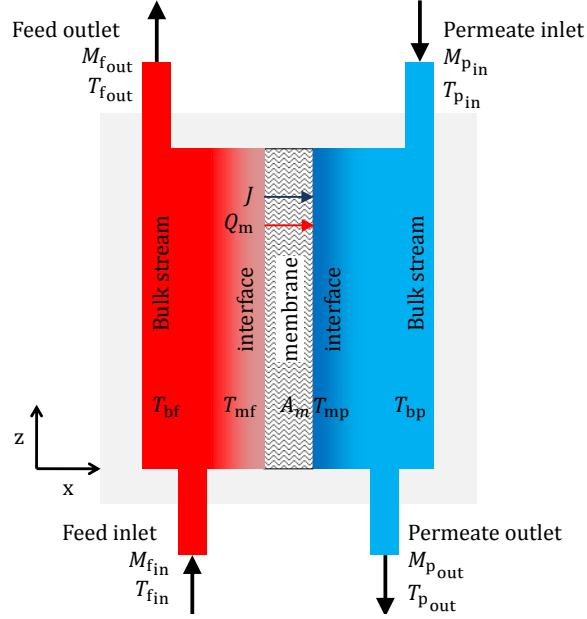
Figure 2.3: Schematic diagram of DCMD module.

Mass Transfer

The temperature difference between the membrane-feed interface (T_{mf}) and membrane-permeate interface (T_{mp}) induces a difference in the saturation vapor pressure (ΔP). The mass flux (J) in DCMD is related to the saturated vapor pressure difference across the membrane through the membrane mass transfer coefficient (B_{m}), as follows [16]:

$$J = B_{\mathrm{m}}\Delta P = B_{\mathrm{m}}\big(P_{\mathrm{mf}} - P_{\mathrm{mp}}\big) \tag{2.1}$$

The mechanism dominating the mass transfer through the porous membranes depends on the pore radius (r) and the mean free path of the vapor molecules (λ). For membranes with pore radius in the range of $0.5\lambda < r < 50\lambda$, the membrane mass transfer coefficient is expressed as a parallel combination of Knudsen diffusion (B_{Kn}) and molecular diffusion (B_D) coefficients [17], given by

$$B_m = \frac{1}{1/B_{Kn} + 1/B_D}, \tag{2.2}$$

where

$$B_{Kn} = \frac{4}{3}\frac{\varepsilon r}{\chi\delta}\sqrt{\frac{2m_w}{\pi\bar{R}T}}, \qquad\qquad B_D = \frac{\varepsilon}{\chi\delta}\frac{PD}{P_a}\frac{m_w}{\bar{R}T}.$$

The saturated vapor pressure of pure water ($P_w^{sat}[T]$) as a function of temperature (in °C) is given by the Antoine equation [18]:

$$P_w^{sat}[T] = \exp\left(23.1964 - \frac{3816.44}{T + 227.02}\right). \tag{2.3}$$

Dissolved salt in the feed stream reduces the saturated vapor pressure. Therefore, to compensate for this, the following relation was proposed in [18]

$$P_{\mathrm{mf}} = (1 - x_{NaCl})(1 - 0.5x_{NaCl} - 10x_{NaCl}^2)P_w^{sat}[T_{\mathrm{mf}}], \tag{2.4}$$

where x_{NaCl} is the mole fraction of NaCl in the feed stream. However, the permeate is pure and the saturated vapor at the membrane-permeate interface is $P_{\mathrm{mp}} = P_w^{sat}[T_{\mathrm{mp}}]$.

Heat Transfer

As the water evaporates at the membrane-feed interface, the temperature drops from that of the bulk-feed stream (T_{bf}), creating a thermal boundary layer. Another boundary layer is formed as the water vapor condenses on the membrane-permeate interface, and thus raising the temperature higher than that of the bulk-permeate stream(T_{bp}). In addition, conduction takes place through the membrane due to the temperature difference. This is known as the temperature polarization effect [18]. In order to quantify this effect, The Temperature Polarization Coefficient (TPC) is defined as:

$$TPC = \frac{T_{\mathrm{mf}} - T_{\mathrm{mp}}}{T_{\mathrm{bf}} - T_{\mathrm{bp}}} \tag{2.5}$$

This effect reduces the mass transfer driving force, lowering the production rate of the DCMD desalination system. Moreover, the temperature of the feed and permeate streams varies along the flow direction from inlet to outlet, due to convection. Therefore, the TPC is not the same along the membrane length. It is essential to model these spatial variations to be able to characterize the mass flux of the DCMD module. Various approaches have been proposed to model heat transfer in DCMD. In the next chapter, we review the current state of the art about MD modeling and motivate and derive the proposed modeling approach.

2.5   Chapter Summary

This chapter gave an overview of several desalination techniques and highlighted the advantages and potential of MD towards sustainable desalination. Then, a brief background about the mass and heat transfer mechanisms was presented. The spatial temperature distribution presents a challenge for model development and accurate prediction of mass flux. In the next chapter, we review the literature on MD modeling and motivate the proposed modeling approach followed by the model development.

Part I

Model Development and Validation

Chapter 3

Reduced-Order Dynamic Modeling of DCMD

3.1 Introduction

Since heat transfer in MD involves several mechanisms, various modeling approaches have been proposed in the literature. From a simple steady-state model without a space dimension, which could be useful to understand the heat transfer across the membrane, to a much detailed computational fluid dynamics model, which may not be very practical for process control. However, as stated before, the objective is to derive a physical model of DCMD that is suitable for process analysis and real-time optimal control. In this chapter, a state of the art literature study on existing models is first presented. Then, we continue with the heat transfer in DCMD and the development of the proposed dynamical model is detailed.

3.2 Related Work

To capitalize on the stated advantages of MD, the water desalination process has to be well understood, modeled, and optimized to maximize the distilled water flux. In recent years, there have been some efforts to model the MD process and understand the effect of its operational parameters. The steady-state space-independent analysis sets the foundation for understanding the process [17, 19]. To capture the steady-state spatial effects on the process, several approaches have been proposed. In [20], energy and mass conservation laws were used to compare the energy efficiency of three MD configurations: DCMD, AGMD, and Vacuum Membrane Distillation (VMD). In [2],

simulations governed by the laminar steady-state Navier-Stokes equations were compared to measurements of DCMD obtained experimentally. A more recent work, [21], based on energy and mass balances was also compared to experimental measurements of a DCMD experimental setup.

However, due to spatial and temporal variations of the temperature distribution inside the MD module and other effects, it is important to learn more about the dynamic response of the process. In addition, when coupling the MD process with renewable energy, the additional challenge of the unsteady nature of the energy source has to be considered as it evolves in time. All of these reasons have motivated the dynamical modeling of the MD [13, 11, 22, 23]. Both [13, 22] considered dynamic Partial Differential Equations (PDEs) to model AGMD and DCMD respectively, whereas [11] proposed a black-box model based on artificial neural networks.

There are two main limitations for most of the reported models: They are either only applicable for steady-state dimensionless analysis or are computationally not suitable for real-time process control and optimization. In contrast to black-box models, physical models offer more insight into the process and its operational parameters (i.e. the feed and permeate inlet temperatures and flow rates as well as the geometry of the module and the membrane properties). It is important to notice that lumped capacitance models [20, 21] have the benefits of physical models while maintaining the potential for real-time control and optimization applications. Our approach builds upon this concept and proposes a dynamical lumped capacitance model based on electrical analogy to thermal systems.

3.2.1 Heat Transfer in DCMD

To consider spatial variations on the temperature along the feed and permeate flow directions, the DCMD module is divided into control-volume cells. Then, based on the lumped capacitance method, a dynamical model for heat transfer is developed
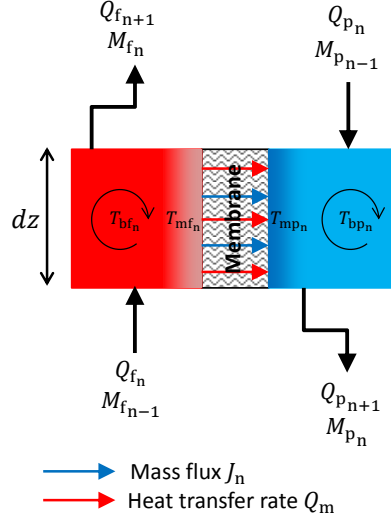
Figure 3.1: Schematic diagram of the nth DCMD cell.

using the energy conservation law.

Fig. 3.1 depicts the nth DCMD cell, where the bulk temperatures (T_{bf_n}, T_{bp_n}) are uniform throughout the cell, except at the membrane interfaces due to the temperature polarization effect, the reader may refer to the List of Symbols for nomenclature description. Therefore within each cell, heat transfer occurs from the feed side to the permeate side and takes place mainly by conduction and due to mass transfer, in three stages. In the first stage, heat is transferred from the hot bulk feed stream to the boundary layer at the feed-membrane interface, the heat transfer rate is expressed as

$$Q_{mf_n} = A_m \big(h_f (T_{bf_n} - T_{mf_n}) + J_n c_p T_{bf_n} \big).$$

The rate of change of the bulk feed stream energy in the nth cell can now be expressed as

$$C_{bf} \frac{d\, T_{bf_n}}{dt} = Q_{f_n} - Q_{f_{n+1}} - A_m \left(h_f (T_{bf_n} - T_{mf_n}) + J_n c_p T_{bf_n} \right), \tag{3.1}$$

where Q_{f_n} and $Q_{f_{n+1}}$ are the heat transfer rate into and out of the nth feed cell respectively.

At the second stage, heat is transferred through the membrane via three mechanisms. The first mechanism (Q_{m1}^n) is the latent heat of vaporization (H_v) transported by the mass flux (J_n) through the nth cell[1], expressed as

$$Q_{m1}^n = A_m J_n H_v[T_{mf_n}] = B_m (P_{mf_n} - P_{mp_n}) H_v[T_{mf_n}], \tag{3.2}$$

where the latent heat of vaporization H_v in (KJ/kg) is expressed as a function of temperature (T in °C):

$$H_v[T] = -2.426\ T + 2503 \tag{3.3}$$

The second and third mechanisms are heat conduction through the membrane material and air trapped in the membrane pores which are combined as

$$Q_{m2}^n = A_m h_m (T_{mf_n} - T_{mp_n}), \tag{3.4}$$

where the membrane heat transfer coefficient (h_m) is the weighted average of thermal conductivity of the membrane material and air, k_m and k_g respectively, given as [5]:

$$h_m = \frac{k_g \varepsilon + k_m (1 - \varepsilon)}{\delta},$$

where ε is the membrane porosity in percentage, and δ is the overall membrane thickness.

Combining these mechanisms to write the energy balance at the membrane interfaces gives the following equation

$$Q_{mf_n} = Q_{mp_n}, \tag{3.5}$$

where the heat transfer rate at the permeate-membrane interface (Q_{mp_n}) is expressed

---

[1]The cell index "n" can be sub-scripted and supper-scripted in this work.

as

$$Q_{mp_n} = A_m \big(h_p(T_{mp_n} - T_{bp_n}) + J_n c_p T_{mp_n} \big) = Q_{m1}^n + Q_{m2}^n. \qquad (3.6)$$

Finally, the third stage of heat transfer where the water-vapor condenses at the permeate-membrane interface and heat is transferred to the bulk permeate mass. The rate of change of energy for the bulk permeate stream is given by

$$C_{bp}\frac{d\,T_{bp_n}}{dt} = Q_{p_n} - Q_{p_{n+1}} + A_m \left(h_p(T_{mp_n} - T_{bp_n}) + J_n c_p T_{mp_n} \right), \qquad (3.7)$$

where Q_{p_n} and $Q_{p_{n+1}}$ are also the heat transfer rate into and out of the nth permeate cell respectively.

The two heat transfer coefficients at the membrane interfaces (h_f, h_p) can be calculated from empirical correlations. These correlations depend on the flow characteristic (laminar or turbulent) and vary accordingly. In this study, the following relation is used for both heat transfer coefficients [17]:

$$h = 0.13 Re^{0.64} Pr^{1/3} \frac{k_w}{D_h}, \qquad (3.8)$$

where Re and Pr are the Reynolds and Prandtl numbers respectively.

Thus far, the analysis has presented the foundation of the proposed modeling method based on energy and mass conservation laws taken on control volume cells along the module length. However, in order to consider the spatial temperature distribution, these cells have to be coupled together to account for the temperature gradient along neighboring cells. More precisely, the heat transfer rates into and out of the nth cell (Q_{f_n}, $Q_{f_{n+1}}$, Q_{p_n}, and $Q_{p_{n+1}}$) has to be quantified. This is enabled by constructing an electrical equivalent thermal network of the DCMD process, based on equations (3.1)-(3.7), as will be discussed in the next section.

3.3 Development of the Electrical Equivalent Thermal Network of DCMD

The dynamical model is based on electrical analogy to thermal systems, which can be derived from the basic laws of each system. Appendix A details the derivation process while a summary of the analogy is shown in Table A.1. Indeed, electrical-analogy based methods have been used to describe the dynamical behavior of many industrial and biological systems such as heat exchangers [24] and the human cardiovascular system [25]. Moreover, it was shown that the transient diffusion phenomena and the heat transfer due to non-steady fluid flow can be described by an electrical analog, see [26] and [27] respectively. The literature above motivated the method presented in this chapter.

Based on the equations derived for the nth DCMD cell, an electrical analog is constructed to simulate heat and mass transfer processes. The electrical analog of the nth cell of the DCMD module is shown in Fig. 3.2. The thermal capacity of the feed and permeate bulk sides is represented by C_{bf} and C_{bp} respectively. In each of the three stages of heat transfer discussed in Section 3.2.1, the heat transfer rate by conduction is proportional to the temperature difference across the thermal resistances R_f, R_m, and R_p, whereas the heat transfer rate due to mass transfer is modeled by the current sources Q_1^n, Q_{m1}^n, and Q_2^n. This completes the analogy of heat transfer within the same cell, and in order to couple neighboring cells, the series impedances (opposition to the heat transfer rate) Z_f^n and Z_p^n are introduced. Apart from the series impedances, Table 3.1 details the expression of each element in the electrical analog circuit.

Another important part of DCMD electrical analogy is to consider the heat transfer by the feed and permeate inlet mass flow rates. Therefore, the electrical analog network should be fed and terminated properly to account for the heat transfer rates into and out of the MD module. This, as well as the series impedances, are fully
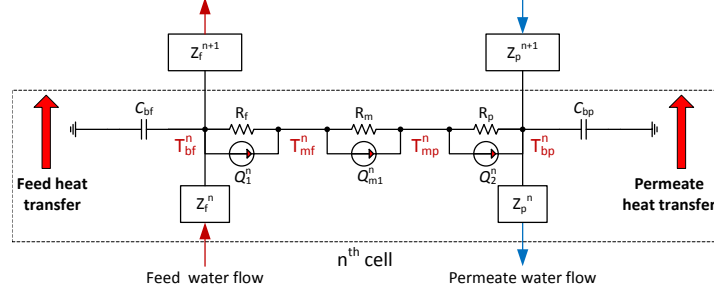
Figure 3.2: Electrical analogue of the nth cell of the DCMD module.

discussed next.

3.3.1 Feeding and Terminating the Network

The feed and permeate inlet temperatures are manipulated by voltage sources ($T_{f_{\text{in}}}$ and $T_{p_{\text{in}}}$, respectively) that can be set as required. This allows to simulate any desired inlet temperature profile. The mass flow rate at the feed inlet ($M_{f_{\text{in}}}$) supplies heat in (Watts) at the rate of

$$Q_{f_{\text{in}}} = Q_{f_1} = M_{f_{\text{in}}} c_p T_{f_{\text{in}}}. \tag{3.9}$$

Therefore, the input impedance of the network should be $1/(M_{f_{\text{in}}} c_p)$ in order for a voltage of $T_{f_{\text{in}}}$ to develop at the feed input terminal of the network.

Table 3.1: Elements of the electrical thermal network for DCMD cell

Element	Expression	Unite
R_f	$\frac{1}{A_m h_f}$	°C/W
R_m	$\frac{1}{A_m h_m}$	°C/W
R_p	$\frac{1}{A_m h_p}$	°C/W
Q_1^n	$A_m J_n c_p T_{bf_n}$	W
Q_{m1}^n	$A_m J_n H_v[T_{mf_n}]$	W
Q_2^n	$A_m J_n c_p T_{mp_n}$	W
C_{bf}	$\rho_w c_p v_{bf}$	J/°C
C_{bp}	$\rho_w c_p v_{bp}$	J/°C

The rate of heat leaving the feed side is given by:

$$Q_{f_{out}} = Q_{f_{N+1}} = M_{f_N} c_p T_{f_{out}}. \tag{3.10}$$

Similarly, for the permeate side, the rate of heat transfer at the outlet is:

$$Q_{p_{out}} = Q_{p1} = M_{p1} c_p T_{p_{out}}. \tag{3.11}$$

However, by conservation of energy, the feed outlet temperature cannot go below the permeate inlet temperature and vice versa, the permeate outlet temperature can't exceed the feed inlet temperature. Based on this argument, the feed and permeate outlet sides are terminated across termination resistances ($R_{f_{term}}$ and $R_{p_{term}}$, receptively) as

$$0 = T_{f_{out}} - T_{p_{in}} - R_{f_{term}} Q_{f_{N+1}}, \tag{3.12}$$

$$0 = T_{p_{out}} - T_{f_{in}} + R_{p_{term}} Q_{p1}. \tag{3.13}$$

where $R_{f_{term}} = \frac{1}{M_{f_N} c_p}$ and $R_{f_{term}} = \frac{1}{M_{p1} c_p}$.

3.3.2 The Series Impedance

In order to simulate the temperature gradient along the membrane in both the feed and permeate sides, adjacent cells are coupled together via the series impedances (Z_f^n and Z_p^n). Careful analysis should be done to design them in order to obtain the correct temperature drop from one cell to the next. As stated in [24], this impedance cannot be determined by direct analogy. However, it is clear that the value of this impedance should be a function of mass flow rates on both feed and permeate sides and the energy lost/received to/from the other side of DCMD module, i.e. the thermal resistance at the membrane interfaces and through the membrane.
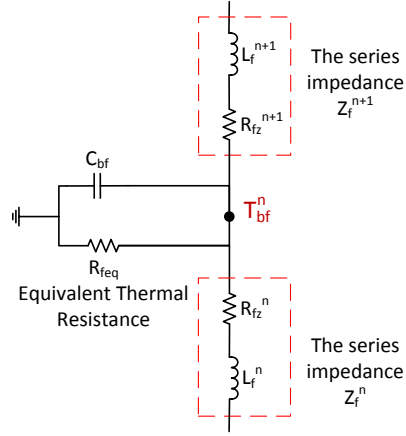
Figure 3.3: Simplified electrical analogue of the feed side.

From the analysis of the constant jacket temperature heat exchanger analog presented in [24], and some intuition as it will be explained, the feed side of the network can be simplified as shown in Fig. 3.3, where an equivalent shunt thermal resistance R_{feq} is introduced. Both the series impedance Z_f^n and the shunt resistance R_{feq} are unknown and to be identified empirically. It is apparent from the analysis in [24] that the resistance R_{fz}^n is inversely proportional to R_{feq} and the square of the mass flow rate M_{f_n}, and takes the following form

$$R_{fz}^n = \frac{1}{M_{f_n}^2 c_p^2 R_{feq}}. \tag{3.14}$$

In order to achieve the correct response from the network, several values of the equivalent shunt thermal resistance R_{feq} were tested and verified against experimental data. Based on that, the following parametrization was found to give the best result:

$$Z_f^n = R_{fz}^n + j\omega L_f^n, \tag{3.15}$$

where

$$R_{fz}^n = \frac{1}{M_{f_n}^2 c_p^2 (R_f + R_m + R_p)}, \quad L_f^n = \frac{R_{fz}^{n\,2} C_{bf}}{4}.$$

The symbol $j\omega$ is used to indicate complex impedance.

The same procedure was used to obtain the parametrization for the permeate side series impedance (Z_p^n) as:

$$Z_p^n = R_{pz}^n + j\omega L_p^n, \tag{3.16}$$

where

$$R_{pz}^n = \frac{1}{M_{p_n}^2 c_p^2 (R_f + 0.5R_m + R_p)}, \quad L_p^n = \frac{R_{pz}^{n\,2} C_{bp}}{4}.$$

Let's explain the idea behind Z_f^n and Z_p^n parametrization. The thermal inertia of the nth cell is modeled by the inductors L_f^n and L_p^n, which account for the dynamic response, while the steady-state response is given by the thermal resistances R_{fz}^n and R_{pz}^n. Heat transfer along the flow direction is significantly affected by the flow inertia because heat is stored in the feed and permeate streams and is transferred by their movements. Therefore, the inductive impedances (L_{fz}^n and L_{pz}^n) resist any sudden changes in the flow momentum and converts potential energy stored in the thermal capacitor to kinetic energy transferred by the stream mass flow rate and vice versa. This oscillatory behavior is damped by the resistances L_f^n and L_p^n.

This concludes the analysis and design of the electrical equivalent thermal network analog of the DCMD setup. In this model, the states are the temperatures in each cell and the heat transfer rates into and out of the cell, the manipulated variables are the inlet feed and permeate water temperatures and flow rates, the controlled variables are the water mass fluxes in each cell which when averaged together represent the overall water mass flux of the DCMD module. In the next section, the equations for the DCMD electrical analogy will be driven from the completed electrical equivalent thermal network circuit.
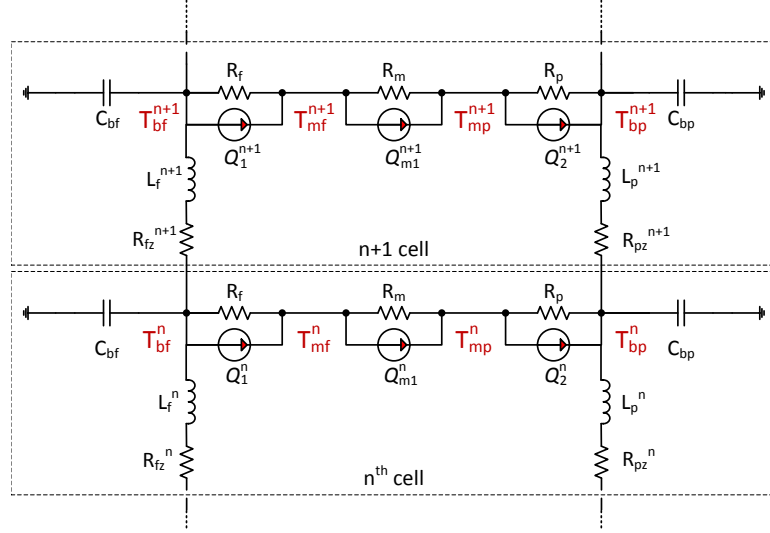
Figure 3.4: Completed electrical equivalent thermal network analogue of the DCMD module.

3.4   Equations of the Electrical Equivalent Thermal Network of DCMD

The elements of the electrical analog network are now properly identified and parameterized, and the complete network is shown in Fig.3.4. Based on this analog circuit, electrical laws are applied to derive the model of DCMD.

The heat transfer rates into and out of the nth cell (Q_{f_n}, $Q_{f_{n+1}}$, Q_{p_n}, and $Q_{p_{n+1}}$) can now be quantified to derive the coupling between neighboring cells. Recall that current in thermal analogy is the heat transfer rate which is flowing through the series impedance from one cell to the next. At the feed side, the rate of change of the heat transfer rate from the $n-1$ cell to the nth cell is proportional to the temperature difference between them. Taking into consideration the series impedance Z_n^f, this is expressed as:

$$\frac{d\,Q_{f_n}}{dt} = \frac{1}{L_f^n}T_{bf_{n-1}} - \frac{R_{fz}^n}{L_f^n}Q_{f_n} - \frac{1}{L_f^n}T_{bf_n}. \tag{3.17}$$

Applying conservation of energy at the nth feed cell, the rate of change of the bulk

feed water equals the rate of energy entering the cell minus the rate of energy leaving the cell. This is also expressed by Kirchoff's current law at the nth node of the ETN. It follows that the rate of change for the bulk feed temperature (T_{bf_n}) is

$$\frac{d\,T_{bf_n}}{dt} = \frac{1}{C_{bf}}Q_{f_n} - \frac{1}{C_{bf}}\left(\frac{1}{R_f} + J_n A_m c_p\right)T_{bf_n} - \frac{1}{C_{bf}}Q_{f_{n+1}} + \frac{1}{C_{bf}R_f}T_{mf_n}. \qquad (3.18)$$

Notice that (3.18) is equivalent to (3.1), but now (3.17) describes the dynamics of the heat transfer rates into and out of the nth feed cell $(Q_{f_n}$ and $Q_{f_{n+1}}$ respectively).

Similarly for the permeate side, the rate of change of the heat transfer rate (Q_{p_n}) is

$$\frac{d\,Q_{p_n}}{dt} = \frac{1}{L_p^n}T_{bp_{n-1}} - \frac{R_{pz}^n}{L_p^n}Q_{p_n} - \frac{1}{L_p^n}T_{bp_n}, \qquad (3.19)$$

and the dynamics of the bulk permeate temperature (T_{bp_n}) is

$$\frac{d\,T_{bp_n}}{dt} = \frac{1}{C_{bp}}Q_{p_n} - \frac{1}{C_{bp}R_p}T_{bp_n} - \frac{1}{C_{bp}}Q_{p_{n+1}} + \frac{1}{C_{bp}}\left(\frac{1}{R_p} + J_n A_m c_p\right)T_{mp_n}. \qquad (3.20)$$

The coupling between the feed and the permeate dynamics in the nth cell is established through the algebraic constraints (3.5) and (3.6), which are written in residue form as

$$0 = \left(\frac{1}{R_f} + J_n A_m c_p\right)T_{bf_n} - \frac{1}{R_f}T_{mf_n} - \left(\frac{1}{R_p} + J_n A_m c_p\right)T_{mp_n} + \frac{1}{R_p}T_{bp_n}, \qquad (3.21)$$

$$0 = \left(\frac{1}{R_m} + \frac{1}{R_p} + J_n A_m c_p\right)T_{mp_n} - \frac{1}{R_p}T_{bp_n} - J_n A_m H_v[T_{mf_n}] - \frac{1}{R_m}T_{mf_n}. \qquad (3.22)$$

The outlet temperatures at the terminal cells of the feed and permeate analog are also given by the algebraic equations (3.12) (3.13).

The heat and mass transfer equations (3.12)-(3.22) represent a nonlinear system of Differential Algebraic Equation (DAE). When considering a total number of N interconnected cells, the resultant equations can be expressed as a nonlinear descriptor

(or DAE) system of the form

$$EX\dot{}(t) = F\big(X(t), u(t)\big)X + B\big(u(t)\big), \tag{3.23}$$

$$y = \begin{bmatrix} CX \\ G \end{bmatrix} \tag{3.24}$$

where $X \in \mathbb{R}^{6N+4}$ represents the differential and algebraic states, $\dot{X}$ refers to the time derivative of the state vector, E is singular, $rank[E] < 6N+4$, and is called the mass matrix, $F\big(X(t), u(t)\big) \in \mathbb{R}^{6N+4 \times 6N+4}$ is nonlinear in the states and input, $B\big(u(t)\big) \in \mathbb{R}^{6N+4}$ represents the input channels into the system, which are the feed and permeate inlet temperatures and mass flow rates ($T_{f_{in}}$, $T_{p_{in}}$, $M_{f_{in}}$, $T_{p_{in}}$. In physical setups, the measurable outputs of this model are the feed and permeate outlet temperatures ($T_{f_{out}}$, $T_{p_{out}}$), which can be linearly inferred from the state vector X by the matrix $C \in \mathbb{R}^{2 \times 6N+4}$, and water production rate(G in kg/hr), which is a nonlinear function of the states. This block matrix representation of (3.23) is further detailed in the next section.

3.5   Descriptor Representation of the DCMD Model

This representation is computationally efficient to solve the nonlinear DAE system and enables the number of total cells (N) to be chosen as desired. In order to take advantage of a tridiagonal structure of (3.23), the state vector X combines both differential and algebraic states in the following order:

$$X = [\quad Q_{f_1}, T_{bf_1}, \ldots, T_{bf_N}, Q_{f_{N+1}}, Q_{p_1}, T_{bp_1}, \ldots, T_{bp_N}, Q_{p_{N+1}}, \tag{3.25}$$

$$T_{f_{out}}, T_{p_{out}}, T_{mf_1}, \ldots, T_{mf_N}, T_{mp_1}, \ldots, T_{mp_N}]^T. \tag{3.26}$$

As a result, the matrix E is the singular mass matrix, given as:

$$
E = \begin{bmatrix} I_{4N+2 \times 4N+2} & \mathbf{0} \\ \mathbf{0} & \mathbf{0}_{2N+2 \times 2N+2} \end{bmatrix},
$$
(3.27)

where I is the identity matrix and $\mathbf{0}$ is the zero matrix of appropriate size.

The matrix $F\big(X(t), u(t)\big)$ represents the nonlinear dynamics of (3.23) and is composed of several blocks which account for the dynamics of the feed and permeate sides along with the algebraic coupling between them, the symbol Z refers to a block matrix for algebraic variables.

$F\big(X(t), u(t)\big)$ is given as

$$
F\big(X(t), u(t)\big) = \begin{bmatrix} A_f & \mathbf{0} & Z_{f1} & Z_{f2} & \mathbf{0} \\ \mathbf{0} & A_p & Z_{p1} & \mathbf{0} & Z_{p2} \\ T_{f_o} & T_{p_o} & I & \mathbf{0} & \mathbf{0} \\ Z_1 & Z_2 & \mathbf{0} & Z_3 & Z_4 \\ \mathbf{0} & Z_5 & \mathbf{0} & Z_6 & Z_7 \end{bmatrix}
$$
(3.28)

where

$A_f \in \mathbb{R}^{2N+1 \times 2N+1}$: Tridiagonal matrix representing the feed differential dynamics.

$Z_{f1} \in \mathbb{R}^{2N+1 \times 2}$: Feed last cell

$Z_{f2} \in \mathbb{R}^{2N+1 \times N}$: Coupling to the membrane-feed interface

$A_p \in \mathbb{R}^{2N+1 \times 2N+1}$: Tridiagonal matrix representing the permeate differential dynamics.

$Z_{p1} \in \mathbb{R}^{2N+1 \times 2}$: Permeate first cell

$Z_{p2} \in \mathbb{R}^{2N+1 \times N}$: Coupling to the membrane-premeate interface

$T_{f_o} \in \mathbb{R}^{2 \times 2N+1}$: Outlet temperature of the feed

$T_{p_o} \in \mathbb{R}^{2 \times 2N+1}$: Outlet temperature of the premeate

$I \in \mathbb{R}^{2\times2}$: The identity matrix.

$Z_1 \in \mathbb{R}^{N\times2N+1}$: Sparse matrix

$Z_2 \in \mathbb{R}^{N\times2N+1}$: Sparse matrix

$Z_3 \in \mathbb{R}^{N\times N}$: Diagonal matrix

$Z_4 \in \mathbb{R}^{N\times N}$: Diagonal matrix

$Z_5 \in \mathbb{R}^{N\times2N+1}$: Sparse matrix

$Z_6 \in \mathbb{R}^{N\times N}$: Diagonal matrix

$Z_7 \in \mathbb{R}^{N\times N}$: Diagonal matrix

The matrix $B\big(u(t)\big)$ is a nonlinear function of the manipulated variables $(M_{\mathrm{f_{in}}},\ M_{\mathrm{P_{in}}},$ $T_{f_{in}},\ T_{p_{in}})$. For convenient representation, the matrix is indexed at the left side:

$$
B\big(u(t)\big) =
\begin{array}{c}
1 \\ 2 \\ \vdots \\ \\ 4N+2 \\ \\ \vdots \\ 6N+4
\end{array}
\begin{bmatrix}
8\ a_2\ M_{\mathrm{f_{in}}}^4 & 0 \\
0 & 0 \\
\vdots & \vdots \\
0 & 0 \\
0 & -8\ a_7\ M_{\mathrm{P_{in}}}^4 \\
0 & 0 \\
\vdots & \vdots \\
0 & 0
\end{bmatrix}
\begin{bmatrix}
T_{\mathrm{f_{in}}} \\
T_{\mathrm{P_{in}}}
\end{bmatrix}.
\tag{3.29}
$$

The elements of the $F\big(X(t), u(t)\big)$ are detailed as follows. The tridiagonal matrices A_f and A_p are specified by tridiag(A_f) and tridiag(A_p), which refer to the three diagonal vectors of A_f and A_p. Each column is a diagonal vector, starting from the lower, main, and then upper diagonal vector respectively.

$$
\mathrm{tridiag}(A_f) = \begin{bmatrix}
 & -4a_1\ M_{\mathrm{f_{in}}}^2 & -8a_2\ M_{\mathrm{f_{in}}}^4 \\
a_5 & -a_3\ J_1 - a_4 & -a_5 \\
4a_2\ M_{\mathrm{f_1}}^4 & -4\ a_1\ M_{\mathrm{f_1}}^2 & -4a_2\ M_{\mathrm{f_1}}^4 \\
\vdots & \vdots & \vdots \\
4a_2\ M_{\mathrm{f_{N-1}}}^4 & -4a_1\ M_{\mathrm{f_{N-1}}}^2 & -4a_2\ M_{\mathrm{f_{N-1}}}^4 \\
a_5 & -a_3\ J_{\mathrm{N}} - a_4 & -a_5 \\
8a_2\ M_{\mathrm{f_N}}^4 & -4a_1\ M_{\mathrm{f_N}}^2 &
\end{bmatrix},
$$

$$
\mathrm{tridiag}(A_p) = \begin{bmatrix}
 & -4a_6\ M_{\mathrm{p_1}}^2 & -8a_7\ M_{\mathrm{p_1}}^4 \\
a_9 & -a_8 & -a_9 \\
4a_7\ M_{\mathrm{p_2}}^4 & -4\ a_6\ M_{\mathrm{p_2}}^2 & -4a_7\ M_{\mathrm{p_2}}^4 \\
\vdots & \vdots & \vdots \\
4a_7\ M_{\mathrm{p_N}}^4 & -4a_6\ M_{\mathrm{p_N}}^2 & -4a_7\ M_{\mathrm{p_N}}^4 \\
a_9 & -a_8 & -a_9 \\
8a_7\ M_{\mathrm{p_{in}}}^4 & -4a_6\ M_{\mathrm{p_{in}}}^2 &
\end{bmatrix},
$$

$$
Z_{f1} = \begin{bmatrix}
0 & 0 \\
\vdots & \vdots \\
0 & 0 \\
-8a_2\ M_{\mathrm{f_N}}^4 & 0
\end{bmatrix}, \quad
Z_{f2} = \begin{bmatrix}
0 & 0 & \ldots & 0 \\
a_4 & 0 & \ldots & 0 \\
0 & 0 & \ldots & 0 \\
0 & a_4 & \ldots & 0 \\
\vdots & \vdots & \ddots & \vdots \\
0 & 0 & \ldots & 0 \\
0 & 0 & \ldots & a_4 \\
0 & 0 & \ldots & 0
\end{bmatrix},
$$

$$
Z_{p1} = \begin{bmatrix} 0 & 8\,a_7\,M_{\mathrm{p1}}^4 \\ 0 & 0 \\ \vdots & \vdots \\ 0 & 0 \end{bmatrix}, \quad
Z_{p2} = \begin{bmatrix} 0 & 0 & \ldots & 0 \\ a_{10}\,J_1 + a_8 & 0 & \ldots & 0 \\ 0 & 0 & \ldots & 0 \\ 0 & a_{10}\,J_2 + a_8 & \ldots & 0 \\ \vdots & \vdots & \ddots & \vdots \\ 0 & 0 & \ldots & 0 \\ 0 & 0 & \ldots & a_{10}\,J_{\mathrm{N}} + a_8 \\ 0 & 0 & \ldots & 0 \end{bmatrix},
$$

$$
T_{f_o} = \begin{bmatrix} 0 & \ldots & 0 & -\frac{1}{M_{\mathrm{f_N}}\,c_p} \\ 0 & \ldots & 0 & 0 \end{bmatrix}, \qquad\qquad
T_{p_o} = \begin{bmatrix} 0 & 0 & \ldots & 0 \\ \frac{1}{M_{\mathrm{p1}}\,c_p} & 0 & \ldots & 0 \end{bmatrix},
$$

$$
Z_1 = \begin{bmatrix} 0 & \frac{1}{\mathrm{R_f}} + a_{11}\,J_1 & 0 & \ldots & 0 \\ 0 & 0 & \ddots & 0 & 0 \\ 0 & \ldots & 0 & \frac{1}{\mathrm{R_f}} + a_{11}\,J_{\mathrm{N}} & 0 \end{bmatrix}, \qquad
Z_2 = \begin{bmatrix} 0 & \frac{1}{\mathrm{R_p}} & 0 & \ldots & 0 \\ 0 & 0 & \ddots & 0 & 0 \\ 0 & \ldots & 0 & \frac{1}{\mathrm{R_p}} & 0 \end{bmatrix},
$$

$$
Z_3 = \begin{bmatrix} -\frac{1}{\mathrm{R_f}} & 0 & \ldots & 0 \\ 0 & -\frac{1}{\mathrm{R_f}} & \ddots & \vdots \\ \vdots & \ddots & \ddots & 0 \\ 0 & \ldots & 0 & -\frac{1}{\mathrm{R_f}} \end{bmatrix},
$$

$$
Z_4 = \begin{bmatrix} -\frac{1}{\mathrm{R_p}} - a_{11}J_1 & 0 & \ldots & 0 \\ 0 & -\frac{1}{\mathrm{R_p}} - a_{11}J_2 & \ddots & \vdots \\ \vdots & \ddots & \ddots & 0 \\ 0 & \ldots & 0 & -\frac{1}{\mathrm{R_p}} - a_{11}J_{\mathrm{N}} \end{bmatrix},
$$

$$
Z_5 = \begin{bmatrix} 0 & -\frac{1}{R_p} & 0 & \cdots & 0 \\ 0 & 0 & \ddots & 0 & 0 \\ 0 & \cdots & 0 & -\frac{1}{R_p} & 0 \end{bmatrix}.
$$

The diagonal vectors of Z_6 and Z_7 are $\mathrm{diag}(Z_6)$ and $\mathrm{diag}(Z_7)$ respectively, which are given as

$$
\mathrm{diag}(Z_6) = \begin{bmatrix} -\frac{1}{R_m} - A_m H_v [T_{\mathrm{mf}_1}] J_1 \\ -\frac{1}{R_m} - A_m H_v [T_{\mathrm{mf}_2}] J_2 \\ \vdots \\ -\frac{1}{R_m} - A_m H_v [T_{\mathrm{mf}_N}] J_N \end{bmatrix}, \qquad \mathrm{diag}(Z_7) = \begin{bmatrix} \frac{1}{R_m} + \frac{1}{R_p} + a_{11} J_1 \\ \frac{1}{R_m} + \frac{1}{R_p} + a_{11} J_2 \\ \vdots \\ \frac{1}{R_m} + \frac{1}{R_p} + a_{11} J_N \end{bmatrix}.
$$

The parameters a_1 to a_{11} are

$$
a_1 = \frac{c_p^2 R_{\mathrm{feq}}}{C_{\mathrm{bf}}} \qquad\qquad a_2 = \frac{c_p^4 R_{\mathrm{feq}}^2}{C_{\mathrm{bf}}}
$$

$$
a_3 = \frac{A_m c_p}{C_{\mathrm{bf}}} \qquad\qquad a_4 = \frac{1}{C_{\mathrm{bf}} R_f}
$$

$$
a_5 = \frac{1}{C_{\mathrm{bf}}} \qquad\qquad a_6 = \frac{c_p^2 R_{\mathrm{peq}}}{C_{\mathrm{bp}}}
$$

$$
a_7 = \frac{c_p^4 R_{\mathrm{peq}}^2}{C_{\mathrm{bp}}} \qquad\qquad a_8 = \frac{1}{C_{\mathrm{bp}} R_p}
$$

$$
a_9 = \frac{1}{C_{\mathrm{bp}}} \qquad\qquad a_{10} = \frac{A_m c_p}{C_{\mathrm{bp}}}
$$

$$
a_{11} = A_m c_p
$$

where

$$
R_{\mathrm{feq}} = R_f + R_m + R_p
$$

$$
R_{\mathrm{peq}} = R_f + 0.5 R_m + R_p
$$

The mass flow rates (M_{f_n} and M_{p_n}) coming out of the nth cell are indexed

$$M_{f_n} = M_{f_{n-1}} - A_m \ J_n; \quad n = 2, 3, \ldots, N$$

$$M_{p_n} = M_{p_{n+1}} + A_m \ J_n; \quad n = 1, 2, \ldots, N - 1$$

where as

$$M_{f_1} = M_{f_{in}} - A_m \ J_1$$

$$M_{p_N} = M_{p_{in}} + A_m \ J_N$$

3.6   Chapter Summary

Membrane distillation is a thermally driven process where only water vapor is passed through a hydrophobic membrane. Several models have been proposed to study this process, yet most of them assume steady-state conditions. This work presents a novel approach to model Direct Contact Membrane Distillation (DCMD) dynamics based on the analogy between electrical and thermal systems. A distributed lumped capacitance dynamical model accounting for mass, energy, and momentum balance was derived and simulated. Counter-current flow setup was considered under various conditions. This model is promising and can be extended to other MD configurations. More details about the MATLAB implementation and the model performance and validation results are discussed in the next chapter 4.

Chapter 4

Model Validation Results

4.1   Introduction

This chapter presents validation results of the proposed model. The validation has been carried out for two case studies. First, we discuss the MATLAB implementation of this model and the developed software. Then simulation results for the two case studies along with the effect of some operational parameters on the process are discussed.

4.2   MATLAB Implementation

The proposed model is implemented with MATLAB [28] environment. A software has been developed which can be easily adjusted to simulate various DCMD experimental setups and modules, i.e. the membrane characteristics and the module dimensions. This is very important for process scale-up studies and performance evaluation under various operating conditions. Also, The feed and permeate mass flow rates and inlet temperatures can follow any desired time-varying profiles. The desired level of accuracy can be achieved by varying the total number of cells (N). A total number of cells between 3 and 10, depending on the module size, gives accurate results.

The model is simulated using `ode15s` MATLAB solver, which uses an adaptive integration step size based on the user defined tolerance. This solver accepts a mass matrix, which in this case is a square singular matrix to identify the differential equations and the algebraic constraints. At the beginning of each simulation run, the

module dimensions and membrane properties and other experimental setting were set as required. Then, the `ode15s` solver is called with relative parameters, such as the simulation duration, and the feed and permeate inlet temperatures and velocities. Inside the ode15s function, the DAE model is constructed and model parameters are updated if necessary as some parameters are temperature dependent. For example, water properties, like density and dynamic viscosity are interpolated for both the feed and permeate streams depending on the average temperature between the inlet and outlet of each channel, so there is one value for the feed side and another one for the permeate side. Also, the membrane mass transfer coefficient and the heat transfer coefficients at the membrane interface layers are updated according to the temperature and flow rate conditions, respectively. Once the simulation passes the first seconds of a transient response, the adaptive solver increases the step size. Therefore, simulation results can be obtained relatively fast.

In order to validated the proposed dynamic model of DCMD, simulations were carried out for two case studies:

- **Case 1:** An experimental data set that is reported in the literature, see [2], providing steady-state flux and temperature measurements.

- **Case 2:** An experimental data set, provided by the WDRC at KAUST, for the steady-state and dynamic response of the flux and feed outlet temperature.

4.3   Case 1 Results

This experimental data, reported in [2], is chosen to validate the simulation results of the proposed model because it tests various aspects and criteria of the DCMD operation as well be presented in the following three tests.
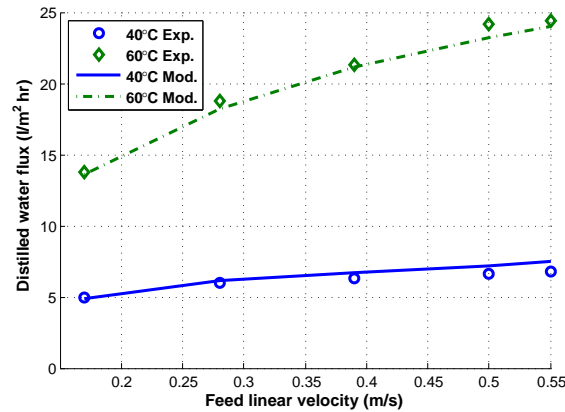
Figure 4.1: Flux as a function of feed linear velocity. Experimental data (Exp.) extracted from [2] compared to modeling results (Mod.) for different linear velocities.

4.3.1 Test 1:

Effect of linear velocity on distilled water flux

The distilled water flux is a function of the partial vapor pressure difference across the membrane, which is expressed as a function of temperature. The linear velocity inside the feed and permeate channels have a significant effect on the heat transfer from the bulk stream to the membrane boundary layer, where higher velocity reduces the thickness of the thermal boundary layer and the temperature polarization effect is reduced. Therefore, it is important to study the relation between the feed/permeate stream velocity on the distilled water flux.

This effect was investigated for two feed inlet temperatures, 60°C and 40°C and permeate inlet temperature of 20°C for both cases. The feed and permeate stream velocities were increased from 0.17 m/s to 0.55 m/s and the distilled water flux was recorded. Fig. 4.1 presents the results obtained from the simulated electrical analog compared to the experimental data reported in [2]. As it was expected, the flux increased with higher velocities. Also, higher values of flux are achieved with higher feed inlet temperatures. This is due to the exponential increase in the mass transfer driving force. It is clear that the modeling results agree with the experimental values

of flux under the two different feed inlet temperatures with less than 10% difference between them.

4.3.2 Test 2:
Effect of linear velocity on feed and permeate outlet temperatures

Another criterion to validate the model is to compare the feed and permeate outlet temperatures to the experimental measurements reported in [2]. Table 4.1 shows the outlet temperatures obtained from simulating the model with five feed and permeate linear velocities starting from 0.17 m/s to 0.55 m/s compared to the experimental data with these conditions: 1% NaCl concentration, and counter current flow setup. The model results are accurate to less than 3% error.

57

Table 4.1: Validation of the feed and permeate outlet temperatures under various inlet flow linear velocities. The experimental values are reported in [2] compared to the simulation results of the proposed model. The experiment is setup as counter-current flow, feed inlet temperature of 60°C, permeate inlet temperature of 20°C, and NaCl concentration of 1%).

velocity (m/s)	Feed outlet temperature °C			Permeate outlet temperature °C		
	Experimental	Simulation	% error	Experimental	Simulation	% error
0.17	50.1	49.58	1.04	29.1	28.62	1.65
0.28	52.1	52.36	0.11	27.4	28.08	2.48
0.39	53.9	54.06	0.3	26.3	26.67	1.40
0.5	55.1	55.16	0.11	25.8	25.52	1.09
0.55	55.3	55.54	0.43	25.4	25.09	1.22

Figure 4.2: Temperature distribution along the flow in the feed and permeate sides.

4.3.3 Test 3:

Temperature distribution along flow direction

The temperature distribution along the flow direction was simulated for the following settings: counter-current flow, feed and permeate linear velocity of 0.5 m/s, feed inlet temperature of 60°C, permeate inlet temperature of 20°C, and feed NaCl concentration of 1%. The ETN model results are presented in Fig. 4.2. This temperature distribution agrees with the experimental data seen in [2]-Fig.8(b).

4.4 Case 2 Results

Two kinds of experiments were conducted by the WDRC to further validate the proposed model, one under steady-state conditions and the other for a ramp of the feed inlet temperature. The experimental setup is first presented followed by a description of the steady-state and dynamic experiments. Finally, the simulation results for both experiments are shown.
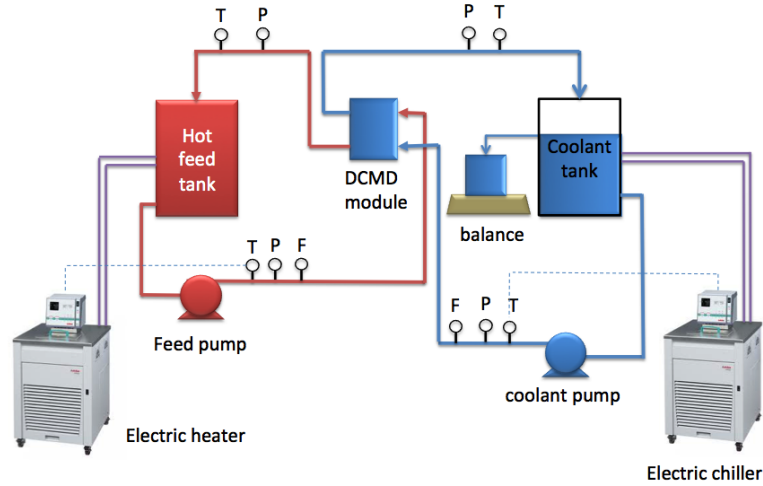
Figure 4.3: A schematic diagram of the experimental lab scale setup.

Table 4.2: DCMD Module Parameters

Property	Value
Active area	0.005 m^2
Total thickness	0.170 mm
Pore size	0.27 μm
Porosity	77%
Tortuosity	1.35 μm
Liquid Entry Pressure	15 psi
Contact angle	140 $\pm$3°

4.4.1 Experimental Setup and Materials

The DCMD lab scale setup used in this experimental work was locally designed and fabricated at KAUST [29]. A schematic diagram of the setup is presented in Figure 4.3. All experimental runs were conducted in a 0.1 m × 0.05 m × 0.003 m flat sheet membrane module made of Poly Methyl Methacrylate (PMMA) material. A composite membrane with a polytetrafluoroethylene (PTFE) active layer and a non-woven polypropylene support layer was used in all experiments. Details of the membrane characteristics and its performance for seawater desalination were widely reported in previous works, e.g. [30, 29, 31]. Some of these parameters are presented in Table 4.2.

For the steady-state experiments, Red Sea water was preheated to the desired

temperature and circulated through the feed side of the membrane, while deionized (DI) water was circulated through the other side of the membrane simultaneously in a counter-current mode. The inlet feed and coolant temperatures were controlled using thermo-regulators. Four experiments were carried out, at various feed inlet temperatures ($40°C$, $50°C$, $60°C$, and $70°C$). Fresh seawater was used for each experiment.

For the time-varying response experiment, the influence of feed water temperature ranging from $30°C$ to $68°C$ on trans-membrane flux was also studied by ramping the feed inlet temperature at a rate of $0.05°C$ per minute. During the ramping experiment, the coolant temperature was also maintained at $20°C$.

For all experiments, the feed and coolant flow rates were kept constant at 90 liters/hr and 60 liters/hr, respectively. The inlet and outlet temperatures of the feed and coolant side were measured by thermocouple sensors with an accuracy of $\pm 1.0°C$. The water-vapor flux produced by the DCMD process increases the volume of water in the coolant tank and, as a result, overflow occurs through an outlet of the coolant tank. To measure the water-vapor flux, the overflow was collected in a separate container placed on a weighing balance (Mattler Toledo NewClassic ML 3200g) with an accuracy of 0.02 g. The increase in weight of the container was continuously monitored and recorded. All measurements were fed through a data acquisition unit into an NI LabView software. The conductivity of the coolant and feed solutions was continuously monitored and measured using conductivity meters (Oakton Eutech Instruments, Malaysia) with multiple ranges (0 to 20, 20 to 200, 200 to 2000 $\mu S/cm$; and 0 to 20.00, 20 to 200 mS/cm) and an accuracy of $\pm 1\%$ of the full scale.
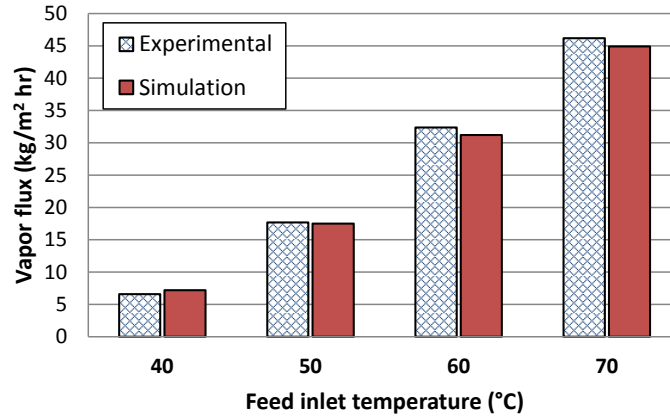
Figure 4.4: Distilled water flux at different feed inlet temperatures.

4.4.2 Steady-state Flux Validation at Various Feed Inlet Temperatures

One of the main factors contributing to the flux in DCMD is the feed inlet temperature. It is important to demonstrate that the proposed model is capable of accurately forecasting the vapor flux at different feed inlet temperatures.

4.4.3 Dynamic Validation of the Flux and Feed Outlet Temperature

Fig. 4.5 depicts the simulated and experimental feed outlet temperature, where it is clear that the simulation results closely match the experimental data and within the sensor tolerance. The water vapor flux was recorded by a sensitive electrical scale, which could be prone to random error or noise. Despite this, we see that the simulation results follow the trend of the experimental data closely as in Fig. 4.6. Since the vapor flux is a nonlinear function of the trans-membrane temperature difference, we notice an exponential increase in the flux with respect to the feed inlet temperature.

Based on the validation results obtained for both the steady-state and dynamic responses, the same model can be used to solve for intrinsic variables that are not
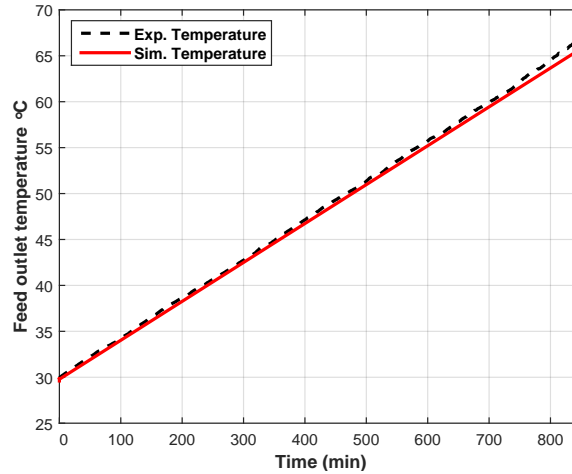
Figure 4.5: Feed outlet temperature for a ramp feed inlet temperature from 30°C to 68°C. Dash is experimental measurements, line is simulation results.
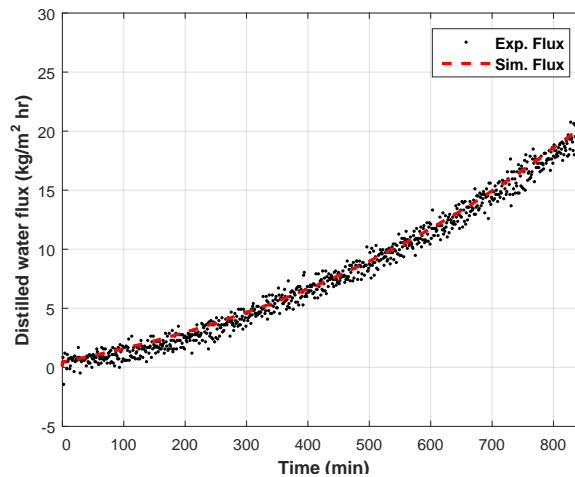
Figure 4.6: Distilled water flux for a ramp feed inlet temperature from 30°C to 68°C. Dots are experimental measurements, line is simulation results.

accessible in the physical setup. For instance, in the time varying ramp experiment, the average pressure differential grows exponentially with respect to the linear increase in the feed inlet temperature, see Fig.4.7.

4.5   DCMD Process Analysis and Discussion

Based on the excellent validations results, we propose to use the same model to carry out design and scale-up studies. As stated before, the proposed model estimates and
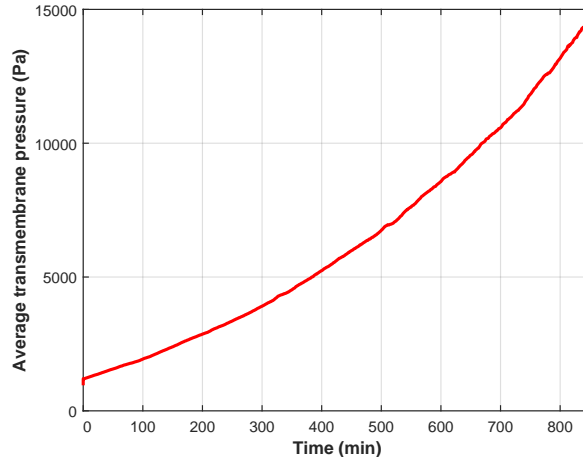
Figure 4.7: The average pressure differential across the membrane predicted over time for a ramp feed inlet temperature from 30°C to 68°C. This shows an exponential relationship between the feed inlet temperature and pressure differential.

solves for intrinsic variables that are not accessible in the physical setup. In the next subsections, we analyze and discuss the effects of various operating conditions on the DCMD process.

4.5.1 Step responses of the DCMD process

An important advantage of the proposed model is the ability to obtain the time response under dynamic changes in the DCMD process. In this simulation the module dimensions are set as follows: length 5m, width 0.4m, channel thickness 0.003m. The feed and permeate inlet velocities are kept constant at 0.4 m/s, the permeate inlet temperature is set to 20°C, while the feed inlet temperature is stepped from 50°C to 60°C at time t=15s. The time response of the feed-bulk temperature distribution over the module length is depicted in Fig. 4.8, where each curve shows the temperature distribution at a given time instant. Starting from the lowest blue curve at t=15s, the module takes 12.5s in response time to reach the upper red curve which shows the new steady state temperature distribution. Fig. 4.9 shows the step response of the bulk-feed and membrane-feed interface temperatures at the cell corresponding to 1.75 m from the feed inlet. Notice that the DCMD process response is relatively fast,
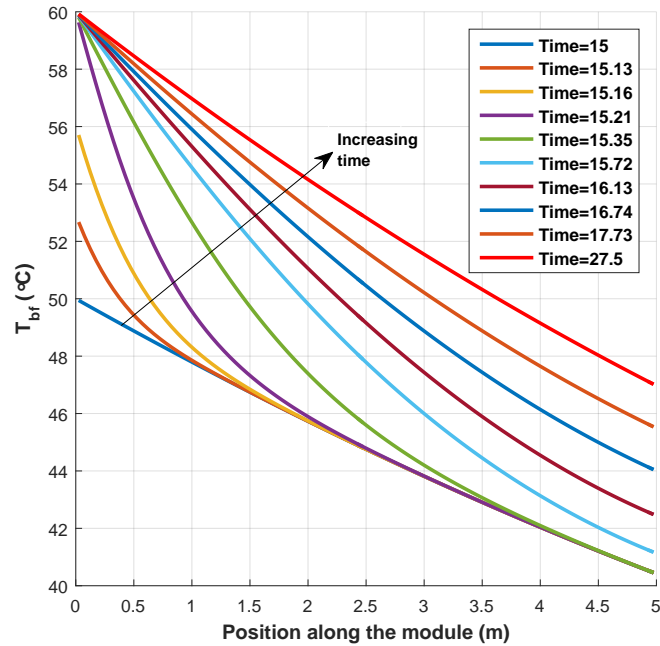
Figure 4.8: The time response of the bulk feed temperature distribution for a step change of the feed inlet temperature from 50°C to 60°C, where each curve shows the response at a given time instant.

given sufficient actuation power. The flux response is presented in Fig. 4.10, it also takes about 12 seconds to reach the new steady-state value.
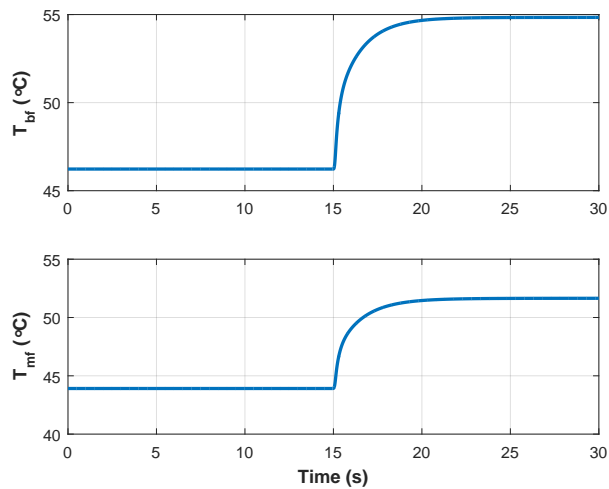
Figure 4.9: The time response for a step change in the feed inlet temperature of the bulk feed (top) and membrane-feed (bottom) temperatures at the cell corresponding to 1.75 m from the feed inlet.
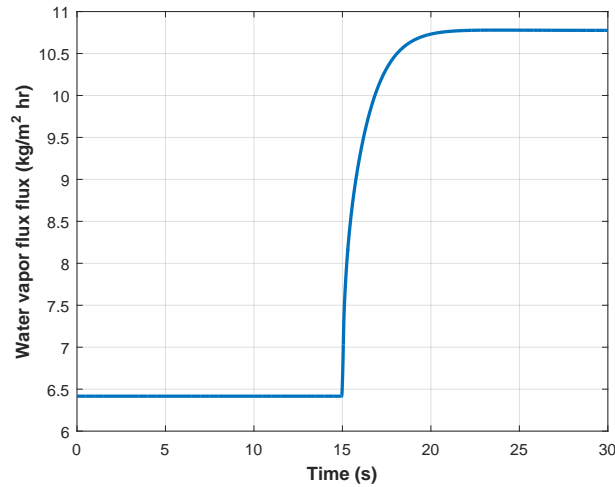
Figure 4.10: Water-vapor flux response for a step change in the feed inlet temperature.

4.5.2 Maximizing the DCMD process efficiency

We would like to apply the proposed model to investigate the DCMD process and optimize its efficiency. Specifically, we want to find the optimal inlet mass flow rates of the feed and permeate streams that maximize the process efficiency for any given module size. Define the thermal conversion efficiency as the ratio between the production rate in kg/hr and the supplied thermal energy calculated as $Q_{\text{in}} = M_{\text{f}_{\text{in}}} c_p T_{\text{f}_{\text{in}}}$. The water vapor flux and production rate (kg/hr) are simulated under different feed and permeate inlet velocities, 0.2, 0.4, 0.6, and 0.8 m/s, while the feed and permeate inlet temperatures were kept at 60°C and 20°C, respectively. The residence time (res_{time}) of the feed and permeate streams is increased by increasing the module length according to this relationship, res_{time} = inlet velocity/module length, while the module width is set to 0.4 m. In this simulation, we notice that as the length of the module increases the average flux decreases, as shown in Fig. 4.11. This is due to the following reasons:

1. As the residence time increases, more heat is lost by conduction through the membrane.
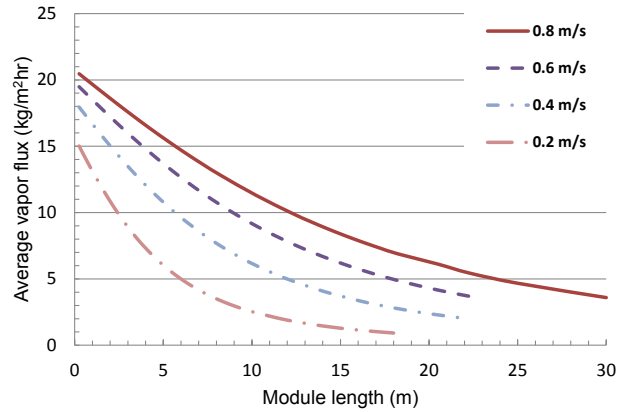
Figure 4.11: Predicted flux vs length for velocities 0.8, 0.6, 0.4, 0.2 m/s, top to bottom respectively

2. The relationship between the saturation vapor pressure and the temperature is nonlinear. The exponential relationship between the temperature and pressure is the key factor here. Here are two cases that demonstrate this point.

Case 1: the temperature at the feed membrane interface is 50°C and at the permeate membrane side is 40°C. Calculating the pressure difference across the membrane gives P_1=4970 Pa.

Case 2: the temperature at the feed membrane interface is 60°C and at the permeate membrane side is 50°C. Calculating the pressure difference across the membrane gives P_2=18847 Pa.

In both cases, the temperature difference across the membrane is 10°C, but the flux generated in case 2 is much higher due to higher driving force. As the DCMD module length increases, the temperature drop in the feed side from inlet to outlet increases. Whereas for the permeate side, as the length increases, the temperature rise from inlet to outlet increases. At some point, the pressure differential along the module length decreases, which results in lower average flux.
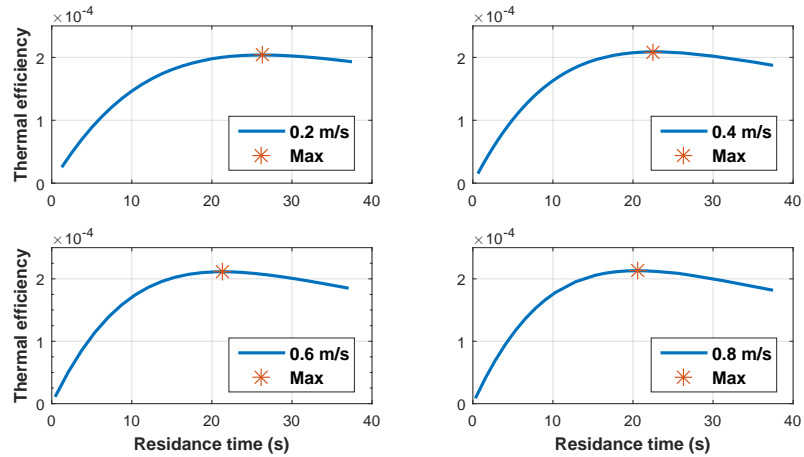
Figure 4.12: Thermal conversion efficiency (kg/hr W) for velocities 0.2, 0.4, 0.6, 0.8 m/s. Maximum efficiency is marked with a star for each plot.
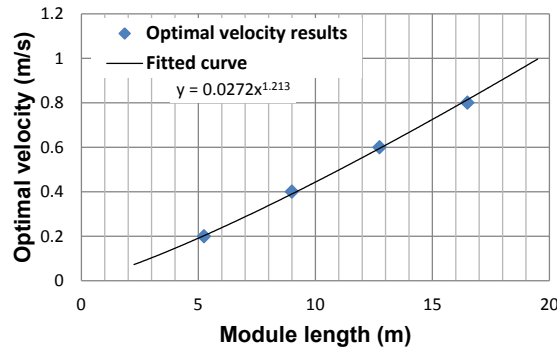
Figure 4.13: Optimal residence time vs optimal length. Notice that if the module length increases, then the feed and permeate inlet velocities should be high as well.

On the other hand, the thermal conversion efficiency increases rapidly as the residence time increases until it reaches a maximum value after which it starts to gradually decline, as seen in Fig. 4.12. An important remark regarding the optimal residence time of water inside the DCMD module channels is observed. For small lengths, it is optimal to run at relatively slow velocities and vice versa, as shown in Fig.4.13. Therefore, there exist an optimal inlet velocity for each module length, which achieves maximum efficiency. Plotting the optimal velocity vs the module length, the following relation can be obtained by fitting the points to a curve, $v = 0.0272x^{1.213}$.
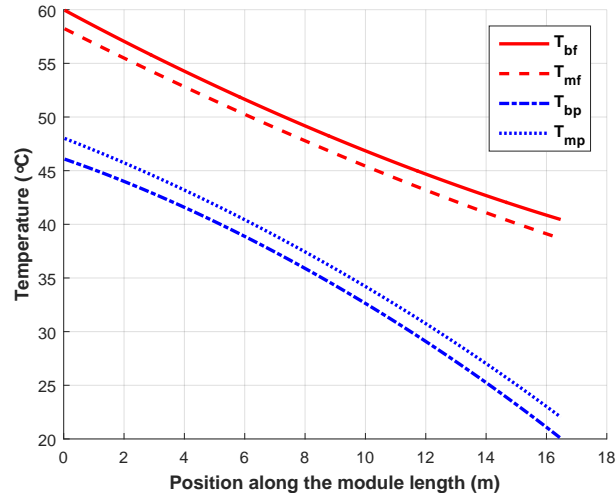
Figure 4.14: Predicted temperature distribution along the length of the module for both the feed and permeate sides.

4.5.3 Temperature prediction along the module length

Predicting the temperature at the membrane boundary layers is essential to accurately quantify the water vapor flux. This model provides distributed temperature predictions along the length of the module. Fig. 4.14 shows the feed and permeate bulk and boundary layers temperatures under the conditions: module length of 16.5 m, width of 0.4 m, feed and permeate inlet temperatures of 60°C and 20°C, respectively, and the linear velocities of both sides was 0.4 m/s. Since this is a counter-current flow setup, the bulk-feed and membrane-feed boundary temperatures drop with the flow direction, whereas the bulk permeate and boundary layer temperature increase with the flow direction. This figure clearly shows the nonlinear temperature distribution along the module length.

4.5.4 Effect of linear velocity on the TPC

To investigate the effect of feed and permeate inlet velocities on the TPC, we design the following simulation. The feed and permeate inlet temperatures are kept constant at 60°C and 20°C, respectively, while the inlet velocities were increased from 0.1 m/s
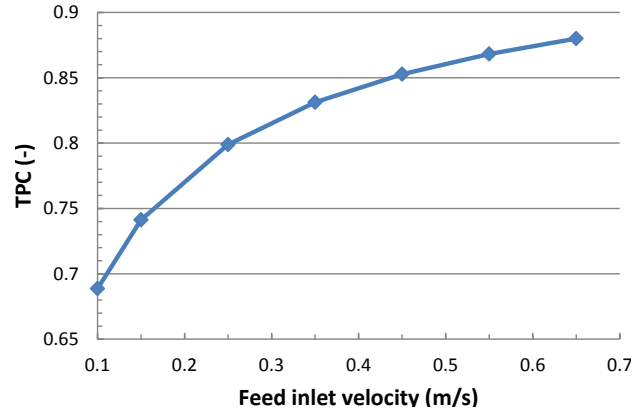
Figure 4.15: TPC as a function of feed inlet velocity.

to 0.65 m/s. Fig. 4.15 shows the TPC as a function of the inlet velocities. It is clear that increasing the inlet velocity has a desirable effect on the TPC. However, this effect begins to saturate starting from 0.5 m/s onward. As the velocity inside the feed and permeate channels increases, the Reynolds number of the flow increases and, as a result, the thermal boundary layer thickness is reduced. Therefore the temperatures at the membrane interfaces are brought closer towards that of the respective bulk temperature.

4.5.5 Membrane Mass Transfer Coefficient Identification

It is very important to estimate the membrane mass transfer coefficient to study the efficiency of the module design and monitor the condition of the membrane during operation. A simple test was designed to identify the membrane mass transfer coefficient in each cell which demonstrates the potential application of this model. Again 10 cells were used for this test, but now two cells had a membrane mass transfer coefficient of 4.1919e-07 (Kg/m^2 hr Pa) and the remaining eight cells had a mass transfer coefficient of 6.6919e-07 (Kg/m^2 hr Pa). Ten experiments were simulated with increasing linear velocities of the feed and permeate streams from 0.115 m/s to 0.55 m/s with feed inlet temperature of 60°C and permeate inlet temperature of 20°C and the total flux was recorded for each experiment. The total flux of the module

can be expressed as the sum of the individual cells fluxes:

$$J = \sum_{n=1}^{10} B_{m_n} \Delta P_n. \tag{4.1}$$

A linear system of equations was set to identify the individual cell membrane mass transfer coefficients, in which the partial vapor pressure difference across the membrane in each cell was calculated from the temperature distribution along the flow direction. Then, by solving the system of equations for B_{m_n} using the truncated singular value decomposition method, the mass transfer coefficient of each cell was successfully identified and in the correct order.

4.6   Chapter Summary

This chapter presented the experimental validation results of the proposed model under steady-state and dynamic operating conditions. The simulation results were found to be accurate and within measurement tolerance. Encouraged by these results, we discussed the effects of various operational parameters on the DCMD process performance. It was found that the proposed model could be used to estimate the membrane mass transfer coefficient. However, a more efficient way to evaluate the characteristics and conditions of the membrane is by designing adaptive observers, which could run in real-time and take advantage of readily available measurements (feed and permeate outlet temperatures and flux). This will enable real-time fault detection of the membrane fouling. In the next chapter, we present a novel design method of adaptive observers for a class of nonlinear descriptor systems, which will be later extended and applied for the membrane fouling detection in Chapter 7.

Part II

Adaptive Observers Design and Fouling Detection

Chapter 5

Adaptive Observer Design for Descriptor Systems

5.1 Introduction

This chapter reviews the relevant literature about adaptive observers design for descriptor systems. Then, a novel design method of adaptive observers for nonlinear descriptor systems is presented with proof of convergence. Finally, a numerical example illustrates the performance of the proposed adaptive observer.

5.2 Related Work

Adaptive observers are used for joint state and parameter estimation. Among the main motivations to study and design adaptive observers are adaptive control and fault detection and isolation (FDI) [32, 33, 34]. Over the past decades, the design of linear and adaptive observers has been extensively studied in [35, 36, 37, 38] and references therein. On the other hand, design methods for nonlinear systems are still an active research field. In [39], a unifying form for adaptive observers for systems that are linear in their parameters was presented. More recently, an adaptive observer for a class of systems that are nonlinear in the parameters was introduced in [40]. These methods deal with systems modeled by ordinary differential equations (ODE).

A more general class of models are descriptor systems (also known as differential algebraic systems or singular systems). These systems appear naturally when modeling interconnected processes, electrical networks, and constrained mechanical systems [23, 41, 42]. There are two common approaches to design observers for descriptor sys-

tems. The common approach to observer design for linear descriptor systems is to use a system of ODEs such that its solution converges asymptotically to the true states by eigenvalue assignment [43, 44]. This approach was extended to estimate states and unknown inputs for linear systems with applications to fault estimation [45, 46] and FDI for linear parameter varying systems [47]. Conversely, for nonlinear descriptor systems, the observer dynamics are a copy of the original system with an error correction term. This approach may also be applied to linear descriptor systems. In this approach, under Lipschitz conditions for the nonlinear terms, one can derive the observer gain based on Lyapunov analysis by solving a set of linear matrix inequalities (LMI) [48, 49, 50, 51].

The early work by [52] presented a design method for adaptive observer for linear descriptor systems. Later in [53], an adaptive observer for linear descriptor system based on the method reported in [43] was proposed. To the best of the authors' knowledge, adaptive descriptor observers for nonlinear systems has not been studied.

This chapter presents an adaptive descriptor observers design method for a class of nonlinear descriptor systems with Lipschitz nonlinearities and unknown parameters. Unlike the methods reported in [43, 44, 45, 53], the proposed method does not require coordinate transformation. In addition, the adaptive observer gain design is facilitated by solving a set of LMI, which guarantees sufficient conditions for asymptotic convergence of the states and parameters estimations to their true values.

This chapter is organized as follows. In Section 5.3, the problem formulation and the proposed adaptive observer design with the convergence proof are presented. The convergence results are established for noise-corrupted systems in Section 5.4. The performance of the proposed adaptive observer is illustrated with a numerical example in Section 5.5. This chapter is concluded in Section 5.6. Appendix B recalls some preliminary results and lemmas.

5.3 Adaptive Observer Design for Descriptor Systems

5.3.1 Definitions

The following definitions are used for descriptor systems stability and observability, which are founded in [54].

Definition 5.1: If $\det(sE - A) \neq 0, \ s \in \mathbb{C}$, then the pair (E,A) is said to be regular. A regular pair (E,A) is impulse-free if $\deg \det(sE - A) = \text{rank}(E)$. If all the roots of the polynomial $\det(sE - A) = 0, \ s \in \mathbb{C}$ have negative real parts, then the pair (E,A) is stable. If the pair (E,A) is regular, impulse-free, and stable, then it is said to be admissible.

Lemma 5.1: [55] The pair (E,A) is admissible if and only if there exists a matrix $X \in \mathbb{R}^{n \times n}$ that satisfies the following

$$
\begin{aligned}
E^T X = X^T E &\geqslant 0, \\
A^T X + X^T A &< 0.
\end{aligned}
\tag{5.1}
$$

Definition 5.2: System (5.4) is called R-detectable if and only if its slow subsystem (differential equations) is detectable, i.e.

$$
\text{rank} \begin{bmatrix} s\,E - A \\ C \end{bmatrix} = n, \quad \forall s \in \mathbb{C}, \ s \text{ finite.}
\tag{5.2}
$$

Definition 5.3: System (5.4) is called impulse-observable if and only if its fast subsystem (algebraic equations) is impulse-observable, i.e.

$$
\text{rank} \begin{bmatrix} E & A \\ 0 & E \\ 0 & C \end{bmatrix} = n + \text{rank } E.
\tag{5.3}
$$

5.3.2 Observer Design

Consider the following descriptor system

$$E\dot{x} = Ax + Bu + D\gamma(t,x)\theta + \psi(t,y,u),$$
$$y = Cx, \tag{5.4}$$

where $x \in \mathbb{R}^n$ is the system state, $u \in \mathbb{R}^m$ is the system input assumed known, $y \in \mathbb{R}^r$ is the system output, $\theta \in \mathbb{R}^{n_\theta}$ is a vector of unknown time invariant parameters. The matrices $E, A \in \mathbb{R}^{n \times n}$, $B \in \mathbb{R}^{n \times m}$, $D \in \mathbb{R}^{n \times q}$, $C \in \mathbb{R}^{r \times n}$ are constants and rank$(E) = s < n$. The known nonlinear functions $\gamma(t,x) \in \mathbb{R}^{q \times n_\theta}$ and $\psi(t,y,u) \in \mathbb{R}^n$ are locally Lipschitz.

Throughout this chapter, we assume the following:

Assumption 5.1: System (5.4) is R-detectable and impulse-observable.

Assumption 5.2: For $\alpha_1 > 0$, the function $\gamma(t,x)$ satisfies

$$\| \gamma(t,x_1) - \gamma(t,x_2) \| \leqslant \alpha_1 \| x_1 - x_2 \| . \tag{5.5}$$

Assumption 5.3: The parameter vector θ is piecewise constant and bounded

$$\| \theta \| \leqslant \alpha_2, \qquad\qquad \alpha_2 > 0. \tag{5.6}$$

The full-order adaptive observer for system (5.4) is of the form

$$E\dot{\hat{x}} = A\hat{x} + Bu + D\gamma(t,\hat{x})\hat{\theta} + \psi(t,y,u) + K(y - \hat{y}),$$
$$\hat{y} = C\hat{x}, \tag{5.7}$$

where $\hat{x} \in \mathbb{R}^n$ and $\hat{\theta} \in \mathbb{R}^{n_\theta}$ are the state and parameter estimates, respectively, and $K \in \mathbb{R}^{n \times r}$ is the observer gain to be designed.

Define the state estimation error by $e_1 = x - \hat{x}$, then from (5.4) and (5.7), the observer error dynamics are given by

$$E\dot{e}_1 = (A - KC)e_1 + D\Big(\gamma(t, x)\theta - \gamma(t, \hat{x})\hat{\theta}\Big). \tag{5.8}$$

The following theorem gives sufficient conditions for convergence of the adaptive observer error dynamics.

Theorem 5.1: Consider the following parameter estimation adaptation law

$$\dot{\hat{\theta}} = \Sigma^{-1}\gamma^T(t, \hat{x})\eta C(x - \hat{x}), \tag{5.9}$$

where $\Sigma^{-1} = \Sigma^{-T} > 0$ is an arbitrary constant matrix of appropriate dimension, which can be thought off as the adaptation rate, and $\eta \in \mathbb{R}^{q \times r}$ such that $D^T P = \eta C$.

Then, system (5.7) is an asymptotically stable adaptive observer for system (5.4), if there exists a non-singular matrix $P \in \mathbb{R}^{n \times n}$, a matrix $W \in \mathbb{R}^{r \times n}$ such that $K = (WP^{-1})^T$, and a scalar $\epsilon_1 > 0$ for which the following matrix inequalities are solvable

$$E^T P = P^T E \geq 0, \tag{5.10}$$

$$\begin{bmatrix} \Omega & P^T \\ P & -\epsilon_1 I \end{bmatrix} < 0, \tag{5.11}$$

where $\Omega = A^T P + P^T A - C^T W - W^T C + \epsilon_1 \alpha_1^2 \alpha_2^2 \parallel D \parallel^2 I$.

Moreover, if the persistent excitation condition holds $\forall t_0, \exists \xi, \delta > 0$ such that

$$\int_{t_0}^{t_0 + \delta} D\gamma(\tau, x)\gamma(\tau, x)^T D^T d\tau > \xi I, \tag{5.12}$$

then, the parameter estimation error converges asymptotically to zero, i.e $\hat{\theta} \to \theta$ as $t \to \infty$.

Proof. If we show that system (5.8) is asymptotically stable, then, it follows that system (5.7) is a full-order adaptive observer for system (5.4). Let $\bar{A} = (A - KC)$ and define the Lyapunov candidate function for error dynamics as

$$V(t) = e_1^T E^T P e_1 + e_2^T \Sigma e_2, \tag{5.13}$$

where $e_2 = \theta - \hat{\theta}$ is the parameter estimation error. The derivative of $V(t)$ is given as

$$\begin{aligned}
\dot{V}(t) =& (E\dot{e}_1)^T P e_1 + e_1^T P^T E \dot{e}_1 + 2 e_2^T \Sigma \dot{e}_2, \tag{5.14}\\
=& \left[\bar{A} e_1 + D\gamma(t, x)\theta - D\gamma(t, \hat{x})\hat{\theta} \right]^T P e_1 \\
& + e_1^T P^T \left[\bar{A} e_1 + D\gamma(t, x)\theta - D\gamma(t, \hat{x})\hat{\theta} \right] + 2 e_2^T \Sigma \dot{e}_2, \\
=& e_1^T \left[\bar{A}^T P + P^T \bar{A} \right] e_1 + 2 \left[D\gamma(t, x)\theta - D\gamma(t, \hat{x})\hat{\theta} \right]^T P e_1 + 2 e_2^T \Sigma \dot{e}_2.
\end{aligned}$$

Substituting $\hat{\theta} = \theta - e_2$ on the second term

$$\begin{aligned}
\dot{V}(t) =& e_1^T \left[\bar{A}^T P + P^T \bar{A} \right] e_1 + 2 \left[D\gamma(t, x)\theta - D\gamma(t, \hat{x})\theta \right]^T P e_1 \\
& + 2 \left[D\gamma(t, \hat{x})e_2 \right]^T P e_1 + 2 e_2^T \Sigma \dot{e}_2.
\end{aligned} \tag{5.15}$$

Applying LemmaB.1 on the second term

$$\begin{aligned}
\dot{V}(t) \leqslant& e_1^T \left[\bar{A}^T P + P^T \bar{A} \right] e_1 + \epsilon_1 \| D\left(\gamma(t, x) - \gamma(t, \hat{x})\right)\theta \|^2 \\
& + \epsilon_1^{-1} e_1^T P^T P e_1 + 2 \left[D\gamma(t, \hat{x})e_2 \right]^T P e_1 + 2 e_2^T \Sigma \dot{e}_2. \tag{5.16}
\end{aligned}$$

Using (5.5) on the second term

$$\dot{V}(t) \leqslant e_1^T \left[\Omega + \epsilon_1^{-1} P^T P \right] e_1 + 2 \left[D\gamma(t, \hat{x})e_2 \right]^T P e_1 + 2 e_2^T \Sigma \dot{e}_2, \tag{5.17}$$

where $\Omega = \bar{A}^T P + P^T \bar{A} + \epsilon_1 \alpha_1^2 \alpha_2^2 \| D \|^2 I$.

Since θ is piecewise constant, $\dot{\theta} = 0$, thus $\dot{e}_2 = -\dot{\hat{\theta}}$. Using the condition $D^T P = \eta C$

we obtain $2\left[D\gamma(t,\hat{x})e_2\right]^T Pe_1 + 2e_2^T \Sigma \dot{e}_2 = 0$, and the parameter adaptation law is given by

$$\dot{\hat{\theta}} = \Sigma^{-1}\gamma^T(t,\hat{x})\eta Ce_1. \tag{5.18}$$

Then, inequality (5.17) becomes,

$$\dot{V}(t) \leqslant e_1^T \left[\Omega + \epsilon_1^{-1}P^T P\right] e_1. \tag{5.19}$$

Therefore, a sufficient condition for $\dot{V}(t) < 0$ is

$$\Omega + \epsilon_1^{-1}P^T P < 0. \tag{5.20}$$

The above inequality can be converted to an LMI, using Schur complement, as

$$\begin{bmatrix} \Omega & P^T \\ P & -\epsilon_1 I \end{bmatrix} < 0. \tag{5.21}$$

For some $\beta > 0$ and from inequality (5.20), it follows that

$$\Omega + \epsilon_1^{-1}P^T P < -\beta I. \tag{5.22}$$

Substituting (5.22) into (5.19), we have

$$\dot{V}(t) \leqslant -\beta e_1^T e_1, \tag{5.23}$$

which implies that $V(t)$ is bounded, since $V(t) \geq 0$ and (5.23) shows that $V(t)$ is non-increasing. It follows from (5.13) that e_1 and e_2 are also bounded. integrating both sides of (5.23) from $t = 0$ to $t = t_1$ yields

$$V(t_1) \leqslant V(0) - \beta \int_0^{t_1} e_1^T(\tau)e_1(\tau)d\tau. \tag{5.24}$$

We obtain that $e_1 \in L^2$ from (5.24). In addition, the observer error dynamics (5.8) implies that $\dot{e}_1 \in L^\infty$. Based on this and using the Barbalat's lemma [56], it follows that $\lim_{t \to \infty} e_1 = 0$ and, as a result, $\lim_{t \to \infty} \dot{e}_1 = 0$. Therefore, from (5.8)

$$\lim_{t \to \infty} D\left(\gamma(t, x)\theta - \gamma(t, \hat{x})\hat{\theta} \right) = 0. \tag{5.25}$$

As $\lim_{t \to \infty} \hat{x} = x$, then $\gamma(t, \hat{x}) \to \gamma(t, x)$ since $\gamma(t, x)$ is continuous and as a result (5.25) is reduced to

$$\lim_{t \to \infty} D\left(\gamma(t, x)(\theta - \hat{\theta}) \right) = 0. \tag{5.26}$$

Moreover, the parameter estimation error converges to zero, i.e. $\hat{\theta} \to \theta$ if the persistent excitation condition (5.12) holds, which is a typical requirement in system identification [38]. $\qquad \square$

5.4 Robustness to Noise, Convergence in the Mean

Consider the noise corrupted descriptor system

$$E\dot{x} = Ax + Bu + D\gamma(t, x)\theta + \psi(t, y, u) + w(t)$$

$$y = Cx + \nu(t) \tag{5.27}$$

where $w(t) \in \mathbb{R}^n$ is the system noise, $\nu(t) \in \mathbb{R}^r$ is measurement noise.

Theorem 5.2: If the noises in system (5.27) $w(t)$ and $\nu(t)$ are bounded, then the state and parameter estimation errors, $e_1(t)$ and $e_2(t)$ respectively, of the adaptive descriptor observer (5.7) for system (5.27) are also bounded.

In addition, if the noises $w(t)$ and $\nu(t)$ have zero mean for all t and are independent of $\gamma(t, x)$, then as $t \to \infty$, the mean of the state and parameter estimation error $\mathbb{E}[e_1(t)]$ and $\mathbb{E}[e_2(t)]$ converge asymptotically to zero.

Proof. In this case, the observer error dynamics are given by

$$Ee\dot{}_1 = (A - KC)e_1 + D\Big(\gamma(t, x)\theta - \gamma(t, \hat{x})\hat{\theta}\Big) + w(t) - K\nu(t), \tag{5.28}$$

$$\dot{e}_2 = -\Sigma^{-1}\gamma^T(t, \hat{x})\eta Ce_1 - \Sigma^{-1}\gamma^T(t, \hat{x})\eta\nu(t). \tag{5.29}$$

The homogeneous part of (5.28) is exponentially stable, thus the state estimation error $e_1(t)$ is bounded for $\gamma(t, x)$ satisfying the local Lipschtiz condition (5.5) and bounded noises $w(t)$ and $\nu(t)$. In the proof of Theorem 5.1, we concluded the asymptotic convergence of parameter estimation error $e_2(t)$ to zero in the noise free case. Therefore, for bounded noises the $e_2(t)$ is also bounded.

In addition, if we use the assumption that the noises $w(t)$ and $\nu(t)$ have zero mean for all time and are independent of $\gamma(t, x)$, then we can take the expected value ($\mathbb{E}$) of the error dynamics for the noise corrupted case (5.28) and (5.29) as

$$E\frac{d(\mathbb{E}[e_1])}{dt} = (A - KC)\mathbb{E}[e_1] + D\Big(\gamma(t, x)\theta - \gamma(t, \hat{x})\mathbb{E}[\hat{\theta}]\Big), \tag{5.30}$$

$$\frac{d(\mathbb{E}[e_2])}{dt} = -\Sigma^{-1}\gamma^T(t, \hat{x})\eta C\mathbb{E}[e_1], \tag{5.31}$$

where the order of differentiation and expectation operations have been interchanged. Notice that the dynamics of E $\mathbb{E}[e_1]$ and $\mathbb{E}[e_2]$, (5.30) and (5.31) respectively, are similar to the noise free case. Therefore, the state and parameter estimation errors converge to zero asymptotically in the mean sense. □

5.5 Illustrative Example

We demonstrate the proposed observer design through the following example. Consider system (5.4) with

$$E = \begin{bmatrix} 0 & 1 & 0 & 0 \\ 0 & 0 & 1 & 0 \\ 0 & 0 & 0 & 1 \\ 0 & 0 & 0 & 0 \end{bmatrix}, \quad A = \begin{bmatrix} 0 & -4 & 0 & 3 \\ 1 & 2 & -4 & 0 \\ 0 & 2 & 0 & -5 \\ -2 & 0 & 3 & 0 \end{bmatrix}, \quad B = \begin{bmatrix} -1 & 0 \\ 0 & 0 \\ 0 & 0 \\ 0 & 1 \end{bmatrix}, \quad D = \begin{bmatrix} -1 & 0 \\ -1 & 0 \\ 0 & 0 \\ 0 & 1 \end{bmatrix},$$

$$C = \begin{bmatrix} 1 & 0 & 0 & 0 \\ 0 & 1 & 0 & 0 \end{bmatrix}, \quad \gamma = \begin{bmatrix} \sin^2(0.125t) & x_1^2 + \sqrt[3]{x_4} \\ x_3^3 + x_2 & \cos^2(0.125t) \end{bmatrix}.$$

Setting the design parameters $\alpha_1 = 1$ and $\alpha_2 = 4$ and using YALMIP toolbox [57] to solve the LMI sufficient conditions (5.10)-(5.11), we obtain the following results:

$$K = \begin{bmatrix} -8.808 & 6.250 \\ 1.782 & 2.788 \\ 1.267 & 1.650 \\ 7.648 & 0 \end{bmatrix}, \eta = \begin{bmatrix} 0 & -0.05937 \\ 0.05791 & 0.05845 \end{bmatrix}.$$

The initial states of the system and the adaptive observer are respectively $x(0) = \begin{bmatrix} -1.6624 & 0.8 & 2.8 & 0.2 \end{bmatrix}^T$,

$\hat{x}(0) = \begin{bmatrix} -1.5017 & 1.0 & 2.25 & 0.5 \end{bmatrix}^T$,

$\hat{\theta}(0) = \begin{bmatrix} 0.4 & -3.5 \end{bmatrix}^T$.

The adaptation rate was chosen as $\Sigma^{-1} = \text{diag}([50, 30])$.

For this simulation, the true values of the parameters θ_1 and θ_2 switch from 0.1 to 0.3 and from -4 to -2, respectively, at $t = 40$ and back again at $t = 80$.

The state and parameters estimation results for the noise-free systems are shown
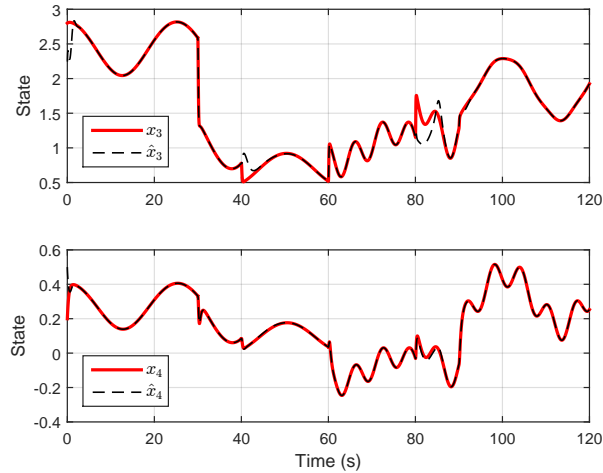
Figure 5.1: Observer response showing the two immeasurable states for the noise free system, top x_3, bottom x_4.
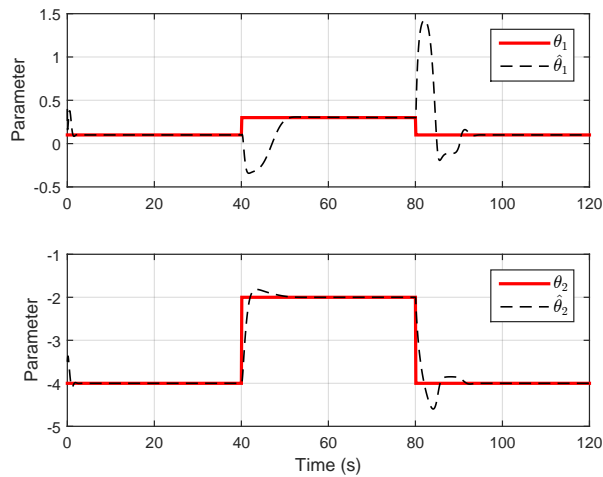
Figure 5.2: The estimates of the unknown parameters, top θ_1, bottom θ_2.

in Fig. 5.1 and 5.2, respectively.

In addition, Gaussian noise with standard deviation of 0.05 is added to the outputs of the system $y(t)$. The response of the system unknown states and their estimates is shown in Fig. 5.3. The estimates of two unknown parameters are depicted in Fig. 5.4.

It can be observed that the estimates of the states and parameters are robust to abrupt changes to the system input signals. The estimate of the parameters re-converges to the new value in about 10 s. After each parameter change, the state
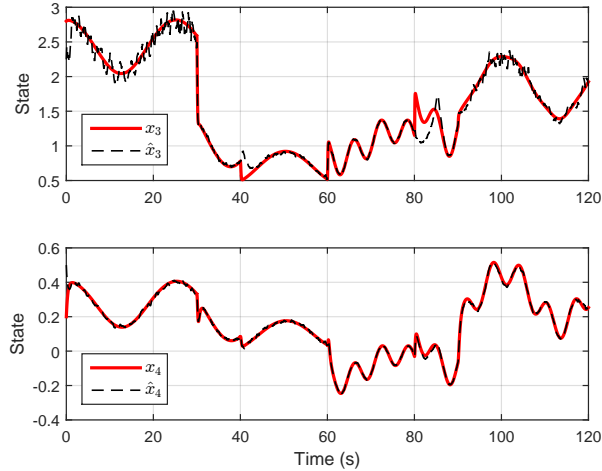
Figure 5.3: Observer response showing the two immeasurable states for the noise corrupted system, top x_3, bottom x_4.
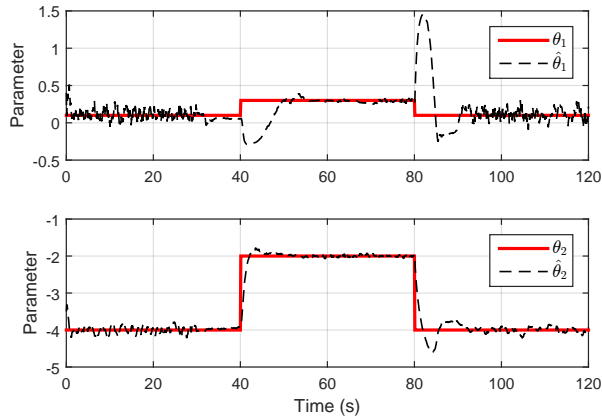
Figure 5.4: The estimates of the unknown parameters, top θ_1, bottom θ_2.

estimation error $e_1(t)$ converges to zero, in the mean sense, faster than the parameter error $e_2(t)$, as shown in Fig. 5.5.

5.6 Conclusion

This chapter proposed the first design method for descriptor adaptive observer for nonlinear systems. The convergence of the adaptive observer is obtained by solving a set of sufficient linear matrix inequalities. Robustness under the noise corrupted system and measurements has been established. For zero mean noises, the estimation errors of states and parameters converge, in the mean, to zero. The performance of
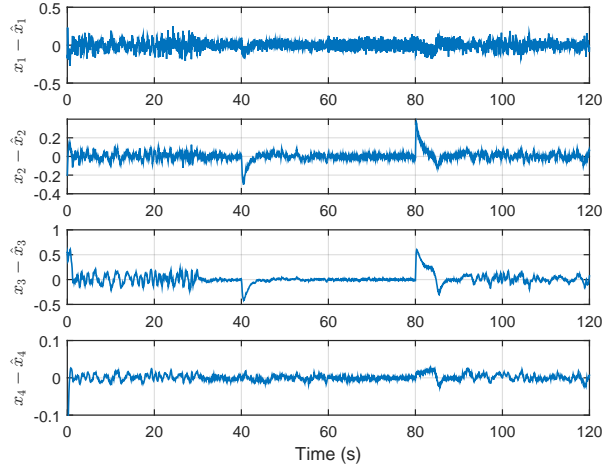
Figure 5.5: The state estimation error for the noise corrupted case.

proposed method has been demonstrated by a numerical example. This method can be used to systematically design adaptive observers for systems with a large number of states, which can be useful for fault detection and adaptive control applications. In the next chapter, we extend this design method and implement it for membrane fouling detection.

Chapter 6

Membrane Fouling Detection in DCMD

6.1 Introduction

Like many membrane-based desalination processes, MD is prone to membrane fouling and scaling, which is a process of accumulated deposition of clay, salt, organic and/or biological materials onto the membrane surface or into the membrane pores [58]. In this chapter, we review the current membrane fouling detection methods. Then, we extend the proposed electrical equivalent thermal network to model membrane fouling as well as the adaptive observer design method for the specific case of membrane fouling detection in DCMD.

6.2 Related Work

Membrane fouling affects the water quality and reduces the production rate and may even cause system shutdown for cleaning, which in turn, increases the operational cost of the MD system. In MD the fouling layer deposited on the surface of the membrane introduces a thermal resistance to heat transfer between the bulk feed stream and the membrane surface, see Fig. 6.1. This results in a lower temperature at the feed-membrane interface and hence a lower partial vapor pressure, which ultimately reduces the production rate of the system.

Several methods have been proposed for detecting membrane fouling in various membrane-based processes. While incorporating sensors into the process is challenging and can be expensive [59, 60], using mathematical tools and readily available

measurements to detect fouling is ideal for this application[61, 62]. In [61], a statistical method was developed to indicate fouling in membrane bioreactors. Another approach is based on the design of system observers, where the estimated profiles are used to conclude about faults in the system, as in [62] where a polynomial fuzzy observer is used to detect fouling in heat exchangers.

In fact, observers have been widely applied for fault detection and isolation (FDI) [32, 33, 34]. While several studies have discussed the design of linear and adaptive observers in [35, 36, 37, 38] and references therein; design of nonlinear adaptive observers is still an active area of research. For systems modeled by ODE, the work in [39] presents the design method of adaptive observers for systems that are linear in their parameters, whereas the recent work in [40] deals with systems modeled that are nonlinear in the parameters.

The common method to design observers for linear descriptor systems is to use a system of ODE, which asymptotically converges to the true states by eigenvalue assignment [43, 44]. Later, this approach was extended for fault estimation for linear descriptor systems with unknown inputs [45, 46] and linear parameter varying systems [47]. On the other hand, for Lipschitz nonlinear descriptor systems several methods have been proposed, where a stabilizing gain for a Luenberger like observer is designed by solving a set of linear matrix inequalities (LMI) [48, 49, 50, 51]. Fewer studies discussed the design of adaptive observers for descriptor systems. The linear case has been studied in [52, 53]. To the best of the authors' knowledge, only recently a design method for nonlinear adaptive descriptor observers has been proposed by us in [63].

The descriptor model for direct contact membrane distillation (DCMD) proposed in 4 is extended to account for membrane fouling. Then, an adaptive observer is proposed for the detection of membrane fouling based on [63]. Unlike the methods reported in [43, 44, 45, 53], the proposed method does not require coordinate transformation. In addition, the adaptive observer gain design is facilitated by solving a
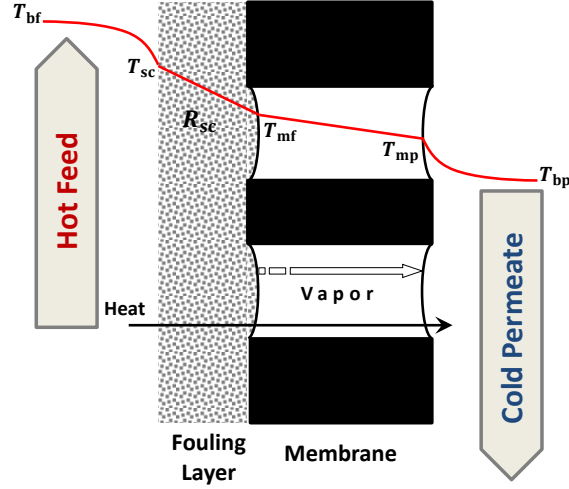
Figure 6.1: A schematic diagram of the fouling layer in DCMD setups.

set of LMI, which guarantees sufficient conditions for asymptotic convergence of the states and parameters estimations to their true values.

6.3   Membrane Fouling Modeling

6.3.1   DCMD fouling model

In MD the fouling layer deposited on the surface of the membrane introduces a thermal resistance to heat transfer between the bulk feed stream and the membrane surface, see Fig. 6.1. This results in a lower temperature at the feed-membrane interface and hence a lower partial vapor pressure, which ultimately reduces the production rate of the system.

The fouling thermal resistance (R_{sc}) can be incorporated into the previous model as shown in Fig. 6.2. Rewriting the heat transfer equations to account for the fouling resistance gives:

$$
\begin{aligned}
\frac{dT_{bf_n}}{dt} &= \frac{1}{C_{bf}}Q_{f_n} - \frac{1}{C_{bf}}Q_{f_{n+1}} - \frac{1}{C_{bf}}\left(\frac{1}{R_f} + J_n A_m c_p\right)T_{bf_n} \\
&+ \frac{1}{C_{bf}}\left(\frac{R_s c(1 + R_f\ G_n\ c_p)}{R_f + R_s c(1 + R_f\ G_n\ c_p)}\right)T_{bf_n} + \frac{1}{C_{bf}(R_f + R_s c(1 + R_f\ G_n\ c_p))}T_{mf_n},
\end{aligned}
\tag{6.1}
$$
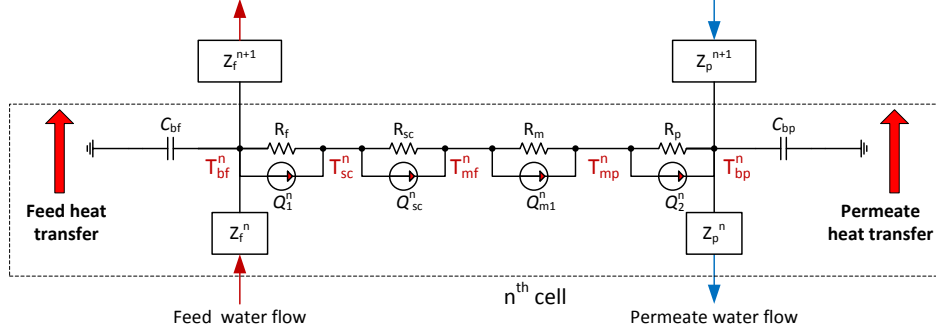
Figure 6.2: The electrical analogue of the nth cell with showing the thermal resistance of the membrane fouling layer.

$$
\left(\frac{1}{R_f} + J_n A_m c_p + \frac{R_{sc}(1 + R_f\ G_n\ c_p)}{R_f + R_{sc}(1 + R_f\ G_n\ c_p)} \right) T_{bf_n}
$$
$$
- \frac{1}{(R_f + R_{sc}(1 + R_f\ G_n\ c_p))} T_{mf_n} = \left(\frac{1}{R_p} + J_n A_m c_p \right) T_{mp_n} - \frac{1}{R_p} T_{bp_n}. \tag{6.2}
$$

Assuming that the feed and permeate inlet mass flow rates into the module are constant, i.e. not changing over time, then the proposed model can be represented as:

$$
E\dot{x} = Ax + Bu + D_1 \gamma(t, x) B_m + H(x, R_{sc}),
$$
$$
y = \begin{bmatrix} Cx \\ G \end{bmatrix}, \tag{6.3}
$$

where $x \in \mathbb{R}^{6N+4}$ is the system state vector, $A \in \mathbb{R}^{6N+4 \times 6N+4}$ is a constant state transition matrix, $B \in \mathbb{R}^{6N+4 \times 2}$, u is the system input which is the known feed and permeate inlet temperatures, $D_1 \in \mathbb{R}^{6N+4 \times 3N}$ is a constant matrix mapping the nonlinear terms to the state equations, $\gamma(t, x) \in \mathbb{R}^{3N \times 1}$ is the nonlinear part of the DCMD model related to the mass flux, $\theta \in \mathbb{R}^+$ is the known time invariant membrane mass transfer coefficient, $H(x, R_{sc}) \in \mathbb{R}^{6N+4 \times 1}$ is a nonlinear function of the state x and the fouling thermal resistance R_{sc}, and $y \in \mathbb{R}^{3 \times 1}$ is the system output. Note that this process has two kind of outputs, the first one is linear combination of the system states through the matrix $C \in \mathbb{R}^{2 \times 6N+4}$, in this case it is the feed and permeate

outlet temperatures. The second is the production rate of the DCMD module (G), which measured directly from the module. It can be seen that G is a nonlinear function of the temperatures at the membrane surfaces and the membrane mass transfer coefficient. The A, B, D, and $\gamma(t,x)$, matrices can be extracted from the DAE system representation explained in Section 3.5. Whereas $H(x, R_{sc})$, for a model with three cells, is given as

$$
H(x,\mathrm{R_{sc}}) =
\begin{bmatrix}
8M_{fin}^4 a_{2\mathrm{s}_1} T_{\mathrm{f_{in}}} - 4M_{\mathrm{fin}}^2 a_{1\mathrm{s}_1} Q_{\mathrm{f}_1} - 8M_{fin}^4 a_{2\mathrm{s}_1} T_{bf_1} \\[4pt]
\frac{\mathrm{R_{sc}}(1+\mathrm{R_f}\ G_1\ c_p)}{C_{\mathrm{bf}}\mathrm{R_f}(\mathrm{R_{sc}}(1+\mathrm{R_f}\ G_1\ c_p)+\mathrm{R_f})}T_{\mathrm{bf}_1} + \frac{1}{C_{\mathrm{bf}}(\mathrm{R_{sc}}(1+\mathrm{R_f}\ G_1\ c_p)+\mathrm{R_f})}T_{\mathrm{mf}_1} \\[4pt]
4M_1^4 a_{2\mathrm{s}_2} T_{\mathrm{bf}_1} - 4M_1^2 a_{1\mathrm{s}_2} Q_{\mathrm{f}_2} - 4M_1^4 a_{2\mathrm{s}_2} T_{bf_2} \\[4pt]
\frac{\mathrm{R_{sc}}(1+\mathrm{R_f}\ G_2\ c_p)}{C_{\mathrm{bf}}\mathrm{R_f}(\mathrm{R_{sc}}(1+\mathrm{R_f}\ G_2\ c_p)+\mathrm{R_f})}T_{\mathrm{bf}_2} + \frac{1}{C_{\mathrm{bf}}(\mathrm{R_{sc}}(1+\mathrm{R_f}\ G_2\ c_p)+\mathrm{R_f})}T_{\mathrm{mf}_2} \\[4pt]
4M_2^4 a_{2\mathrm{s}_3} T_{\mathrm{bf}_2} - 4M_2^2 a_{1\mathrm{s}_3} Q_{\mathrm{f}_3} - 4M_2^4 a_{2\mathrm{s}_3} T_{bf_3} \\[4pt]
\frac{\mathrm{R_{sc}}(1+\mathrm{R_f}\ G_3\ c_p)}{C_{\mathrm{bf}}\mathrm{R_f}(\mathrm{R_{sc}}(1+\mathrm{R_f}\ G_3\ c_p)+\mathrm{R_f})}T_{\mathrm{bf}_3} + \frac{1}{C_{\mathrm{bf}}(\mathrm{R_{sc}}(1+\mathrm{R_f}\ G_3\ c_p)+\mathrm{R_f})}T_{\mathrm{mf}_3} \\[4pt]
0 \\[4pt]
8M_{p_1}^4 a_{7\mathrm{s}_1} T_{\mathrm{P_{out}}} - 4M_{p_1}^2 a_{6\mathrm{s}_1} Q_{\mathrm{P}_1} - 8M_{p_1}^4 a_{7\mathrm{s}_1} T_{\mathrm{bp}_1} \\[4pt]
0 \\[4pt]
4M_{p_2}^4 a_{7\mathrm{s}_2} T_{\mathrm{bp}_1} - 4M_{p_2}^2 a_{6\mathrm{s}_2} Q_{\mathrm{P}_2} - 4M_{p_2}^4 a_{7\mathrm{s}_2} T_{\mathrm{bp}_2} \\[4pt]
0 \\[4pt]
4M_{p_3}^4 a_{7\mathrm{s}_3} T_{\mathrm{bp}_2} - 4M_{p_3}^2 a_{6\mathrm{s}_3} Q_{\mathrm{P}_3} - 4M_{p_3}^4 a_{7\mathrm{s}_3} T_{\mathrm{bp}_3} \\[4pt]
0 \\[4pt]
0 \\[4pt]
0 \\[4pt]
0 \\[4pt]
-\frac{\mathrm{R_{sc}}(1+\mathrm{R_f}\ G_1\ c_p)}{\mathrm{R_f}\ (\mathrm{R_{sc}}(1+\mathrm{R_f}\ G_1\ c_p)+\mathrm{R_f})}T_{\mathrm{bf}_1} - \frac{1}{\mathrm{R_{sc}}(1+\mathrm{R_f}\ G_1\ c_p)+\mathrm{R_f}}T_{\mathrm{mf}_1} \\[4pt]
-\frac{\mathrm{R_{sc}}(1+\mathrm{R_f}\ G_2\ c_p)}{\mathrm{R_f}\ (\mathrm{R_{sc}}(1+\mathrm{R_f}\ G_2\ c_p)+\mathrm{R_f})}T_{\mathrm{bf}_2} - \frac{1}{\mathrm{R_{sc}}(1+\mathrm{R_f}\ G_2\ c_p)+\mathrm{R_f}}T_{\mathrm{mf}_2} \\[4pt]
-\frac{\mathrm{R_{sc}}(1+\mathrm{R_f}\ G_3\ c_p)}{\mathrm{R_f}\ (\mathrm{R_{sc}}(1+\mathrm{R_f}\ G_3\ c_p)+\mathrm{R_f})}T_{\mathrm{bf}_3} - \frac{1}{\mathrm{R_{sc}}(1+\mathrm{R_f}\ G_3\ c_p)+\mathrm{R_f}}T_{\mathrm{mf}_3} \\[4pt]
0 \\[4pt]
0 \\[4pt]
0
\end{bmatrix}. \tag{6.4}
$$

6.4 Membrane fouling detection

Expanding the function $H(x, \mathrm{R_{sc}})$ around $\mathrm{R_{sc}} = 0$, this is the ideal case without membrane fouling. Taking the linear terms of the Taylor expansion, system (6.3) can be written as

$$E\dot{x} = Ax + Bu + D_1\gamma(t, x)B_m + D_2\tilde{H}(x)\Delta\mathrm{R_{sc}},$$
$$y = \begin{bmatrix} Cx \\ G \end{bmatrix}, \tag{6.5}$$

where $\tilde{H}(x)$ is the Jacobian of $H(x, \mathrm{R_{sc}})$, and $\Delta\mathrm{R_{sc}}$ is the deviation from the nominal value of zero fouling thermal resistance.

Consider the following adaptive observer form for system (6.5)

$$E\dot{\hat{x}} = A\hat{x} + Bu + D_1\gamma(t, \hat{x})B_m + D_2\tilde{H}(\hat{x})\Delta\hat{R}_{sc} + K(Cx - C\hat{x}),$$
$$\hat{y} = \begin{bmatrix} C\hat{x} \\ \hat{G} \end{bmatrix} \tag{6.6}$$

Define the state estimation error by $e_1 = x - \hat{x}$, then from (6.5) and (6.6), the observer error dynamics are given by

$$E\dot{e}_1 = (A - KC)e_1 + D_2\left(\tilde{H}(x)\Delta\mathrm{R_{sc}} - \tilde{H}(\hat{x})\Delta\hat{R}_{sc}\right). \tag{6.7}$$

The following theorem gives sufficient conditions for convergence of the adaptive observer error dynamics.

Theorem 6.1: Consider the following adaptation law

$$\Delta\dot{\hat{R}}_{sc} = \Sigma^{-1}\tilde{H}(\hat{x})\eta C(x - \hat{x}) - \Sigma^{-1}L(G - \hat{G}) \tag{6.8}$$

where $\Sigma^{-1} = \Sigma^{-T} > 0$ is an arbitrary constant matrix of appropriate dimension, which can be thought off as the adaptation rate.

Then, system (6.6) is an asymptotically stable adaptive observer for system (6.5), if there exists a non-singular matrix $P \in \mathbb{R}^{n \times n}$, a matrix $W \in \mathbb{R}^{r \times n}$ such that $K = (WP^{-1})^T$, and a scalar $\epsilon_1 > 0$ for which the following matrix inequalities are solvable

$$E^T P = P^T E \geq 0, \tag{6.9}$$

$$\begin{bmatrix} \Omega & P^T \\ P & -\epsilon_1 I \end{bmatrix} < 0, \tag{6.10}$$

where $\Omega = A^T P + P^T A - C^T W - W^T C + \epsilon_1 \alpha_1^2 \alpha_2^2 \parallel D_2 \parallel^2 I$, α_1 is the local Lipschitz constants of $\tilde{H}(x)$, and α_2 is the upper bound on the fouling thermal resistance ΔR_{sc}.

Moreover, if the persistent excitation condition holds $\forall t_0, \exists \xi, \delta > 0$ such that

$$\int_{t_0}^{t_0 + \delta} D_2 \tilde{H}(\hat{x}) \tilde{H}(\hat{x})^T D_2^T d\tau > \xi I, \tag{6.11}$$

then, the parameter estimation error converges to zero, i.e $\Delta \hat{R}_{sc} \to \Delta R_{sc}$ as $t \to \infty$.

Proof. If we show that system (6.7) is asymptotically stable, then, it follows that system (6.6) is a convergent adaptive observer for system (6.5). Let $\bar{A} = (A - KC)$ and define the Lyapunov candidate function for error dynamics as

$$V(t) = e_1^T E^T P e_1 + e_2^T \Sigma e_2, \tag{6.12}$$

where $e_2 = \Delta R_{sc} - \Delta \hat{R}_{sc}$ is the parameter estimation error. The derivative of $V(t)$ is

given as

$$\dot{V}(t) = (E\dot{e}_1)^T P e_1 + e_1^T P^T E \dot{e}_1 + 2 e_2^T \Sigma \dot{e}_2, \tag{6.13}$$

$$= \left[\bar{A} e_1 + D_2 \tilde{H}(x) \Delta \mathrm{R}_{\mathrm{sc}} - D_2 \tilde{H}(\hat{x}) \Delta \hat{R}_{sc} \right]^T P e_1$$

$$+ e_1^T P^T \left[\bar{A} e_1 + D_2 \tilde{H}(x) \Delta \mathrm{R}_{\mathrm{sc}} - D_2 \tilde{H}(\hat{x}) \Delta \hat{R}_{sc} \right] + 2 e_2^T \Sigma \dot{e}_2,$$

$$= e_1^T \left[\bar{A}^T P + P^T \bar{A} \right] e_1 + 2 \left[D_2 \tilde{H}(x) \Delta \mathrm{R}_{\mathrm{sc}} - D_2 \tilde{H}(\hat{x}) \Delta \hat{R}_{sc} \right]^T P e_1 + 2 e_2^T \Sigma \dot{e}_2.$$

Substituting $\Delta \hat{R}_{\mathrm{sc}} = \Delta \mathrm{R}_{\mathrm{sc}} - e_2$ on the second term

$$\dot{V}(t) = e_1^T \left[\bar{A}^T P + P^T \bar{A} \right] e_1 + 2 \left[D_2 \tilde{H}(x) \Delta \mathrm{R}_{\mathrm{sc}} - D_2 \tilde{H}(\hat{x}) \Delta \mathrm{R}_{\mathrm{sc}} \right]^T P e_1$$

$$+ 2 \left[D_2 \tilde{H}(\hat{x}) e_2 \right]^T P e_1 + 2 e_2^T \Sigma \dot{e}_2. \tag{6.14}$$

Applying Lemma B.1 on the second term

$$\dot{V}(t) \leqslant e_1^T \left[\bar{A}^T P + P^T \bar{A} \right] e_1$$

$$+ \epsilon_1 \parallel D_2 \big(\tilde{H}(x) - \tilde{H}(\hat{x}) \big) \Delta \mathrm{R}_{\mathrm{sc}} \parallel^2$$

$$+ \epsilon_1^{-1} e_1^T P^T P e_1$$

$$+ 2 \left[D_2 \tilde{H}(\hat{x}) e_2 \right]^T P e_1 + 2 e_2^T \Sigma \dot{e}_2. \tag{6.15}$$

Using the local Lipschitz property of $\tilde{H}(x)$ and the bound on $\Delta \mathrm{R}_{\mathrm{sc}}$ on the second term

$$\dot{V}(t) \leqslant e_1^T \left[\Omega + \epsilon_1^{-1} P^T P \right] e_1$$

$$+ 2 \left[D_2 \tilde{H}(\hat{x}) e_2 \right]^T P e_1 + 2 e_2^T \Sigma \dot{e}_2, \tag{6.16}$$

where

$$\Omega = \bar{A}^T P + P^T \bar{A} + \epsilon_1 \alpha_1^2 \alpha_2^2 \parallel D_2 \parallel^2 I. \tag{6.17}$$

Since ΔR_{sc} is piecewise constant, $\Delta \dot{R}_{sc} = 0$, thus $\dot{e}_2 = -\dot{\hat{R}}_{sc}$. Using the condition $D_2^T P = \eta C$ and substituting the adaptation law (6.8), we obtain

$$2 \left[D_2 \tilde{H}(\hat{x}) e_2 \right]^T P e_1 + 2 e_2^T \Sigma \dot{e}_2 = e_2^T L (G - \hat{G}), \tag{6.18}$$

where $L \in \mathbb{R}^+$ is a positive constant gain, then the term $-e_2^T L (G - \hat{G})$ is always non-positive as it can be shown

$$\begin{cases} \text{if } e_2 < 0, \rightarrow (G - \hat{G}) > 0, \text{therefore} e_2^T L (G - \hat{G}) < 0 \\ \text{if } e_2 > 0, \rightarrow (G - \hat{G}) < 0, \text{therefore} e_2^T L (G - \hat{G}) < 0 \end{cases} \tag{6.19}$$

Then, inequality (6.16) becomes,

$$\dot{V}(t) \leqslant e_1^T \left[\Omega + \epsilon_1^{-1} P^T P \right] e_1. \tag{6.20}$$

Therefore, a sufficient condition for $\dot{V}(t) < 0$ is

$$\Omega + \epsilon_1^{-1} P^T P < 0. \tag{6.21}$$

The above inequality can be converted to an LMI, using Schur complement, as

$$\begin{bmatrix} \Omega & P^T \\ P & -\epsilon_1 I \end{bmatrix} < 0. \tag{6.22}$$

For some $\beta > 0$ and from inequality (6.21), it follows that

$$\Omega + \epsilon_1^{-1} P^T P < -\beta I. \tag{6.23}$$

Substituting (6.23) into (6.20), we have

$$\dot{V}(t) \leqslant -\beta e_1^T e_1, \tag{6.24}$$

which implies that $V(t)$ is bounded, since $V(t) \geq 0$ and (6.24) shows that $V(t)$ is non-increasing. It follows from (6.12) that e_1 and e_2 are also bounded. integrating both sides of (6.24) from $t = 0$ to $t = t_1$ yields

$$V(t_1) \leqslant V(0) - \beta \int_0^{t_1} e_1^T(\tau)e_1(\tau)d\tau. \tag{6.25}$$

We obtain that $e_1 \in L^2$ from (6.25). In addition, the observer error dynamics (5.8) implies that $\dot{e}_1 \in L^\infty$. Based on this and using the Barbalat's lemma [56], it follows that $\lim_{t \to \infty} e_1 = 0$ and, as a result, $\lim_{t \to \infty} \dot{e}_1 = 0$. Therefore, from (6.7)

$$\lim_{t \to \infty} D_2\left(\tilde{H}(x)\Delta R_{sc} - \tilde{H}(\hat{x})\Delta \hat{R}_{sc}\right) = 0. \tag{6.26}$$

As $\lim_{t \to \infty} \hat{x} = x$, (6.26) is reduced to

$$\lim_{t \to \infty} D_2\left(\tilde{H}(x)(\Delta R_{sc} - \Delta \hat{R}_{sc})\right) = 0. \tag{6.27}$$

Moreover, the parameter estimation error converges to zero, i.e. $\Delta \hat{R}_{sc} \to \Delta R_{sc}$ if the persistent excitation condition (6.11) holds, which is a typical requirement in system identification [38]. $\square$

6.5 Numerical results

To demonstrate the performance of the proposed adaptive observer, a simulation of gradual membrane fouling is developed. For the first 25 seconds, the fouling thermal resistance (ΔR_{sc}) is set to zero. Then, a gradual increase takes place over the duration
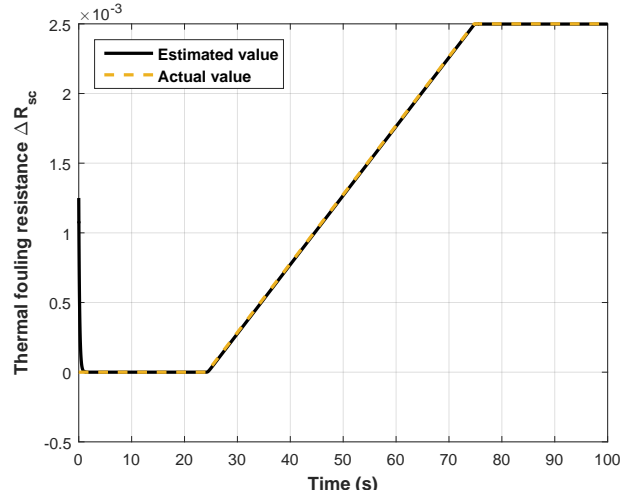
Figure 6.3: The estimated and actual profile of the thermal fouling resistance ($\Delta \mathrm{R_{sc}}$).
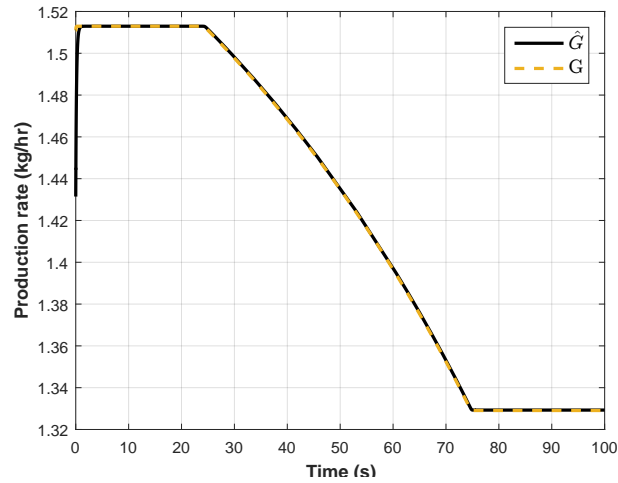
Figure 6.4: The estimated and actual profile of the modules production rate (G).

of 50 seconds, until the fouling thermal resistance reaches 2.5×10^{-3} and stays there for another 25 seconds. The actual and estimated profile of ΔR_{sc} is shown in Fig. 6.3. It is clear that the adaptive observer is able to track the development of the membrane fouling as it develops. The production rate over time is shown in Fig. 6.4, where the effect of membrane fouling is clear on the production rate. To confirm the response of the temperature distribution estimation, Fig. 6.5 shows the estimated and simulated temperature spatial profiles for both the feed and permeate sides of the module at the final time t=100s.
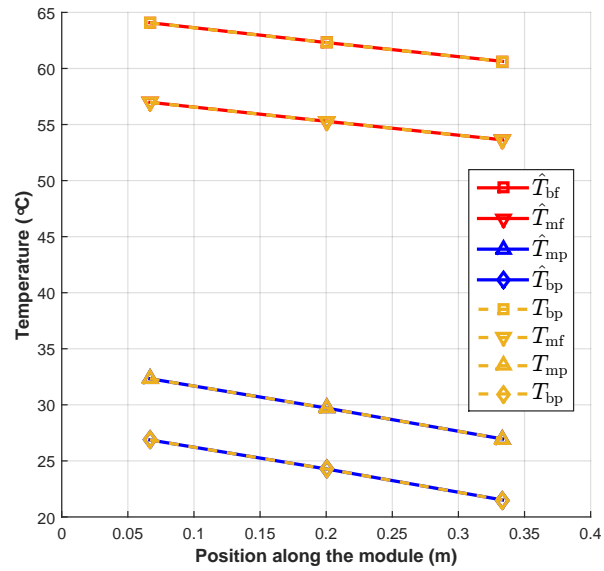
Figure 6.5: The temperature distribution through the DCMD module for both the estimated and actual values at time t=100s.

6.6   Conclusion

In this chapter, membrane fouling in DCMD has been modeled by an extension of the proposed electrical equivalent thermal network model. The proposed design method of adaptive observers has been implemented for the specific case of fouling detection in DCMD. Numerical simulation results were presented and discussed.

Part III

Optimization of Solar-Powered DCMD

Chapter 7

Extremum Seeking Control

7.1 Introduction

This chapter introduces the basic idea of Extremum Seeking (ES) control and explain two main configurations of ES, namely gradient-based ES and Newton-based ES. We then propose a modification to the Newton-based ES scheme. A numerical example illustrates the difference between the traditional ES and the proposed method.

7.2 Background

Many physical systems can be described by mathematical models, some of which are very complex or unreliable. Moreover, these systems might have an unknown optimal reference to output peak that depends on the system parameters or operating conditions. While classical adaptive control methods deal with the stabilization of systems and the tracking of a known set point, ES is an adaptive control method that finds and tracks an optimal peak of the reference to output map.

Extremum Seeking is non-model based which enables it to track the extremum (maximum or minimum) of the reference-to-output map as the system evolves. Therefor, ES is a real-time optimization technique contrary to numerical-based optimization methods which require the plant response to settle down before optimization.

Extremum Seeking control was very popular around the 1960s but advances in classical adaptive control theory and the emergence of digital computing slowly took over ES. However, since the proof of stability for ES was published for general non-

linear systems [64], it has received an increased attention and development in both theory and practice. Successful applications of extremum seeking control include axial-flow compressors [65], photovoltaics [66], optimizing bioreactors [67], and wind energy [68], as well as many other fields not listed here.

In the next two sections, two schemes of extremum seeking feedback controllers are presented.

7.3 Gradient Based Extremum Seeking

Consider a general nonlinear system given as

$$\dot{x} = f(x, u), \tag{7.1a}$$

$$y = h(x), \tag{7.1b}$$

where $x \in \mathbb{R}^n$ is the states, $u \in \mathbb{R}^m$ represents the inputs, $y \in \mathbb{R}$ is the output, and $f : \mathbb{R}^n \times \mathbb{R}^m \to \mathbb{R}^n$ and $h : \mathbb{R}^n \to \mathbb{R}$ are smooth functions. Now, suppose that a smooth control law is parameterized by a scalar value θ.

$$u(t) = \beta(x, \theta). \tag{7.2}$$

Then, the closed loop system is

$$\dot{x} = f\big(x, \beta(x, \theta)\big). \tag{7.3}$$

Finally, consider the following assumptions about the closed loop system 7.3.

Assumption 7.1: There exists a smooth function $l : \mathbb{R}^m \to \mathbb{R}^n$ such that $f\big(x, \beta(x, \theta)\big) = 0$ if and only if $x = l(\theta)$.

This means there exists an equilibrium point for the close loop system parameterized by θ. The following assumption lies in the heart of extremum seeking control.
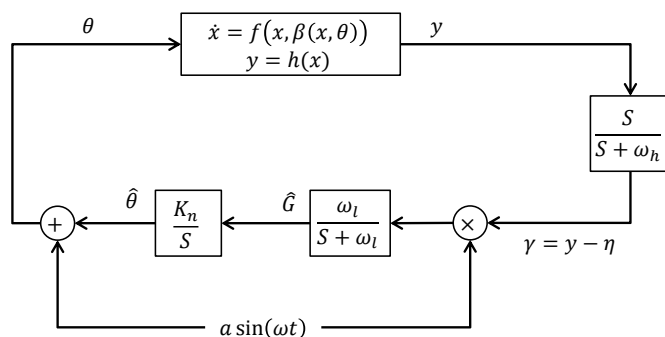
Figure 7.1: Block diagram of gradient-based ES scheme.

Assumption 7.2: There exists a θ^* such that

$$\frac{\partial y}{\partial \theta}\bigg|_{\theta=\theta^*} = 0$$

$$\frac{\partial^2 y}{\partial \theta^2}\bigg|_{\theta=\theta^*} = H \prec 0, \qquad\qquad H^T = H.$$

This simply says that the reference-to-output map $y = h(l(\theta))$ has a maximum at $\theta = \theta^*$. Without loss of generality, the following analysis still holds for the case of a minimum by replacing y with $-y$.

A feedback peak seeking scheme is depicted in Fig. 7.1 for a general nonlinear SISO system. The same analysis holds for a multiple-input case with appropriate vector dimensions. This configuration resembles the foundation on which other extensions build on. A "slow" periodic perturbation is added to the signal $\hat{\theta}$ (which is an approximate value of the optimal parameter θ^*). The resultant signal (θ) is then applied to the system as an input which produces a periodic response on the output y. The high pass filter $(\frac{s}{s+\omega_h})$ together with the multiplication by the dither signal $a\sin(\omega t)$ acts like a differentiator, eliminating the "DC component" of y and producing an approximate sinusoidal estimate of the gradient. The low-pass filter $(\frac{\omega_l}{s+\omega_l})$

extracts the "DC component" of the multiplication result, which approximately represent the gradient $(\hat{G})$ of the reference-to-output map with respect to θ. Finally, the integrator updates $\hat{\theta}$ driving it towards θ^*.

The design and choice of frequencies in this scheme should follow these general guidelines:

- The perturbation frequency ω should be smaller than the response time of the system 7.1, as such the plant appears like a static map $y = h\big(l(\theta)\big)$.

- The cut-off frequencies for the high and low pass filters, ω_h and ω_l respectively, should be lower than the perturbation frequency ω.

The following equations summaries the system in Fig. 7.1:

$$\dot{x} = f\big(x, \beta(\hat{\theta} + a\sin\omega t)\big), \tag{7.4}$$

$$\dot{\hat{\theta}} = K_n\hat{G}, \tag{7.5}$$

$$\dot{\hat{G}} = -\omega_l\hat{G} + \omega_l(y - \eta)a\sin\omega t, \tag{7.6}$$

$$\dot{\eta} = -\omega_h + \omega_h y. \tag{7.7}$$

The stability proof of the gradient-based extremum seeking follows from averaging and singular perturbation analysis [64, 69]. The analysis shows that the solution converges to an $O(a)$-neighborhood of the optimal θ^*, where δ is a small positive constant. However, since extremum seeking control is a non-model based optimization method, the convergence rate of gradient-based extremum seeking is dictated by the unknown Hessian of the reference-to-output map. This may reduce the efficiency of extremum seeking for plants with a wide range of behavior [70]. To address this limitation, the Newton-based extremum seeking scheme was developed.
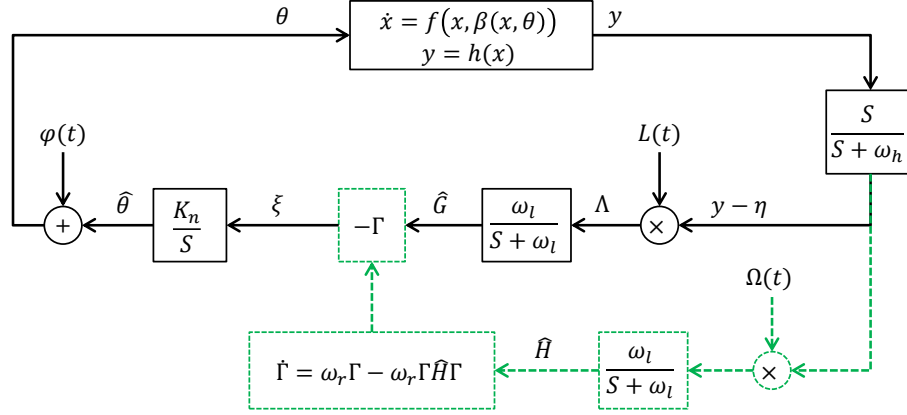
Figure 7.2: Block diagram of multivariable Newton-based ES.

7.4 Newton Based Extremum Seeking

Several configurations have been proposed for the Newton-based extremum seeking controller [70, 71, 72]. The work in [72] proposes a multivariate scheme for general non-linear systems and will be presented in this section.

Consider the same problem of finding an extremum of the general non-linear system reference-to-output map 7.1, with the control law defined as in 7.2. Then, the closed-loop system is given as

$$\dot{x} = f\big(x, \beta(x, \theta)\big). \tag{7.8}$$

Assumptions 7.1 and 7.2 are still applied here.

The block diagram of the Newton-based multivariate ES is depicted in Fig.7.2. This scheme builds on the structure of the gradient-based ES design and adds a mechanism to estimate the unknown Hessian. Since Newton's method requires the inverse of the Hessian, an estimate of the inverse of the Hessian is obtained asymptotically by the solution of a dynamic system in the form of a Riccati equation. By including the information about the gradient and the Hessian of the reference-to-output map, the convergence rate of the extremum seeking scheme can be user assigned.

The dither signals in this scheme are somewhat different from the gradient-based ones. The following details the design of the perturbation matrices $\big(L(t) \in \mathbb{R}^{2\times 1},\ \Omega(t) \in \mathbb{R}^{2\times 2},$ and $\varphi(t) \in \mathbb{R}^{2\times 1} \big)$ for a system with two inputs and one output:

$$L(t) = [\frac{2}{c_1}\sin(\omega_1 t), \frac{2}{c_2}\sin(\omega_2 t)]^T, \tag{7.9}$$

$$\Omega(t) = \Omega^T(t), \tag{7.10}$$

$$\Omega_{i,i} = \frac{16}{c_i^2}\Big(\sin^2(\omega_i t) - \frac{1}{2}\Big), \tag{7.11}$$

$$\Omega_{i,k} = \frac{4}{c_i\ c_k}\Big(\sin(\omega_i t)\ \sin(\omega_k t)\Big), \quad i \neq k, \tag{7.12}$$

$$\varphi(t) = [c_1\sin(\omega_1 t),\ c_2\sin(\omega_2 t)]^T, \tag{7.13}$$

where $\omega_i \neq \omega_k$ such that ω_i/ω_k is a rational number, and c_1, c_2 are real positive numbers. The cut-off frequencies for the low and high pass filters , ω_l and ω_h respectively, are designed appropriately according to this recommendation.

$$\omega_l \ll \min\{\omega_i, |\omega_i - \omega_k|, |2\omega_i - \omega_k|\}, \tag{7.14}$$

$$\omega_h > w_i, \qquad\qquad \forall i, k | i \neq k. \tag{7.15}$$

This design derives an estimate of the gradient vector $\hat{G}$ and the Hessian by adding the perturbation signal, $\varphi(t)$, to the estimated optimal input, $\hat{\theta}$. The estimate of the Hessian matrix is inverted by a dynamical system to avoid difficulties of algebraically inverting $\hat{H}$ when it is close to singular, given as

$$\dot{\Gamma} = \omega_r\Gamma - \omega_r\Gamma\hat{H}\Gamma, \tag{7.16}$$

where $\Gamma = \hat{H}^{-1}$.

The reader is referred to [72] for full detailed convergence proof and design method.

To following equations summarize the dynamical system shown in Fig. 7.2:

$$\dot{x} = f\big(x, \beta(x, \theta)\big), \tag{7.17}$$

$$\dot{\eta} = -\omega_h \eta + \omega_h y, \tag{7.18}$$

$$\dot{\hat{G}} = -\omega_l \hat{G} + \omega_l \Lambda, \tag{7.19}$$

$$\dot{\hat{\theta}} = K_n \xi, \tag{7.20}$$

$$\dot{\hat{H}} = -\omega_l \hat{H} + \omega_l \Omega(t)\big(y - \eta\big), \tag{7.21}$$

$$\dot{\Gamma} = \omega_r \Gamma - \omega_r \Gamma \hat{H} \Gamma, \tag{7.22}$$

where

$$\begin{bmatrix} \xi_1 \\ \xi_2 \end{bmatrix} = -\begin{bmatrix} \Gamma_{11} & \Gamma_{12} \\ \Gamma_{21} & \Gamma_{22} \end{bmatrix} \begin{bmatrix} \hat{G}_1 \\ \hat{G}_2 \end{bmatrix}, \tag{7.23}$$

$$\begin{bmatrix} \Lambda_1 \\ \Lambda_2 \end{bmatrix} = \begin{bmatrix} L_1(t) \\ L_2(t) \end{bmatrix} (y - \eta). \tag{7.24}$$

7.5 Extremum Seeking with Adaptive Dither Signal Amplitude

Both of the presented extremum seeking schemes employ dither signals to continuously perturb the plant and obtain derivative like information of the measured output. However, the amplitude of these dither signals is directly proportional to the radius of convergence around the neighborhood of the optimal solution, θ^*, as has been indicted in [64][72]. In addition, the controller rate of convergence is also affected by the magnitude of the perturbation signals. Therefore, it would be convenient and practically useful to design a mechanism that dynamically controls the amplitude of the dither signal .

The following design is built around Newton-based extremum seeking presented

earlier in 7.4 but can easily adapted to other ES configurations. It is well known that the gradient of the objective function vanishes at the extremum point. Since an estimate of the gradient is readily available in different extremum seeking schemes, it can be used to design the control law for the dither signal amplitude. In other words, when $||\xi||$ is large, it is beneficial to have a large value for c_i and vise versa. Although it is tempting to have $c_i = 0$ at the optimal, this is impractical due to measurement noise in y. Instead, the following equation is proposed:

$$\frac{dc_i}{dt} = k_c \, (\alpha - c_i), \tag{7.25}$$

where α is chosen as

$$\alpha = \max(\lambda||\xi||, c_{\min}). \tag{7.26}$$

where k_c and λ are positive scalars that can be designed according to the problem. It is found that passing the norm of the gradient estimate ($||\xi||$) helps to smooth the response.

7.5.1 Simulations Results

The following simulation is presented to demonstrate the difference between the standard Newton-based extremum seeking and the proposed modification. Consider the following static quadratic input-output map:

$$y = g(\theta) = g^* + \frac{1}{2}(\theta - \theta^*)^T H(\theta - \theta^*). \tag{7.27}$$

The following parameters are used to carryout the simulations: $g^* = 100, \theta^* = [2, 4]^T, \hat{\theta}_0 = [2.5, 5]^T, \omega_1 = 3$ rad/s,$\omega_2 = 4$ rad/s,$\omega_l = 0.1$ rad/s, $\omega_h = 0.08$ rad/s, $\omega_r = 0.1$ rad/s, $\hat{H}_0 = 400$ diag($[1, 1]$), $K_n = 0.01$ diag($[1, 1]$), $H_{11} = 100, H_{12} = H_{21} = 30, H_{22} = 20., k_c = 0.1, \lambda = 0.001$, and $c_{\min}$ is chosen to be 0.001.

The estimation of the min $y = g(\theta)$ (output response) and the parameters θ_1, θ_2
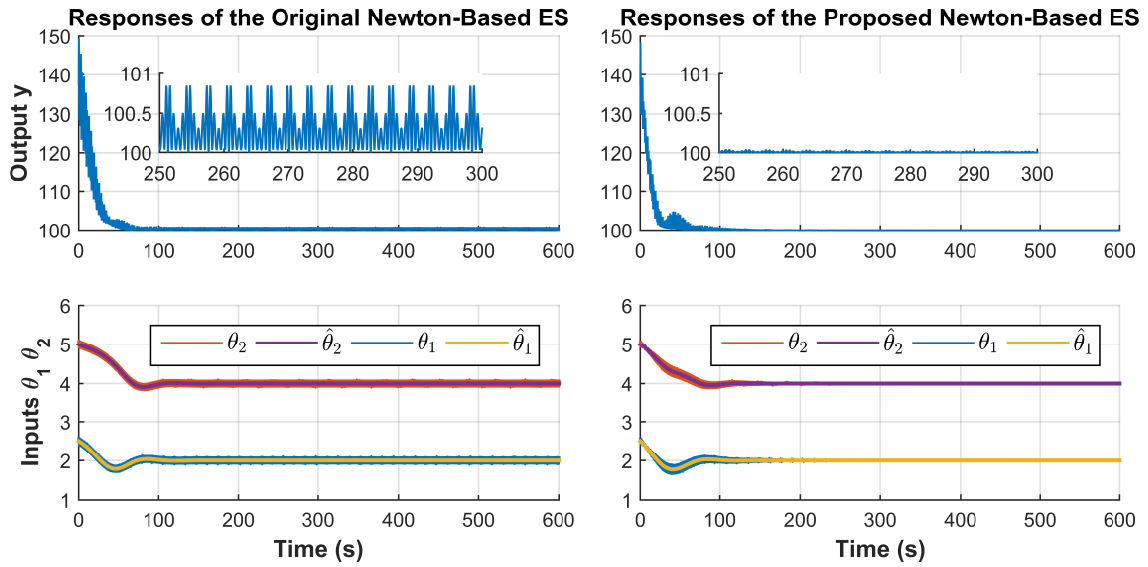
Figure 7.3: Comparing the system output of the proposed multivariable Newton-based ES to that of the original design.

(inputs response) using the original Newton-based ES and the proposed modification are depicted in Fig. 7.3, top plots for the output response, bottom plots for the inputs. It takes about 50 seconds for both methods to converge to $g^* = 100$, but it is clear from the zoom that the output of the proposed controller have less oscillation and goes closer to the optimal point g^* than that of the original one, which keeps on oscillating around it. The response of the inputs $[\theta_1, \theta_2]^T$ shows clearly that the dither signal amplitude converges to the minimum value after approximately 200 seconds, where $||\xi||$ is almost zero and the controller switches to the minimum amplitude.

Chapter 8

Multivariable ES for Solar-Powered DCMD

8.1 Introduction

Now that the distinction between the gradient-based and Newton-based extremum seeking schemes has been established in the previous Chapter 7. This chapter presents the problem formulation and simulation results of solar powered DCMD process optimization using the Newton-based extremum seeking scheme. This controller takes into account the varying feed inlet temperature, due to the unsteady nature of the sun. Moreover, since ES is non-model based, the controller design is robust against plant-model mismatch. This is important since the results obtained in simulation should be applicable to experimental validation.

8.2 Optimal Control Problem of the Solar Powered DCMD

As it is well known, the objective is always to operate any process at optimal settings, which reduces the operational costs and guarantees the performance and stability of the system. This is true for the solar-powered MD water desalination, where the objective is to maximize the water production and reduce the energy consumption at the same time through the manipulation of the feed and permeate inlet mass flow rates.

In terms of DCMD process optimization, the work in [11] developed a neural network model, which was used to calculate optimal feed-forward gains for solar
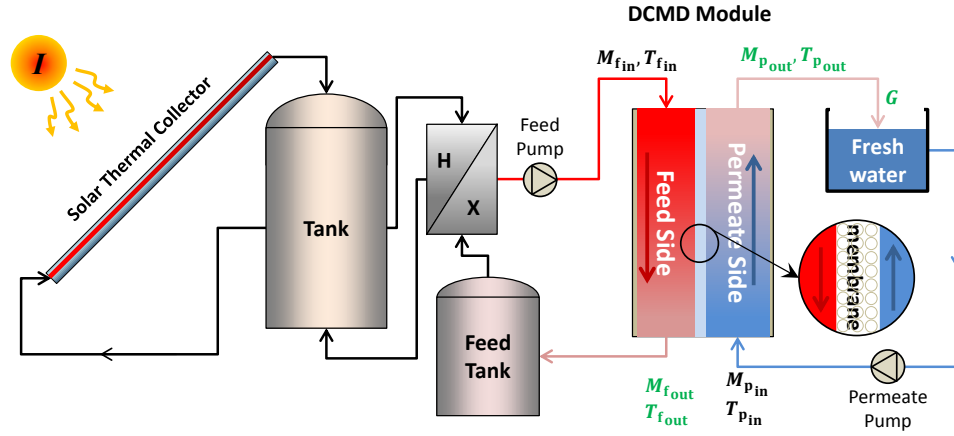
Figure 8.1: Schematic diagram of solar powered DCMD setup.

powered MD. However, when coupling the MD with renewable energy, it is important to consider the unsteady nature of the energy source. Therefore, a real-time optimal control would be more suitable. The MD water desalination process can be further explored and a better overall system performance can be achieved.

Several optimal control schemes have been reported in the literature. For instance, model predictive control (MPC) [73, 74] requires full knowledge of the plant model and the objective function. On the other hand, extremum seeking is another adaptive optimal controller which finds and tracks the peak of the reference-to-output map in real time without knowledge of either the system model or the objective function. Moreover, ES controllers are computationally efficient, especially when compared to the other available methods.

The solar powered DCMD water desalination setup is composed of a solar thermal collector connected to a storage tank and a heat exchanger. The feed water is circulated from the feed tank through a heat exchanger to the DCMD module and back to the feed tank. The permeate is pumped from a fresh water tank into the DCMD module, where it collects the distilled water flux and flow back into the fresh water tank. The setup is depicted in Fig. 8.1, where the control inputs are the mass flow rates of feed and permeate sides. It is clear that the feed inlet temperature $(T_{f_{in}})$ will
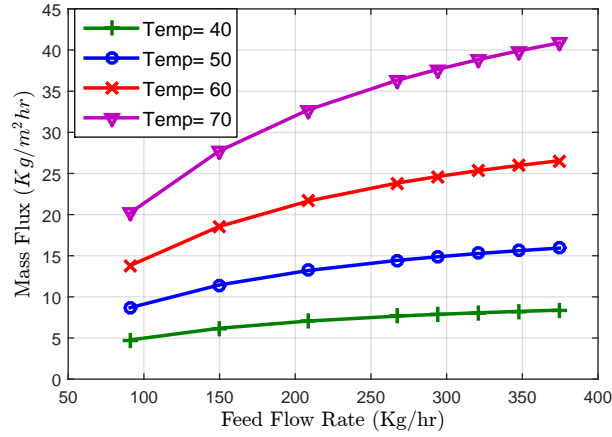
Figure 8.2: The flux response as a function of the feed inlet mass flow rate for various feed inlet temperatures.

vary according to the solar radiation throughout the day, which affects the distilled water flux. An Optimal control strategy is needed to ensure the efficiency of the process under disturbed operating conditions. One way to optimize the process is by maximizing the objective function $\mathcal{Y}$, which penalizes the feed/permeate inlet mass flow rates and rewards the distilled water flux (J).

$$\max \mathcal{Y} = \max \left(\alpha_1 J - (\alpha_2 M_{\text{f}_{\text{in}}} + \alpha_3 M_{\text{p}_{\text{in}}}) \right) \tag{8.1}$$

where, α_1, α_2, and α_3 are used to scale the terms of the objective function to be in the same order of magnitude.

Fig. 8.2 depicts the flux response of the DCMD process under various feed inlet temperatures and feed inlet mass flow rates. In this simulation, the permeate inlet mass flow rate was kept constant at 256 Kg/hr, while the feed inlet mass flow rate was increased from 90 Kg/hr to 375 Kg/hr. This was repeated for 5 feed inlet temperatures. As demonstrated in the figure, increasing the feed inlet temperature increased the distilled water flux. While increasing the feed inlet mass flow rate increases the
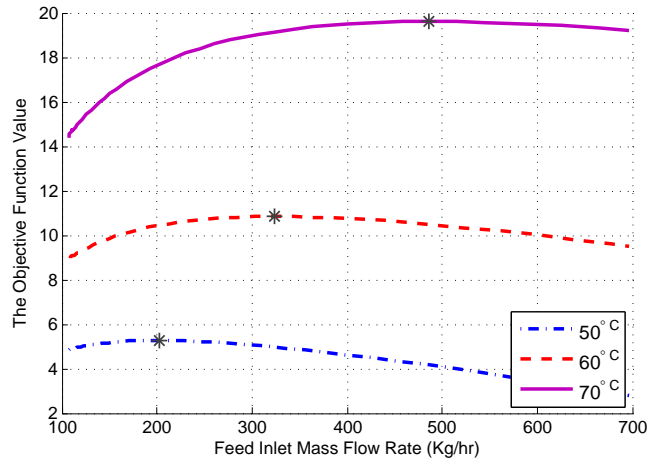
Figure 8.3: The objective function ($\mathcal{Y}$) at three feed inlet temperatures.

flux, the flux reaches saturation values at high feed inlet mass flow rates. This behavior provokes the following question: What is the optimal feed/permeate flow rate for a given feed inlet temperature? Simulation results of equation (8.1) shows that there exists a maximum value of the objective function ($\mathcal{Y}$) which varies for different feed inlet temperatures, as shown in Fig. 8.3. The objective function behaves similarly with respect to the permeate inlet mass flow rate. Therefore, the controller is required to automatically track the peak of the objective function by manipulating the feed and permeate inlet mass flow rates.

The block diagram of Newton-based ES for DCMD is depicted in Fig. 8.4. Notice that the feed inlet temperature ($T_{f_{in}}$) is considered as a disturbance in this setup. The DAE model presented in chapter 3 is used to simulate the flux response, which is then fed to the objective function along with values of the control inputs ($\theta = [M_{f_{in}}, M_{p_{in}}]$). As demonstrated in Fig. 8.3, the performance function ($\mathcal{Y}$) has a $T_{f_{in}}$ dependent peak. Hence, Assumptions 7.1 and 7.2 are valid and the closed-loop system is given by

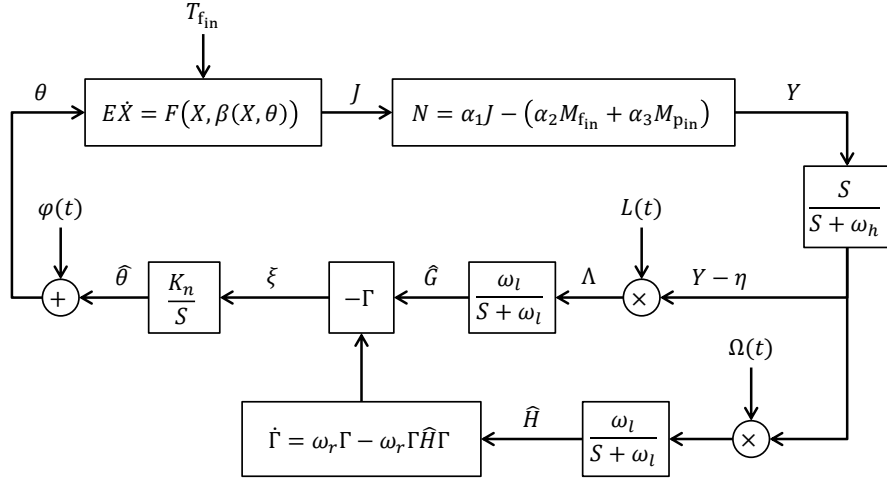$$E\dot{X} = F\big(X, \beta(X, \theta)\big). \tag{8.2}$$

Figure 8.4: The block diagram of the Newton-based ES for DCMD.

The perturbation matrices $\left(L(t) \in \mathbb{R}^{2\times 1},\ \Omega(t) \in \mathbb{R}^{2\times 2}, \text{and } \varphi(t) \in \mathbb{R}^{2\times 1}\right)$, and the design of the high and low pass filters follow the guidelines presented in section § 7.4.

8.3 Simulation Results

Simulations were carried out in order to demonstrate the effectiveness of the proposed controller to optimize the solar powered DCMD water desalination process. For this, realistic membrane parameters were used, as listed in Table 8.1. In order to design and tune the parameters of the Newton-based ES controller, we started by choosing the perturbation frequencies, to separate the time scale of the DCMD system from gradient and Hessian estimation filters and ensures a resealable convergence time. It was found that setting $\omega_1 = 3\text{rad/s}, \omega_2 = 2\text{rad/s}$ gave a good result. The next step was to tune the amplitude of the perturbation signal, setting $c_1 = c_2 = 0.15$. The frequencies of low and high-pass filters are chosen to have slow time scale, $\omega_l = 0.1\text{rad/s}, \omega_h = 4\text{rad/s},$. The frequency of dynamical inversion system Γ was designed to be very slow, which ensures a smoother estimate of the Hessian inverse, $\omega_r = 0.0008$. Finally, the gain (K_n) was designed to balance between convergence time and stability of the closed loop system, $K_n = \text{diag}([0.05, 0.05])$.

Table 8.1: DCMD Module Parameters

Property	Value
Pore size	0.27 μm
Total thickness	0.170 mm
Porosity	77%
Module length	0.4 m
Module width	0.15 m
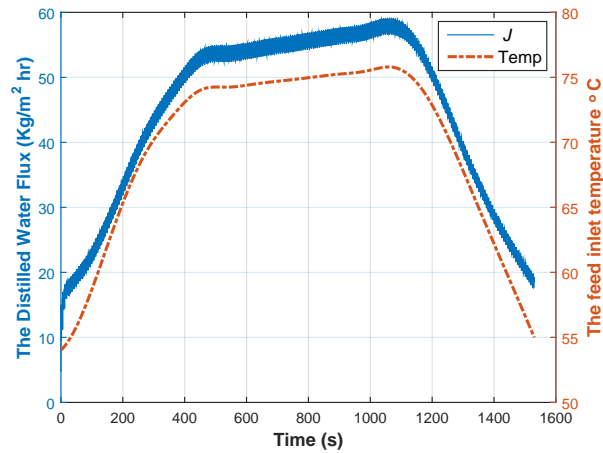
Figure 8.5: The distilled water flux (J) is shown on the left axes. The dashed line shows the feed inlet temperature profile.

The feed inlet temperature profile is designed to reflect a realistic behavior which is depicted in Fig. 8.5, by the dashed line. The permeate inlet temperature is kept constant through out the simulation at 20 °C. As the feed inlet temperature increase, the distilled water flux is optimized taking into account the feed and permeate inlet mass flow rates, as shown in Fig. 8.5 (solid line).

Figure 8.6: The estimated optimal inlet mass flow rates for the feed and permeate sides along with objective function value. The Newton-based ES quickly initializes and then tracks the peak with smooth transitions

Chapter 9

Concluding Remarks

This chapter briefly provides an overview of the proposed reduced order dynamic model of Direct Contact Membrane Distillation process for water desalination and its relevance to the process optimization. A summary of all the work done in this thesis along with some future work directions are provided in the next two sections.
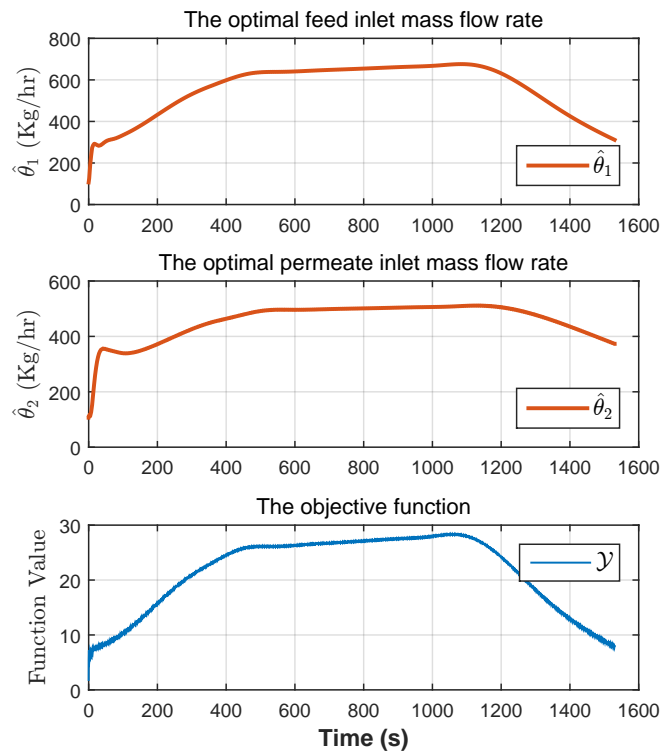
9.1   Summary

Membrane distillation (MD) is an emerging technology that has great potential for sustainable water desalination. In order to pave the way for the successful commercialization of MD-based water desalination, adequate and accurate dynamical models of the process are essential. A novel dynamic model of DCMD was proposed based on the analogy between electrical and thermal systems. This model adopts the lumped capacitance method to obtain a reduced order version of somewhat the equivalent partial differential equation model of the DCDMD process. The model directly solves for the temperature distribution along the flow direction and the local flux values. Simulation results agreed with experimentally collected data for both steady-state and dynamic response of the system. The effect of some operational parameters was demonstrated through process efficiency. The problem of membrane fouling detection was addressed by extending the proposed model to account for the thermal resistance induced by the fouling layer. Then, an adaptive observer was developed for nonlinear descriptor systems, and specific implementation for the case of fouling detection in

DCMD was demonstrated. For the purpose of process optimization, two schemes of Extremum Seeking were then introduced. Finally, the optimal control problem of solar powered DCMD model was formulated and the model was used to carry out simulation and demonstrate the method.

9.2 Future Research Work

The work presented in this thesis can be extended in the following directions.

⋆ We would like to further investigate and test the proposed method for membrane fouling detection and membrane parameters identification on real DCMD experimental setups.

⋆ The promising simulation results of the solar powered DCMD process optimization can be a starting point for experimental validation of ES based controller.

⋆ As it has been presented in section 8.2, the solar powered DCMD configuration is composed of a solar collector and a thermal storage loop and the DCMD module. Although component by component optimization improves the efficiency of the process, considering the whole system into the optimization problem formulation exploits all the degrees of freedom and may yield a better overall result.

⋆ Both of the presented extremum seeking schemes rely on dither signals to modulate the measured performance signal and obtain an estimate of its derivatives. A practically useful modification to the extremum seeking schemes is to dynamically adapt the amplitude of these dither signals. This is beneficial in order to obtain a tighter convergence to the desired optimal solution, as it is proportional to $O(a)$.

REFERENCES

[1] M. Khayet and T. Matsuura, "Chapter 1 - introduction to membrane distillation," in *Membrane Distillation*, M. K. Matsuura, Ed. Amsterdam: Elsevier, 2011, pp. 1 – 16.

[2] H. J. Hwang, K. He, S. Gray, J. Zhang, and I. S. Moon, "Direct contact membrane distillation (DCMD): Experimental study on the commercial PTFE membrane and modeling," *Journal of Membrane Science*, vol. 371, no. 1-2, pp. 90–98, Apr. 2011.

[3] A. Cipollina, G. Micale, and L. Rizzuti, *Seawater desalination: conventional and renewable energy processes.* Springer Science & Business Media, 2009.

[4] K. C. Ng, K. Thu, Y. Kim, A. Chakraborty, and G. Amy, "Adsorption desalination: An emerging low-cost thermal desalination method," *Desalination*, vol. 308, no. 0, pp. 161 – 179, 2013, new Directions in Desalination.

[5] A. Alkhudhiri, N. Darwish, and N. Hilal, "Membrane distillation: A comprehensive review," *Desalination*, vol. 287, no. 0, pp. 2 – 18, 2012.

[6] M. Khayet and T. Matsuura, "Chapter 10 - direct contact membrane distillation," in *Membrane Distillation*, M. Khayet and T. Matsuura, Eds. Amsterdam: Elsevier, 2011, pp. 249 – 293.

[7] J. Koschikowski, M. Wieghaus, and M. Rommel, "Membrane Distillation for Solar Desalination," in *Seawater Desalination*, A. Cipollina, G. Micale, and L. Rizzuti, Eds. Springer Berlin Heidelberg, Jul. 2009, ch. 7, pp. 165–187.

[8] C. H. Lee and W. H. Hong, "Effect of operating variables on the flux and selectivity in sweep gas membrane distillation for dilute aqueous isopropanol," *Journal of Membrane Science*, vol. 188, no. 1, pp. 79 – 86, 2001.

[9] M. Khayet and T. Matsuura, "Chapter 12 - vacuum membrane distillation," in *Membrane Distillation*, M. Khayet and T. Matsuura, Eds. Amsterdam: Elsevier, 2011, pp. 323 – 359.

[10] L. Qianliang, M. Jun, W. Zhenghui, C. Liwei, and W. Panpan, "The effect of ammonia initial concentration in membrane distillation process for high ammonia concentration wastewater treatment," *2011 International Conference on Consumer Electronics, Communications and Networks (CECNet)*, pp. 1795–1797, Apr. 2011.

[11] R. Porrazzo, A. Cipollina, M. Galluzzo, and G. Micale, "A neural network-based optimizing control system for a seawater-desalination solar-powered membrane distillation unit," *Computers and Chemical Engineering*, vol. 54, no. 0, pp. 79 – 96, 2013.

[12] P. Zolotarev, V. Ugrozov, I. Volkina, and V. Nikulin, "Treatment of waste water for removing heavy metals by membrane distillation," *Journal of Hazardous Materials*, vol. 37, no. 1, pp. 77 – 82, 1994.

[13] H. Chang, G.-B. Wang, Y.-H. Chen, C.-C. Li, and C.-L. Chang, "Modeling and optimization of a solar driven membrane distillation desalination system," *Renewable Energy*, vol. 35, no. 12, pp. 2714 – 2722, 2010.

[14] Y.-D. Kim, K. Thu, N. Ghaffour, and K. C. Ng, "Performance investigation of a solar-assisted direct contact membrane distillation system," *Journal of Membrane Science*, vol. 427, no. 0, pp. 345 – 364, 2013.

[15] A. Chafidz, S. Al-Zahrani, M. N. Al-Otaibi, C. F. Hoong, T. F. Lai, and M. Prabu, "Portable and integrated solar-driven desalination system using membrane distillation for arid remote areas in saudi arabia," *Desalination*, vol. 345, no. 0, pp. 36 – 49, 2014.

[16] R. Schofield, A. Fane, and C. Fell, "Heat and mass transfer in membrane distillation," *Journal of Membrane Science*, vol. 33, no. 3, pp. 299 – 313, 1987.

[17] M. Qtaishat, T. Matsuura, B. Kruczek, and M. Khayet, "Heat and mass transfer analysis in direct contact membrane distillation," *Desalination*, vol. 219, no. 1-3, pp. 272–292, Jan. 2008.

[18] K. W. Lawson and D. R. Lloyd, "Membrane distillation," *Journal of Membrane Science*, vol. 124, no. 1, pp. 1 – 25, 1997.

[19] V. Bui, L. Vu, and M. Nguyen, "Modelling the simultaneous heat and mass transfer of direct contact membrane distillation in hollow fibre modules," *Journal of Membrane Science*, vol. 353, no. 1-2, pp. 85–93, May 2010.

[20] E. K. Summers, H. a. Arafat, and J. H. Lienhard, "Energy efficiency comparison of single-stage membrane distillation (MD) desalination cycles in different configurations," *Desalination*, vol. 290, pp. 54–66, Mar. 2012.

[21] Y. M. Manawi, M. Khraisheh, A. K. Fard, F. Benyahia, and S. Adham, "Effect of operational parameters on distillate flux in direct contact membrane distillation (dcmd): Comparison between experimental and model predicted performance," *Desalination*, vol. 336, no. 0, pp. 110 – 120, 2014.

[22] F. Eleiwi and T. M. Laleg-kirati, "Dynamic modeling and optimization in membrane distillation system," in *The 19th World Congress of the International Federation of Automatic Control*, Cape Town, South Africa, 2014, pp. 3327–3332.

[23] A. Karam and T. Laleg-Kirati, "Electrical thermal networks for direct contact membrane distillation modeling," in *Control Applications (CCA), 2014 IEEE Conference on*, Oct 2014, pp. 1563–1569.

[24] R. Ford, "Electrical analogues for heat exchangers," *Proceedings of the IEE - Part B: Radio and Electronic Engineering*, vol. 103, no. 7, pp. 65–82, 1956.

[25] A. Ferreira, S. Chen, M. Simaan, J. Boston, and J. Antaki, "A nonlinear state-space model of a combined cardiovascular system and a rotary pump," in *Decision and Control, 2005 and 2005 European Control Conference. CDC-ECC '05. 44th IEEE Conference on*, Dec 2005, pp. 897–902.

[26] A. Robertson and D. Gross, "An electrical-analog method for transient heat-flow analysis," *Journal of Research of the National Bureau of Standards*, vol. 61, no. 2, p. 105, Aug. 1958.

[27] I. Fatt, "A new electric analogue model for nonsteady state flow problems," *AIChE Journal*, vol. 4, no. 1, pp. 49–52, 1958.

[28] MATLAB, *version 8.0 (R2012b)*. Natick, Massachusetts: The MathWorks Inc., 2012.

[29] L. Francis, N. Ghaffour, A. Alsaadi, S. Nunes, and G. Amy, "Performance evaluation of the dcmd desalination process under bench scale and large scale module operating conditions," *Journal of Membrane Science*, vol. 455, no. 0, pp. 103 – 112, 2014.

[30] L. Francis, N. Ghaffour, A. A. Alsaadi, and G. L. Amy, "Material gap membrane distillation: A new design for water vapor flux enhancement," *Journal of Membrane Science*, vol. 448, no. 0, pp. 240 – 247, 2013.

[31] A. S. Alsaadi, L. Francis, G. L. Amy, and N. Ghaffour, "Experimental and theoretical analyses of temperature polarization effect in vacuum membrane distillation," *Journal of Membrane Science*, vol. 471, no. 0, pp. 138 – 148, 2014.

[32] Q. Zhang, "A new residual generation and evaluation method for detection and isolation of faults in non-linear systems," *Int. J. Adapt. Control Signal Process.*, vol. 14, no. 7, p. 759773, 2000.

[33] J. Zhang, A. K. Swain, S. K. Nguang, and A. Nasiri, "Estimation of actuator and sensor faults for nonlinear systems using a descriptor system approach," in *Decision and Control (CDC), 2014 IEEE 53rd Annual Conference on*, Dec 2014, pp. 1834–1839.

[34] A. M. Nagy-Kiss, D. Ichalal, G. Schutz, and J. Ragot, "Fault tolerant control for uncertain descriptor multi-models with application to wastewater treatment plant," in *American Control Conference (ACC), 2015*, July 2015, pp. 5718–5725.

[35] D. Luenberger, "An introduction to observers," *Automatic Control, IEEE Transactions on*, vol. 16, no. 6, pp. 596–602, Dec 1971.

[36] G. Luders and K. Narendra, "An adaptive observer and identifier for a linear system," *Automatic Control, IEEE Transactions on*, vol. 18, no. 5, pp. 496–499, Oct 1973.

[37] G. Kreisselmeier, "Adaptive observers with exponential rate of convergence," *Automatic Control, IEEE Transactions on*, vol. 22, no. 1, pp. 2–8, Feb 1977.

[38] Q. Zhang, "Adaptive observer for multiple-input-multiple-output (MIMO) linear time-varying systems," *Automatic Control, IEEE Transactions on*, vol. 47, no. 3, pp. 525–529, Mar 2002.

[39] G. Besanon, "Remarks on nonlinear adaptive observer design," *Systems & Control Letters*, vol. 41, no. 4, pp. 271 – 280, 2000.

[40] I. Y. Tyukin, E. Steur, H. Nijmeijer, and C. van Leeuwen, "Adaptive observers and parameter estimation for a class of systems nonlinear in the parameters," *Automatica*, vol. 49, no. 8, pp. 2409 – 2423, 2013.

[41] P. Liu, Q. Zhang, X. Yang, and L. Yang, "Passivity and optimal control of descriptor biological complex systems," *Automatic Control, IEEE Transactions on*, vol. 53, no. Special Issue, pp. 122–125, Jan 2008.

[42] F. Lewis, "A survey of linear singular systems," *Circuits, Systems and Signal Processing*, vol. 5, no. 1, pp. 3–36, 1986.

[43] M. Darouach and M. Boutayeb, "Design of observers for descriptor systems," *Automatic Control, IEEE Transactions on*, vol. 40, no. 7, pp. 1323–1327, Jul 1995.

[44] M. Hou and P. Muller, "Observer design for descriptor systems," *Automatic Control, IEEE Transactions on*, vol. 44, no. 1, pp. 164–169, Jan 1999.

[45] D. Koenig and S. Mammar, "Design of proportional-integral observer for un-known input descriptor systems," *Automatic Control, IEEE Transactions on*, vol. 47, no. 12, pp. 2057–2062, Dec 2002.

[46] D. Koenig, "Unknown input proportional multiple-integral observer design for linear descriptor systems: application to state and fault estimation," *Automatic Control, IEEE Transactions on*, vol. 50, no. 2, pp. 212–217, Feb 2005.

[47] H. Hamdi, M. Rodrigues, C. Mechmeche, D. Theilliol, and N. B. Braiek, "Fault detection and isolation in linear parameter-varying descriptor systems via pro-portional integral observer," *Int. J. Adapt. Control Signal Process.*, vol. 26, no. 3, p. 224240, March 2012.

[48] S. Kaprielian and J. Turi, "An observer for a nonlinear descriptor system," in *Decision and Control, 1992., Proceedings of the 31st IEEE Conference on*, 1992, pp. 975–976 vol.1.

[49] G. Lu and D. Ho, "Full-order and reduced-order observers for lipschitz descriptor systems: the unified lmi approach," *Circuits and Systems II: Express Briefs, IEEE Transactions on*, vol. 53, no. 7, pp. 563–567, July 2006.

[50] L.-N. Zhou, C.-Y. Yang, and Q.-L. Zhang, "Observers for descriptor systems with slope-restricted nonlinearities," *International Journal of Automation and Computing*, vol. 7, no. 4, pp. 472–478, 2010.

[51] C. Yang, Q. Zhang, and T. Chai, "Nonlinear observers for a class of nonlinear descriptor systems," *Optim. Control Appl. Meth.*, vol. 34, no. 3, p. 348363, 2013.

[52] Y. Uetake, "Adaptive observer for continuous descriptor systems," *Automatic Control, IEEE Transactions on*, vol. 39, no. 10, pp. 2095–2100, Oct 1994.

[53] M. Alma and M. Darouach, "Adaptive observers design for a class of linear descriptor systems," *Automatica*, vol. 50, no. 2, pp. 578 – 583, 2014.

[54] L. Dai, *Singular Control Systems*, 1st ed. Springer-Verlag Berlin Heidelberg, 1989.

[55] I. Masubuchi, Y. Kamitane, A. Ohara, and N. Suda, "H control for descriptor systems: A matrix inequalities approach," *Automatica*, vol. 33, no. 4, pp. 669 – 673, 1997.

[56] H. K. Khalil, *Nonlinear Systems*, 3rd ed.   Prentice Hall, 2002.

[57] J. Lofberg, "Yalmip : a toolbox for modeling and optimization in matlab," in *Computer Aided Control Systems Design, 2004 IEEE International Symposium on*, Sept 2004, pp. 284–289.

[58] M. Gryta, "Fouling in direct contact membrane distillation process," *Journal of Membrane Science*, vol. 325, no. 1, pp. 383 – 394, 2008.

[59] G.-Y. Chai, A. Greenberg, and W. Krantz, "Ultrasound, gravimetric, and sem studies of inorganic fouling in spiral-wound membrane modules," *Desalination*, vol. 208, no. 1, pp. 277 – 293, 2007.

[60] L. Sim, Z. Wang, J. Gu, H. Coster, and A. Fane, "Detection of reverse osmosis membrane fouling with silica, bovine serum albumin and their mixture using in-situ electrical impedance spectroscopy," *Journal of Membrane Science*, vol. 443, pp. 45 – 53, 2013.

[61] H. Monclus, G. Ferrero, G. Buttiglieri, J. Comas, and I. Rodriguez-Roda, "Online monitoring of membrane fouling in submerged {MBRs}," *Desalination*, vol. 277, no. 13, pp. 414 – 419, 2011.

[62] F. Delmotte, M. Dambrine, S. Delrot, and S. Lalot, "Fouling detection in a heat exchanger: A polynomial fuzzy observer approach," *Control Engineering Practice*, vol. 21, no. 10, pp. 1386 – 1395, 2013.

[63] A. M. Karam and T. M. Laleg-kirati, "Nonlinear adaptive descriptor observer for the joint states and parameters estimation," *Submitted*, 2016.

[64] M. Krstic and H.-H. Wang, "Stability of extremum seeking feedback for general nonlinear dynamic systems," *Automatica*, vol. 36, no. 4, pp. 595 – 601, 2000.

[65] H.-H. Wang, S. Yeung, and M. Krstic, "Experimental application of extremum seeking on an axial-flow compressor," *Control Systems Technology, IEEE Transactions on*, vol. 8, no. 2, pp. 300–309, Mar 2000.

[66] A. Ghaffari, M. Krstic, and S. Seshagiri, "Power optimization for photovoltaic microconverters using multivariable newton-based extremum seeking," *Control Systems Technology, IEEE Transactions on*, vol. 22, no. 6, pp. 2141–2149, Nov 2014.

[67] M. Guay, D. Dochain, and M. Perrier, "Adaptive extremum seeking control of continuous stirred tank bioreactors with unknown growth kinetics," *Automatica*, vol. 40, no. 5, pp. 881 – 888, 2004.

[68] A. Ghaffari, M. Krstic, and S. Seshagiri, "Power optimization and control in wind energy conversion systems using extremum seeking," *Control Systems Technology, IEEE Transactions on*, vol. 22, no. 5, pp. 1684–1695, Sept 2014.

[69] K. B. Ariyur and M. Krstić, *Real-time optimization by extremum-seeking control.* Wiley-Blackwell, 2003.

[70] W. Moase, C. Manzie, and M. Brear, "Newton-like extremum-seeking for the control of thermoacoustic instability," *Automatic Control, IEEE Transactions on*, vol. 55, no. 9, pp. 2094–2105, Sept 2010.

[71] D. Nesic, Y. Tan, W. Moase, and C. Manzie, "A unifying approach to extremum seeking: Adaptive schemes based on estimation of derivatives," in *Decision and Control (CDC), 2010 49th IEEE Conference on*, Dec 2010, pp. 4625–4630.

[72] A. Ghaffari, M. Krsti, and D. Nei, "Multivariable newton-based extremum seeking," *Automatica*, vol. 48, no. 8, pp. 1759 – 1767, 2012.

[73] C. E. Garca, D. M. Prett, and M. Morari, "Model predictive control: Theory and practicea survey," *Automatica*, vol. 25, no. 3, pp. 335 – 348, 1989.

[74] D. Mayne, J. Rawlings, C. Rao, and P. Scokaert, "Constrained model predictive control: Stability and optimality," *Automatica*, vol. 36, no. 6, pp. 789 – 814, 2000.

[75] F. Chen and W. Zhang, "LMI criteria for robust chaos synchronization of a class of chaotic systems," *Nonlinear Analysis: Theory, Methods & Applications*, vol. 67, no. 12, pp. 3384 – 3393, 2007.

APPENDICES

Appendix A

Electrical Analogues for Thermal Elements

The analogy can be derived from the basic equations of electrical and thermal systems. Let's start by considering the one-dimensional heat conduction through an element of cross-sectional area A_{cs} and thermal conductivity k and length of δx, see Fig. A.1. The heat transfer rate is given by the Fourier's law as:

$$Q = -kA_{cs}\frac{\partial T}{\partial x}. \tag{A.1}$$

The difference of heat transfer rates between two parallel surfaces is equal to the heat absorbed to raise the temperature of the control volume, as given by:

$$\frac{\partial Q}{\partial x} = -\rho A_{cs}c_p\frac{\partial T}{\partial t}. \tag{A.2}$$

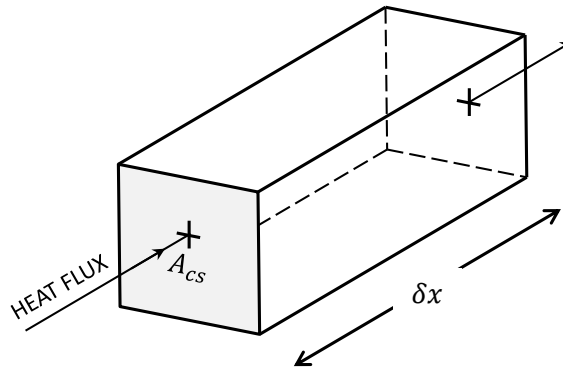Substituting (A.1) into (A.2) gives the one dimensional heat diffusion equation

Figure A.1: 1D heat flow through an element of length δx and cross sectional area of A_{cs}.

Table A.1: Electrical analogues of thermal system

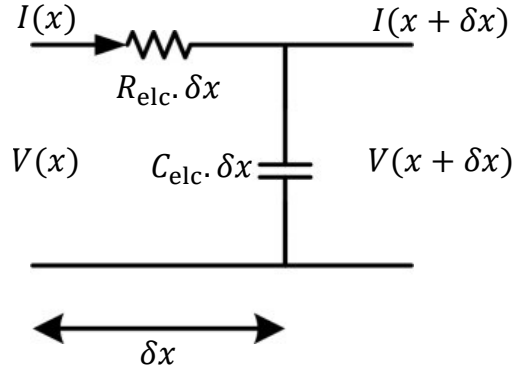| Electrical			Thermal		
Element	Expression	Unit	Element	Expression	Unit
Voltage	V	V	Temperature	T	°C or K
Current	I	A	Heat transfer rate	Q	Watt (W=J/s)
Resistor	$R_{\text{elc}}\delta x$	Ω	Resistor	$\dfrac{\delta x}{kA_{cs}}$	°C/W
Capacitor	$C_{\text{elc}}\delta x$	F	Capacitor	$C = c_p m$	J/°C

Figure A.2: Schematic diagram of a transmission line.

as:

$$\frac{\partial T}{\partial t} = \frac{k}{\rho c_p}\frac{\partial^2 T}{\partial x^2}. \tag{A.3}$$

This is a 1D heat equation, in which heat transfer takes place along the length δx and with the assumptions that heat only enters or leaves the element from end surfaces, further there is no heat exchange on the side boundaries.

In order to complete the analogy, a section of a uniform transmission line is considered as depicted in Fig. A.2, where the line resistance and capacitance (R_{elc}, C_{elc} respectively) are given per unit length. For some length δx, the total resistance and capacitance are $R_{elc}\delta x$ and $C_{elc}\delta x$ respectively.

Ohm's law gives:

$$V(x + \delta x) - V(x) = -IR_{\text{elc}}.\delta x. \tag{A.4}$$

Applying Kirchoff's current law gives:

$$I(x + \delta x) - I(x) = -C_{elc}.\delta x \frac{\partial V}{\partial t}. \tag{A.5}$$

Taking the limit as $\delta x \to 0$ for (A.4) and (A.5) respectively gives:

$$I = -\frac{1}{R_{elc}} \frac{\partial V}{\partial x}, \tag{A.6}$$

$$\frac{\partial I}{\partial x} = -C_{elc} \frac{\partial V}{\partial t}. \tag{A.7}$$

Combining equations (A.6) and (A.7) results in the telegraph equations:

$$\frac{\partial^2 V}{\partial x^2} = R_{elc} C_{elc} \frac{\partial V}{\partial t}. \tag{A.8}$$

Comparing (A.6) with (A.1) and (A.7) with (A.2), leads to the analogy between electrical and thermal systems given in Table A.1.

Appendix B

Preliminaries

Here, we present some preliminary results, which are used in the proof of convergence in section 5.

Lemma B.1: [75] Let x and y be real vectors of the same dimension. Then, for any scalar $\epsilon > 0$ the following inequality holds

$$2x^T y \leqslant \epsilon x^T x + \epsilon^{-1} y^T y. \tag{B.1}$$

Lemma B.2: (Schur complement) Given any real matrices X_1, X_2 and X_3 such that $X_1 = X_1^T$ and $X_3 > 0$, then

$$X_1 + X_2^T X_3^{-1} X_2 < 0, \tag{B.2}$$

if and only if

$$\begin{bmatrix} X_1 & X_2^T \\ X_2 & -X_3 \end{bmatrix} < 0. \tag{B.3}$$

Lemma B.3: [56](Barbalat's lemma) Let $\phi : \mathbb{R} \to \mathbb{R}$ be a uniformly continuous function on $[0, \infty)$. Suppose that $\lim_{t \to \infty} \int_0^t \phi(\tau)d\tau$ exists and is finite. Then,

$$\phi(t) \to 0 \quad \text{as} \quad t \to \infty.$$

Appendix C

Publications

Journal Papers

[J1] Ayman Karam and T. M. Laleg-Kirati, "Electrical Thermal Network for Direct Contact Membrane Distillation Modeling and Analysis", *Journal of Process Control*, vol. 47, November 2016, Pages 87-97.

[J2] Ayman Karam, A. Alsaadi, N. Ghaffour, and T. M. Laleg-Kirati, "Analysis of direct contact membrane distillation based on a lumped-parameter dynamic predictive model", *Desalination*, vol. 402, 16 January 2017, Pages 50-61.

Under Preparation

[U1] Ayman Karam and T. M. Laleg-Kirati, "Membrane Fouling Detection in Direct Contact Membrane Distillation based on Nonlinear Adaptive Descriptor Observer".

[U2] P. Bendevis, Ayman Karam, and T. M. Laleg-Kirati, "Control of Solar Thermal Distillation Systems".

[U3] J. Lee, A. Alsaadi, Ayman Karam, L. Francis, N. Ghaffour, "Theoretical Investigation of the Water Production Inversion in Multi-Stage Direct Contact Membrane Distillation (DCMD)".

[U4] Ayman Karam and T. M. Laleg-Kirati, "Nonlinear Adaptive Descriptor Observer for Joint States and Parameters Estimation".

Conference Proceedings

[C1] Ayman Karam and T. M. Laleg-Kirati, "Real Time Optimization of Solar Powered Direct Contact Membrane Distillation Based on Multivariable Extremum Seeking", *in Control Applications (CCA), 2015 IEEE Conference on , pp.1618-1623, 21-23 Sept. 2015.*

[C2] Ayman Karam and T. M. Laleg-Kirati, "Electrical thermal networks for direct contact membrane distillation modeling", *Control Applications, 2014 IEEE Conference on*, pp.1563-1569, Oct. 2014.

[C3] Ayman Karam and T. M. Laleg-Kirati, "Dynamical Model for Direct Contact Membrane Distillation based on Electrical Analogues", *Paper presented at the 10th International Congress on Membranes and Membrane Progresses (ICOM2014)*, China, 2014.

Poster Presentations

- Ayman Karam and T. M. Laleg-Kirati, "Towards Smart Desalination Systems", *poster presented at the KAUST-NSF Research Conference on Electronic Materials, Devices, and Systems for a Sustainable Future*, KAUST, Saudi Arabia, Mar. 2016.

- Ayman Karam and T. M. Laleg-Kirati, "Sustainable Desalination for Smart Cities", *poster presented at the Human-Machine Networks and Intelligent Infrastructure Conference*, KAUST, Saudi Arabia, Oct. 2015.

Appendix D

Patents

[P1] Taous Meriem Laleg-Kirati; Ayman Karam; Fadi Eleiwi - Temprature and membrane characteristics soft sensing of membrane distillation process, "patent pending" - US application PCT/IB2016/055467.

[P2] Taous Meriem Laleg-Kirati; Ayman Karam; Fadi Eleiwi - Inlet temperatures controller for Membrane distillation system, "patent pending" -US application PCT/IB2016/053946.

[P3] Taous Meriem Laleg-Kirati; Ayman Karam; Fadi Eleiwi - Real time optimal controller for solar powered Direct Contact Membrane Distillation (DCMD), "patent pending" -US provisinal application.

[P4] Taous Meriem Laleg-Kirati; Ayman Karam - Smart membranes for monitoring membrane-based desalination processe, "patent pending" -US provisional application, 62/318,008.